3D Photoacoustic Molecular Imaging

by

Ryan K. W. Chee

A thesis submitted in partial fulfillment of the requirements for the degree of

Doctor of Philosophy

in

Biomedical Engineering

Department of Electrical and Computer Engineering
University of Alberta

Abstract

Molecular imaging is allowing researchers to make ground breaking strides in science and medicine by imaging molecular processes in vivo. Applications include detecting disease biomarkers, improving drug efficacy, studying biochemistry, and understanding disease mechanisms of action. Photoacoustic (PA) imaging is a promising non-invasive imaging technique that uses pulse laser excitation to induce PA signals. PA imaging has promising potential as a molecular imaging technique, but it has yet to be fully realized. In comparison to other comparable molecular imaging methods like fluorescence imaging, PA imaging has significantly higher resolutions and faster imaging rates at a 1-5 cm imaging depth. This makes PA imaging potentially ideal for small animal studies which are the backbone of biomedical discovery and innovation. With further advances into 3D PA imaging technology and molecular PA contrast agents, PA molecular imaging could become an essential molecular imaging technique in various fields of scientific research.

This thesis aims to further 3D PA molecular imaging via a multi-dimensional approach by integrating work on transducers, molecular contrast agents, and PA applications. We start with the development of a promising capacitive micromachined ultrasonic transducer (CMUT) known as a top-orthogonal-to-bottom-electrode (TOBE) CMUT, which was developed to improve the feasibility of acquiring and transferring signals from large 3D imaging arrays. We characterize and demonstrate the potential of such arrays for 3D PA imaging. We also demonstrate that these TOBE CMUTs can potentially acquire 3D PA images orders of magnitude faster than traditional large 3D imaging arrays using a novel design specific technique known as modulation encoding. We then developed interlaced multifrequency CMUTs to increase imaging sensitivity to molecular PA contrast agents. Interlaced multifrequency CMUTs have a broader bandwidth, allowing improved detection of diffuse contrast agents in comparison to high-frequency clinical transducers all while maintaining the ability to image fine structures. This was followed by our work on background signal suppression using novel photoswitchable PA molecular contrast agents, sGPC2 and sGPC3. These photoswitchable PA contrast agents can be tagged to molecules of interest for molecular imaging and can reduce background signals by switching between two absorption states. Furthermore, we introduce a technique to simultaneously image and distinguish multiple photoswitchable contrast agents for multiplexed molecular imaging. Multiplexed molecular imaging is essential for imaging real molecular processes that have multiple targets of interest. Finally, we apply photoacoustic imaging to the quantification of tumour volumes to help study the role of p110β in tumour angiogenesis. We compare the accuracy of the PA measurements by comparing it with measured values obtained via staining histology.

Preface

This thesis is an original work by Ryan K. W. Chee. *In vivo* experiment procedures involving animals described in this thesis follow the laboratory animal protocol approved by the University of Alberta Animal Use and Care Committee. Chapters 3 through 6 contain work that has either been published in or submitted to a peer-reviewed journal. These chapters contain minor modifications from the original papers to adhere to the thesis format. The original publication and co-author contributions for each of the thesis chapters is detailed as follows.

Chapter 3 of this thesis has been published as R. K. W. Chee, A. Sampaleanu, D. Rishi, and R. J. Zemp, "Top orthogonal to bottom electrode (TOBE) 2D CMUT arrays for 3D photoacoustic imaging," *IEEE transactions on ultrasonics, ferroelectrics, and frequency control*, 61(8), pp. 1392-1395, 2014. I was responsible for the experiment design, data collection, data analysis, and manuscript composition. A. Sampaleanu designed the transducer, and D. Rishi contributed to data collection. R. J. Zemp was the supervisory author and was involved with concept formation and manuscript composition.

Chapter 4 of this thesis has been published as R. K. W. Chee and R. J. Zemp, "Feasibility of modulation encoded TOBE CMUTs for real-time 3D imaging," *IEEE transactions on ultrasonics, ferroelectrics, and frequency control*, 62(4), pp. 771-775, 2015. I was responsible for experiment design, data collection, data analysis, and manuscript composition. R. J. Zemp was the supervisory author and was involved with concept formation and manuscript composition.

Chapter 5 of this thesis has been published as R. K. W. Chee, P. Zhang, M. Maadi, and R. J. Zemp, "Multifrequency interlaced CMUTs for photoacoustic imaging," *IEEE transactions on ultrasonics, ferroelectrics, and frequency control*, 64(2), pp. 391-401, 2017. I was responsible for the experiment design, data collection, data analysis, and manuscript composition. P. Zhang designed the transducer, and M. Maadi contributed to data collection. R. J. Zemp was the supervisory author and was involved with concept formation and manuscript composition.

Chapter 6 of this thesis has been prepared by R. K. W. Chee*, Y. Li*, W. Zhang, R. E. Campbell, and R. J. Zemp, “In vivo multiplexed photoacoustic molecular imaging with far-red photoswitchable chromoproteins,” (Soon to be submitted, 2018). *Both authors contributed equally to this paper. I was responsible for the experiment design, system development, conceiving demixing concepts, data collection, algorithm development, data analysis, and manuscript composition. Y. Li was responsible for protein engineering including directed evolution, wet lab work, data collection and analysis pertaining to non-photoacoustic characterization, and manuscript composition pertaining to protein engineering and non-photoacoustic characterization. W. Zhang created the variant of GAF2 for which Y. Li further evolved to create sGPC2 and sGPC3. R. E. Campbell and R. J. Zemp were the supervisory authors and were involved with concept formation and manuscript composition.

Chapter 7 of this thesis has been prepared by R. K. W. Chee, A. K. Azad, A. G. Murray, and R. J. Zemp, “Photoacoustic tumour volume estimation for p110β knockout study,” (Unsubmitted, 2018). This paper aimed to answer whether photoacoustic imaging could be used as a quantitative measure comparable to traditional staining histology. This was part of a larger study led by A. K. Azad and A. G. Murray (supervisory author) to investigate whether p110β plays a role in tumour angiogenesis. For this paper relating to photoacoustic imaging, I was responsible for the experiment design, data collection, data analysis, and manuscript composition. A. K. Azad was responsible for sample preparation and contributed to experiments. A. G. Murray assisted with concept formation. R. J. Zemp was the supervisory author and was involved with concept formation and manuscript composition.

Acknowledgements

I would like to thank Dr. Roger Zemp for his support, patience, and encouragement. Thank you for guiding me in my growth as an academic and professional. Your passion and ambition in your career has been inspirational and insightful. Thank you for the incredible mentorship you have shown me. I would not be here today without your continued support of my endeavours and interests.

I would like to thank Dr. Robert Campbell and Yan Li for providing an engaging multidisciplinary opportunity to work with novel photoswitchable chromproteins. I am particularly grateful for the work that Yan has done.

My PhD has been a challenging but rewarding adventure that would not have been the same without the amazing colleagues and friends that have journeyed with me. Thank you to everyone who has been a part of this period in my life in any way. Your companionship and interactions, big or small, have helped shape me and brighten my life.

Thank you to my parents for their love and support. You have worked tirelessly to help your children live a better life, and I am grateful for the many sacrifices that you have made. Thank you to my older sister, Melissa Chee, for the enormous influence she has had on my life. You are the best sister, friend, and advisor that I could ask for.

I gratefully acknowledge funding from the Natural Sciences and Engineering Research Council of Canada (NSERC) for a Doctoral Alexander Graham Bell Canada Graduate Scholarship (CGS D) and the Alberta Innovates Technology Futures for a Graduate Student Scholarship.

Funding for this research has been generously provided by a number of sources including NSERC (NSERC RGPIN355544, STPGP494293-16), the Canadian Cancer Society (CCS 2011-700718, CCS 702032), the Canadian Institutes of Health Research (CIHR PS153067, CPG134739), Prostate Cancer Canada (PCCMVPRDG D2013-40, PCCMVPRDG D2015-04), and the Brain Canada Platform.

List of Symbols

- A_e: specific optical absorption
- c: speed of sound or column number
- C: concentration or capacitance
- C_V: specific heat capacity at constant volume
- d: diameter or distance
- E: voltage
- f: focal length
- i: current
- k: isothermal compressibility
- K_s: coefficient of stiffness
- P: pressure wave
- r: row number or observation field point
- q: charge
- R: reflection coefficient
- R_s: radius of sphere
- t: time
- T: temperature
- U: Heaviside step function
- V: volume or voltage
- Z: acoustic impedance
- β: thermal coefficient of volume expansion
- Γ: Grüneisen parameter
- $\Delta\omega_m$: change in modulation frequency
- ε: extinction coefficient

- η^{th}: percentage converted into heat
- λ: wavelength
- μ_a: optical absorption coefficient
- υ_s: speed of sound
- ρ: mass density
- σ: standard deviation
- φ: angle
- Φ: optical fluence
- ω_c: modulation frequency applied to column
- ω_m: base modulation frequency

List of Abbreviations

- AF: accumulated fluence
- ANSI: American National Standards Institute
- AR-PAM: acoustic-resolution photoacoustic microscopy
- A-scan: single image column containing depth and intensity
- B-scan: extension of an A-scan in two dimensions
- BV: biliverdin
- CMOS: complimentary metal-oxide-semiconductor
- CMUT: capacitive micromachined ultrasonic transducer
- CNR: contrast-to-noise ratio
- C-scan: extension of an A-scan in three dimensions
- CT: x-ray computed tomography
- DFG: delay function generator
- FG: function generator
- FWHM: full width at half maximum
- $f_\#$: f-number
- Hb: deoxygenated hemoglobin
- HbO_2: oxygenated hemoglobin
- H&E: hematoxylin and eosin
- ICP-DRIE: inductively-coupled plasma deep-reactive ion etching
- KO: knockout
- KOH: potassium hydroxide
- LPCVD: low pressure chemical vapour deposition
- LPF: low pass filter
- LTO: low temperature oxide

- MB: methylene blue
- MEL: melanin
- MEMS: microelectromechanical system
- MRI: magnetic resonance imaging
- Mw: molecular weight
- NEC: noise-equivalent concentration
- NS: nonspecific
- NT: nontransfected
- OR-PAM: optical-resolution photoacoustic microscopy
- PA: photoacoustic
- PACT: photoacoustic tomography
- PAGE: polyacrylamide gel electrophoresis
- PAM: photoacoustic microscopy
- PBS: phosphate-buffered saline
- PC: personal computer
- PCR: polymerase chain reaction
- PD: photodiode
- PECVP: plasma-enhanced chemical vapor deposition
- PET: positron emission tomography
- PI3K: phosphoinositide 3-kinase
- pMUT: piezoelectric micromachined ultrasonic transducer
- QY: quantum yield
- RMS: root mean square
- SEM: scanning electron microscope
- Si_3N_4: silicon nitride
- SNR: signal-to-noise ratio

- SOI: silicon on insulator
- sO_2: oxygen saturation
- sPA: spectroscopic photoacoustic
- SR-PAM: super-resolution photoacoustic microscopy
- TEOS: tetraethyl orthosilicate
- TOBE: top orthogonal to bottom electrode
- US: ultrasound
- VEGF: vascular endothelial growth factor

List of Figures

List of Tables

Table of Contents

1. Introduction

1.1 Brief Synopsis of Thesis

Photoacoustic (PA) imaging is an exciting and relatively new imaging technique allowing unprecedented high-resolution images in vivo up to several centimeters deep in tissue. In PA imaging, a laser induces heating in a target which causes rapid expansion and the generation of ultrasonic waves or PA signals, which can be detected with an ultrasound transducer. PA microscopy has been able to image capillaries in vivo, a feat that can be achieved due to its high resolution and sensitivity [1]. PA imaging can obtain soft tissue contrast and relative target concentrations by demixing images taken at multiple laser wavelengths. PA demixing has been used to determine functional parameters like total hemoglobin and blood oxygen saturation [2]. There is substantial interest in PA imaging due to the numerous medical and scientific applications. PA imaging has significant potential for oncology in detecting and managing cancers [3]. This includes the early stage detection of prostate cancer [4], the diagnosis and treatment of skin cancer [5], and the imaging of breast cancer [6, 7]. PA imaging may also help treat breast cancer by providing intraoperative breast tumour margins during breast-conserving surgery [8]. PA imaging has promising applications in other fields of medicine as well including ophthalmology via ocular imaging [9-11] and cardiology via the imaging of vulnerable atherosclerotic plaques [12, 13]. In addition, PA imaging is a valuable molecular imaging tool for scientific research. Using molecular contrast agents like genetically encoded reporters [14], PA imaging can achieve deep molecular images in small animals [15, 16], allowing researchers to gain new insights into biochemical interactions in the body. Applications of PA molecular imaging include studying biochemistry, understanding disease mechanisms of action, detecting disease biomarkers, and aiding drug development. The ability to image several centimeters deep with relatively high resolutions and real-time imaging speeds make it a potentially highly valuable imaging technique for small animal research, which is the foundation for many modern scientific advances.

This thesis explores novel transducer technologies and optical reporters for 3D PA molecular imaging. In doing so, we will improve PA imaging technology, which will benefit many of the exciting applications mentioned above. To reach the full potential of 3D PA molecular imaging, several challenges still need to be addressed with regards to ultrasound transducer and molecular reporter technology.

Most PA imaging technologies have used piezoelectric ultrasound transducers. Piezoelectric transducers use materials that generate voltage with applied pressure and vice versa. For novel applications such as multifrequency imaging and fast large field-of-view 3D imaging, piezoelectric transducer technologies do not yet provide needed capabilities. To address these needs, we introduce novel architectures based on capacitive micromachined ultrasonic transducer (CMUT) technology. CMUTs are an alternative to traditional piezoelectric transducer technologies and are made possible by the modern advances in layer-by-layer microfabrication. They offer ultra-high receive sensitivities and the ability to develop novel architectures to achieve goals not easily achieved with piezoelectrics.

There is a need for large 2D array transducers for real-time 3D imaging of small animals like mice. However, there is significant complexity when dealing with large 2D arrays due to the large transmit-receive channel numbers required to address each element of the array. On-board beamforming is often implemented to reduce channel numbers, but it comes at the cost of decreased imaging speed and a lack of individual element addressing. To address this, we introduce top-orthogonal-to-bottom-electrode (TOBE) CMUTs for PA imaging. This crossed electrode design reduces the total channel requirements to only those required to access rows and columns without the need for on-board beamforming electronics. The crossed electrode design also lends itself to a novel method for fast 3D PA imaging using modulation encoding. Modulation encoding encodes the signals from multiple elements on different carrier frequencies allowing faster imaging with the already reduced channel requirements.

Multifrequency imaging is especially important for PA molecular imaging because PA signals have a very broad bandwidth. Fine microvasculature will have high-frequency PA signals, but large, diffuse molecular contrast agent distributions often having PA signals frequencies that are too low to be detected by clinical ultrasound transducers. Sensitivity to molecular contrast agent distributions is essential to PA molecular imaging, while visualization of fine microvasculature is important for understanding aspects of diseases such as angiogenesis in cancer. For multifrequency imaging, we introduce interlaced multifrequency CMUTs that have interlaced high- and low-frequency elements for the detection of both high-and low-frequency PA signals. This means that PA signals from both fine vessel structures and diffuse molecular reporters can be detected with the same transducer due to its ultrawide bandwidth. The interlaced multifrequency design also reduces grating lobes, resulting in reduced imaging artifacts.

Even with ultrawide bandwidth transducers, PA molecular imaging may still struggle to provide highly sensitive molecular imaging capabilities. One reason for this is the large background signal present due to blood and other pigments which may obscure weak signals from weak reporters. Recently, Yao et al [17] introduced a novel photoswitchable reporter (BphP1) which can reduce background PA signals by switching between 2 absorption states via exposure to light of certain wavelengths. Images can be taken at each absorption state, and the two resulting images can be subtracted from one another to remove the unchanged background signal. However, this approach with a single reporter did not offer capabilities of multiplexed imaging of multiple reporters which would be transformative for better understanding complex signaling pathways. We collaborated with the Robert Campbell group to extend the palette of near-infrared photoswitchable reporters (sGPC2 and sGPC3) and introduce a novel method to multiplex multiple photoswitchable reporters known difference-spectra demixing. We use difference-spectra demixing to simultaneously image and differentiate photoswitchable sGPC2 and BphP1 in vivo and thus present the first multiplexed low-background PA molecular images.

Finally, as an example application, we explore the capabilities of PA imaging to quantitatively access metastasis in a study of the effects of p110β deletion on tumour angiogenesis. With its depth penetration and high resolution, PA imaging has significant potential to be used for longitudinal small animal studies allowing scientists to potentially analyze a mouse in vivo throughout the entire time course of a study rather than sacrificing mice at different time points to do ex vivo analysis. As a first step, we compare ex vivo tumour volume estimations obtained via PA imaging to that obtained with staining histology to determine the accuracy of PA histology.

1.2 Major Contributions

Chapters 3 to 7 consist of research done during the course of this thesis, some of which have been published or submitted in peer-reviewed scientific journals. The major contributions for chapters 3 to 7 are described as follows. Co-author contributions have previously been described in the preface. The following only describes the novelty and impact of each publication.

Chapter 3. R. K. Chee, A. Sampaleanu, D. Rishi, and R. J. Zemp, "Top orthogonal to bottom electrode (TOBE) 2-D CMUT arrays for 3-D PA imaging," *IEEE Transactions on Ultrasonics, Ferroelectrics, and Frequency Control*, *61*(8), pp. 1393-1395, 2014.

Large ultrasound transducer arrays are required to image large fields-of-view in PA imaging. Large fields-of-view are essential for acquiring meaningful information from a PA image. Array size is typically limited because of the number of transmit-receive channels required to control all elements of the array. An N×N array has N^2 elements, so even a relatively small 1024×1024 array will already have 1048576 elements, requiring a transmit-receive channel each for full array control. The large transmit-receive channel numbers add significant design complexity. TOBE CMUTs allow larger ultrasound transducer arrays to be created with reduced complexity while retaining individual element control. Its crossed electrode design reduces the number of transmit-receive channels required to control an N×N array from N^2 to N transmit-receive channels. We demonstrate the potential for TOBE CMUTs for 3D PA imaging, thus showing the potential to use TOBE CMUTs to create large transducer arrays for large field-of-view 3D PA imaging.

Chapter 4. R. K. Chee and R. J. Zemp, "Feasibility of modulation-encoded TOBE CMUTS for real-time 3-D imaging," *IEEE Transactions on Ultrasonics, Ferroelectrics, and Frequency Control*, *62*(4), pp. 771-775, 2015.

3D PA imaging has the potential to image at high frame rates, which would allow researchers unprecedented imaging capabilities deep in vivo. Unfortunately, large transducer arrays typically have slow 3D imaging speeds because integrated beamforming electronics are implemented to reduce the number of transmit-receive channels. These integrated beamforming electronics beamform one 2D plane at a time, requiring a 3D image to be acquired slice by slice. Thus, the imaging speed is reduced by the number of 2D slices that compose the 3D image. In TOBE CMUTs, imaging speed is also reduced because PA signals must be acquired column by column resulting in decreasing imaging speed with increasing array size. We introduce a novel method to acquire signals from all columns at once, allowing fast imaging speeds regardless of array size and number of 2D slices while maintaining low channel numbers. This method is called modulation encoding which takes advantage of the crossed electrode TOBE CMUT design to encode signals from different columns in different frequency bands. Thus, we can potentially have fast 3D PA images with large fields-of-view, allowing us to see molecular interactions in vivo in real-time.

Chapter 5. R. K. Chee, P. Zhang, M. Maadi, and R. J. Zemp, "Multifrequency Interlaced CMUTs for PA Imaging," *IEEE Transactions on Ultrasonics, Ferroelectrics, and Frequency Control*, *64*(2), pp.391-401, 2017.

PA signals are composed of a very broad range of frequencies. Diffuse molecular contrast agents for example will have significantly lower frequencies than fine microvasculature. Typical imaging transducer are designed to detect high-frequencies, necessary for high resolution images, and thus may not be sensitive enough to detect low-frequency signals from diffuse molecular contrast agents. We compare the low-frequency PA signal content of large diffuse distributions with that of fine structures via simulation. We then introduce interlaced multifrequency CMUTs, capable of imaging both low- and high-frequency PA signals. Our interlaced design results in low- and high-frequency elements that are tightly spaced, which minimizes grating lobes for reduced imaging artifacts. We use out interlaced multifrequency CMUTs to create co-registered high- and low-frequency PA images with minimal artifacts, thus combining the sensitivity to diffuse molecular contrast agents with high-resolution images of fine structures.

Chapter 6. R. K. Chee*, Y. Li*, W. Zhang, R. E. Campbell, and R. J. Zemp, "In vivo multiplexed PA molecular imaging with far-red photoswitchable chromoproteins," (Soon to be submitted 2018). *Both authors contributed equally to this paper.

Molecular PA imaging is limited due to high blood background signals which limit contrast agent sensitivity. To improve molecular contrast agent sensitivity, photoswitchable reporters were developed that could switch between two absorption states. Thus, an image could be taken at each of the absorption states and subtracted from each other. The background would be reduced because it does not change while the reporter signal would remain due to the difference in PA signal intensity at each absorption state. However, more photoswitchable reporters are necessary in order to image multiple targets in a complex molecular process. We introduce a second photoswitchable reporter (sGPC2) for use in multiplexed PA molecular imaging. In addition, we introduce a novel demixing technique to improve the multiplexing of photoswitchable reporters. We developed a PA imaging system for multiplexed imaging of photoswitchable molecular contrast agents and present the first multiplexed low-background PA molecular images.

Chapter 7. R. K. W. Chee, A. K. Azad, A. G. Murray, and R. J. Zemp, “PA tumour volume estimation for p110β knockout study,” (Unsubmitted 2018)

PA imaging has great potential as a quantitative research tool. PA imaging could one day allow histology to be performed multiple times in vivo throughout a longitudinal research study. We take a first step by comparing the accuracy of PA imaging with that of traditional staining histology ex vivo. We apply PA imaging to a study analyzing the effects of p110β deletion on tumour angiogenesis. We explore the capability of PA imaging to quantitatively access tumour volumes and compare mean PA sample values with measurements from traditional staining histology.

1.3 Organization of Thesis

Chapter 2 contains background information and references to prior work necessary for understanding the research done in this thesis. It provides an overview of molecular imaging and the various imaging techniques used, PA imaging principles and configurations, as well as ultrasound transducers used for PA imaging. Chapter 3 demonstrates the potential of TOBE CMUTs for PA imaging. Chapter 4 discusses the feasibility of modulation encoding in TOBE CMUTs for fast 3D PA imaging. Chapter 5 details the need for broadband transducers for PA imaging and introduces interlaced multifrequency CMUTs for improved broadband PA imaging. Chapter 6 introduces novel photoswitchable chromoproteins (sGPC2 and sGPC3) for reduced PA background signal. Chapter 6 also illustrates improved multiplexing using a novel demixing technique and presents the first multiplexed molecular images of photoswitchable chromoproteins. Chapter 7 contains an application of PA imaging to the quantitative analysis of tumour volumes in a study investigating the effects of p110β deletion on tumour angiogenesis. Finally, Chapter 8 contains a summary of the thesis and ongoing work.

References

1. K. Maslov, H. F. Zhang, S. Hu, and L. V. Wang, "Optical-resolution photoacoustic microscopy for in vivo imaging of single capillaries," Opt. Lett. **33,** 929-931 (2008).

2. X. Wang, X. Xie, G. Ku, L. V. Wang, and G. Stoica, "Noninvasive imaging of hemoglobin concentration and oxygenation in the rat brain using high-resolution photoacoustic tomography," J. Biomed. Opt. **11,** 024015 (2006).

3. K. S. Valluru, K. E. Wilson, and J. K. Willmann, "Photoacoustic Imaging in oncology: translational preclinical and early clinical experience," Radiology **280,** 332-349 (2016).

4. A. Agarwal, S. Huang, M. Oâ€™donnell, K. Day, M. Day, N. Kotov, and S. Ashkenazi, "Targeted gold nanorod contrast agent for prostate cancer detection by photoacoustic imaging," J. Appl. Phys. **102,** 064701 (2007).

5. J. Oh, M. Li, H. F. Zhang, K. Maslov, and L. V. Wang, "Three-dimensional imaging of skin melanoma in vivo by dual-wavelength photoacoustic microscopy," J. Biomed. Opt. **11,** 034032 (2006).

6. R. A. Kruger, C. M. Kuzmiak, R. B. Lam, D. R. Reinecke, S. P. Del Rio, and D. Steed, "Dedicated 3D photoacoustic breast imaging," Med. Phys. **40,** (2013).

7. D. Piras, W. Xia, W. Steenbergen, T. G. van Leeuwen, and S. Manohar, "Photoacoustic imaging of the breast using the twente photoacoustic mammoscope: present status and future perspectives," IEEE Journal of Selected Topics in Quantum Electronics **16,** 730-739 (2010).

8. L. Xi, S. R. Grobmyer, L. Wu, R. Chen, G. Zhou, L. G. Gutwein, J. Sun, W. Liao, Q. Zhou, and H. Xie, "Evaluation of breast tumor margins in vivo with intraoperative photoacoustic imaging," Optics express **20,** 8726-8731 (2012).

9. A. de La Zerda, Y. M. Paulus, R. Teed, S. Bodapati, Y. Dollberg, B. T. Khuri-Yakub, M. S. Blumenkranz, D. M. Moshfeghi, and S. S. Gambhir, "Photoacoustic ocular imaging," Opt. Lett. **35,** 270-272 (2010).

10. Z. Hu, X. Wang, Q. Liu, and Y. Paulus, "Photoacoustic imaging in ophthalmology," Int J Ophthalmol Eye Res **3,** 126-132 (2015).

11. G. Xu, Y. Xue, Z. G. Ã–zkurt, N. Slimani, Z. Hu, X. Wang, K. Xia, T. Ma, Q. Zhou, and H. Demirci, "Photoacoustic imaging features of intraocular tumors: Retinoblastoma and uveal melanoma," PloS one **12,** e0170752 (2017).

12. K. Jansen, Van Der Steen, Antonius FW, H. M. van Beusekom, J. W. Oosterhuis, and G. van Soest, "Intravascular photoacoustic imaging of human coronary atherosclerosis," Opt. Lett. **36,** 597-599 (2011).

13. S. Sethuraman, J. H. Amirian, S. H. Litovsky, R. W. Smalling, and S. Y. Emelianov, "Spectroscopic intravascular photoacoustic imaging to differentiate atherosclerotic plaques," Optics express **16,** 3362-3367 (2008).

14. L. Li, R. J. Zemp, G. F. Lungu, G. Stoica, and L. V. Wang, "Photoacoustic imaging of lacZ gene expression in vivo," J. Biomed. Opt. **12,** 020504 (2007).

15. A. P. Jathoul, J. Laufer, O. Ogunlade, B. Treeby, B. Cox, E. Zhang, P. Johnson, A. R. Pizzey, B. Philip, and T. Marafioti, "Deep in vivo photoacoustic imaging of mammalian tissues using a tyrosinase-based genetic reporter," Nature Photonics **9,** 239 (2015).

16. Q. Fan, K. Cheng, Z. Yang, R. Zhang, M. Yang, X. Hu, X. Ma, L. Bu, X. Lu, and X. Xiong, "Peryleneâ€□Diimideâ€□Based Nanoparticles as Highly Efficient Photoacoustic Agents for Deep Brain Tumor Imaging in Living Mice," Adv Mater **27,** 843-847 (2015).

17. J. Yao, A. A. Kaberniuk, L. Li, D. M. Shcherbakova, R. Zhang, L. Wang, G. Li, V. V. Verkhusha, and L. V. Wang, "Multiscale photoacoustic tomography using reversibly switchable bacterial phytochrome as a near-infrared photochromic probe," Nature methods **13,** 67 (2016).

2. Background

2.1 Molecular Imaging

Molecular imaging is the imaging of biological processes in vivo by targeting specific molecules [1, 2]. This has significant potential for scientific discovery and medicine as it allows researchers to uncover the biochemical and molecular causes behind morphological changes in the body. Molecular imaging has already had a significant impact of numerous fields including oncology [1, 3-6], drug development [7-10], immunology [11, 12], neuroscience [13-15], cardiology [13, 16-18], and theranostics [13, 19] among others.

2.1.1 Molecular Imaging Modalities

There are many imaging techniques capable of molecular imaging, and each technique has its own probes for molecular targeting [7, 20]. The main molecular imaging methods include magnetic resonance imaging (MRI), x-ray computed tomography (CT), positron emission tomography (PET), and optical imaging. In addition to these, photoacoustic (PA) imaging is an emerging molecular imaging technique that has promising potential for the future. No one imaging modality is suitable in also cases, and each have their own advantages and disadvantages. The table below shows how these imaging modalities compare.

Imaging Modalities	Depth Penetration	Resolution	Acquisition Time	Soft-Tissue Contrast	Ionizing	Cost
MRI	Unlimited	High	Minutes to Hours	Excellent	No	High
CT	Unlimited	High	Minutes	Poor	Yes	Low
PET	Unlimited	Low	Minutes to Hours	Poor	Yes	High
Optical Imaging	≤ 1 cm	High	Real-Time to Minutes	Excellent	No	Low
PA	≤ 5 cm	High (Scalable)	Real-Time	Excellent	No	Low

Table 2.1. Comparison of molecular imaging modalities [20, 21].

2.1.1.1 Magnetic Resonance Imaging

MRI imaging is based on the response of magnetic dipoles, typically hydrogen atoms in water, to a strong magnetic field. A powerful magnetic field first aligns the hydrogen atoms, and then the magnetic field is removed. The hydrogen atoms will have varying relaxation times to their unaligned states based on their different tissue environments [2]. This provides excellent soft-tissue contrast with high resolution and whole body depth penetration without the use of ionizing radiation. Unfortunately, MRI requires a powerful uniform magnetic field typically generated from a superconducting magnet, which has both a high initial and maintenance cost. In addition, MRI has relatively slow imaging speeds requiring minutes to hours [20]. Common MRI probes for molecular imaging include iron oxide [22-24] and Gandolinium [24-26] based contrast agents. The main challenge for MRI as a molecular imaging method is the poor contrast agent sensitivity, which require very high potentially toxic contrast agent doses for detection [13].

2.1.1.2 X-Ray Computed Tomography

CT images are produced by firing x-rays through the body and measuring the amount that pass through. Multiple angles are used at a single position to reconstruct a tomographic slice. CT has high resolutions (50-200 µm, preclinical) and unlimited depth penetration, but have poor soft-tissue contrast and slow imaging rates (minutes) [13, 20]. In addition, CT imaging is ionizing due to the use of high energy x-rays. Nanoparticles such as targeted gold nanoparticles [27], NanoK [28], and FePt [29] are used as molecular contrast agents in CT.

2.1.1.3 Positron Emission Tomography

PET creates images from the gamma radiation released from a decaying radiolabeled contrast agent placed in vivo. In PET, the gamma radiation is released when a decaying radionuclide releases a positron which collides with a neighboring electron [13, 30]. Similarly a related technique known as single-photon emission computed tomography detects gamma radiation that is directly produced from a decaying radionuclide [13, 30]. The disadvantages of PET include relatively low spatial resolutions (1-2mm) and the exposure to ionizing gamma rays [13]. Promising PET molecular contrast agents include [^{18}F]fluoro-2-deoxy-D-glucose and 3′-deoxy-3′-[^{18}F]fluorothymidine [3, 31].

2.1.1.4 Optical Imaging

The two major optical imaging modalities are fluorescence imaging and bioluminescence imaging [30]. Fluorescence imaging involves the excitation of electrons in a target via light of a certain wavelength. These electrons are excited to an unstable excited state which quickly decays into a lower energy state while releasing energy in the form of light at a specific wavelength. Bioluminescence imaging involves a contrast agent that produces light via a chemical reaction. In both cases, the emitted light is detected using sensitive charge coupled detectors [30]. One of the advantages of optical imaging is being able to easily multiplex different contrast agents with different absorption spectra [2]. Multiplexing is especially important in molecular imaging because biological processes are often complex interactions involving multiple targets. Fluorescence imaging has advantages such as low cost, multiplexing capabilities, and no required substrate administration [13]. Limitations include < 1 cm depth penetration, background fluorescence, and relatively low sensitivity [13]. In comparison, bioluminescence imaging has higher sensitivity and lower background signal, but it is limited by depth penetration and the administration of bioluminescent substrates [13]. Bioluminescence is produced by the luciferase enzymes such as FLuc, RLuc, and GLuc [13]. Fluorescence imaging uses genetically-encoded proteins as molecular contrast agents, which allow expression within the cell and thus visualization of biochemistry and gene expression [32-34]. Fluorescent contrast agents include green fluorescent protein and its derivatives which have had a huge impact on scientific discovery [35].

2.1.1.5 Photoacoustic Imaging

PA imaging is a promising relatively new molecular imaging modality that relies on the detection of ultrasound generated by laser induced thermoelastic expansion of tissue. One of the main advantages of PA imaging is that it can achieve high scalable resolution beyond the typical depth range of optical imaging, up to approximately 5 cm deep [13, 36]. Its resolution at a depth of 1-5 cm is higher than can be achieved by other imaging modalities. Similarly to fluorescence imaging, PA imaging can take advantage of powerful genetically-encoded proteins for molecular imaging. There are a host of genetic reporters that can be used for PA imaging, which include existing fluorescent genetic reporters [37]. Since fluorescence and PA imaging both rely on optical absorption, many fluorescent reporters can be used as PA reporters. Molecular PA contrast agents include both genetic reporters like iRFP, BphP1, and Dronpa [37] as well as targeted nanoparticles [38, 39]. PA imaging is also able capable of multiplexed molecular imaging, which is essential for imaging complex molecular processes.

2.1.2 Real-Time 3D Molecular Imaging

There is currently no molecular imaging technique capable of taking real-time, high-resolution 3D molecular images of whole small animal bodies. 3D molecular images of small animals would have significant potential to drive new scientific discoveries. Modalities such as MRI, CT, and PET have the depth penetration and field of view but lack either imaging speed or resolution. Bioluminescence imaging is capable of 3D molecular imaging, but acquisitions could take minutes, and it has poor resolution when imaging deep [40]. Real-time imaging has been demonstrated for fluorescence imaging [41], and 3D fluorescence imaging has been demonstrated in small animals, but poor resolution (3.5mm) were observed at depth [42]. PA imaging has shown significant promise for high-resolution, real-time 3D imaging. Current systems have been able to image 3D sections of a mouse in real-time with resolutions as low as 140 µm, but scanning is required for a full mouse [43, 44]. There are several technological challenges that prevent PA imaging from obtaining real-time 3D molecular images of a whole mouse. The first is the challenge of building large 2D ultrasound transducer arrays to acquire wide field-of-view 3D PA images. This is due to the complexity and cost of having a large numbers of transmit-receive channels to address all elements of a large 2D array. The second is the slow 3D image acquisition speeds that results from implementing integrated beamforming electronics for reduced channel numbers. The third is the low sensitivity to molecular contrast agents due to low PA signal frequencies and inherent PA blood background signals. All three of these will be discussed in more detail in the following sections.

2.2 Photoacoustic Imaging

PA imaging is a noninvasive imaging technique that detects acoustic waves generated in tissue via thermal laser stimulation. PA imaging can obtain high-resolution, real-time images of microvasculature up to several centimeters below the tissue surface with higher resolutions than other imaging techniques. This makes it a promising imaging method for imaging breast cancer [45-49], atherosclerotic plaques [50-53], and prostate cancer [54, 55] among others as well as an ideal imaging modality for small animal studies which make up the backbone of biomedical research [56, 57]. PA imaging makes use of the photoacoustic effect which was first discovered by Alexander Graham Bell in 1880 [21], which says that light absorbed by tissue with enough energy will result in rapid thermal expansion and a subsequent generation of an acoustic wave or PA signal. PA imaging uses pulsed lasers to generate PA signals in tissue, which can be detected using an ultrasound transducer.

2.2.1 Photoacoustic Principles

In PA imaging, a nanosecond laser pulse shines on a target causing heating and thus thermoelastic expansion resulting in an acoustic wave or PA signal. The time of travel of this acoustic wave to an ultrasound transducer can be used to identify where it originated from and thus reconstruct a PA image. The PA signal is proportional to the optical absorption of the wavelength of light and the intensity of the laser pulse, which is essential for determining accurate biological information from a PA image.

These proportional relationships result from two factors which are known as thermal and stress confinement. Thermal confinement means that the laser pulse is short enough so that no heat diffuses during irradiation by a single pulse [21]. Stress confinement means that the laser pulse is short enough so that no PA signal propagates during irradiation by a single pulse [21]. These two factors ensures that any PA signal generated is the result of a single laser pulse in its entirety. Nanosecond laser pulses are short enough to be in thermal and stress confinement for PA imaging in soft tissue.

We can derive the PA equation from the equation of the fractional change in target volume resulting from a laser pulse

$$(1) \qquad dV/V = -kP + \beta T$$

where V = volume, k = isothermal compressibility, P = pressure wave (PA signal), β = thermal coefficient of volume expansion, and T = temperature [21]. Thermal and stress confinement means that the volume changes caused by heat diffusion and pressure waves are negligible during the incident time of the laser, $dV/V = 0$. Thus the resulting thermoelastic expansion that occurs will be a result of the entire incident laser pulse as mentioned above. Thus the resulting pressure can be calculated from equation (1). Rearranging equation (1), we get

$$(2) \qquad P = \beta T/k = \beta/(k\rho C_V)\times(\eta^{th}A_e) = \beta/(k\rho C_V)\times(\eta^{th}\mu_a\,\Phi\,)$$

where A_e = specific optical absorption (J/m^3), η^{th} = percentage converted into heat, C_V = specific heat capacity at constant volume, ρ = mass density, μ_a = optical absorption coefficient, and Φ = optical fluence (J/cm^2) [21]. Rearranging equation (2), we get

$$(3) \qquad P = \Gamma\eta^{th}\mu_a\,\Phi$$

where Γ = Grüneisen parameter = $\beta/(k\rho C_V)$, μ_a = optical absorption coefficient, and Φ = optical fluence (J/cm^2) [21]. Equation (3) is the PA equation.

Equation (3) shows that PA signals are proportional to the optical fluence and the optical absorption coefficient. This means that higher optical fluence and optical absorption will result in better PA images. Unfortunately, optical fluence cannot be increased indefinitely, or it would result in safety issues such as burns. The American National Standards Institute (ANSI) has set the safe laser fluence limit for PA imaging to be 20 mJ/cm^2 [58, 59]. Since optical absorption coefficients also play a role in signal intensity, the best contrast agents have high absorption at the imaging wavelength of the laser. This can be found via their absorption spectrums. For deep in vivo imaging, there is an optical window (600-1100 nm) where blood has lower absorption allowing you to obtain PA images deeper in tissue [60].

Another important principle in PA imaging is spectral demixing. Spectral demixing is a technique used to estimate relative concentrations of optical absorbers within an image. This is used to produce functional PA images of hemoglobin concentration, oxygen saturation, and contrast agent concentrations among others. Thus, spectral demixing is essential for quantitative PA molecular images. Spectral demixing can be explained using the PA equation (3). Expanding equation (3), we get $P(\lambda) = \Gamma\mu_a(\lambda)\Phi$ where λ = wavelength because the absorption coefficient for a given substance varies with wavelength. The optical absorption coefficient when imaging a single contrast agent in tissue can be written as

$$(4) \qquad \mu_a(\lambda) = \varepsilon_{HbO_2}(\lambda)C_{HbO_2} + \varepsilon_{Hb}(\lambda)C_{Hb} + \varepsilon_{\mathrm{sGPC2}}(\lambda)C_{\mathrm{contrast\ agent}}$$

where ε = extinction coefficient, C = concentration, HbO_2 = oxygenated hemoglobin, and Hb = deoxygenated hemoglobin. There are 3 unknown concentrations in this case, so at least 3 PA images must be taken at 3 different wavelengths to create a system of equations that can be solved for the unknown concentrations. For N unknown concentrations, there will need to be at least N PA images taken at N different wavelengths. The system of equations can be written as

$$(5) \qquad \begin{bmatrix} P_1(\lambda_1) \\ \vdots \\ P_N(\lambda_N) \end{bmatrix} = \Gamma\Phi \begin{bmatrix} \Delta\varepsilon_1(\lambda_1) & \cdots & \Delta\varepsilon_N(\lambda_1) \\ \vdots & \ddots & \vdots \\ \Delta\varepsilon_1(\lambda_\mathrm{N}) & \cdots & \Delta\varepsilon_N(\lambda_N) \end{bmatrix} \begin{bmatrix} C_1 \\ \vdots \\ C_N \end{bmatrix}$$

Simplifying equation (5) to $P = \Delta\varepsilon C$, the solution for concentration can be written as $C = (\Delta\varepsilon)^{-1}P$. Thus, relative absorber concentrations can be obtained. Spectral demixing is the basis for quantitative measurements for molecular PA imaging [61] and has been used extensively to measure oxygen saturation (sO_2) in hemoglobin [62, 63]. Fig. 2.1 shows a spectrally demixed PA microscopy image of sO_2 in a living mouse ear using 561nm and 570nm imaging wavelengths.

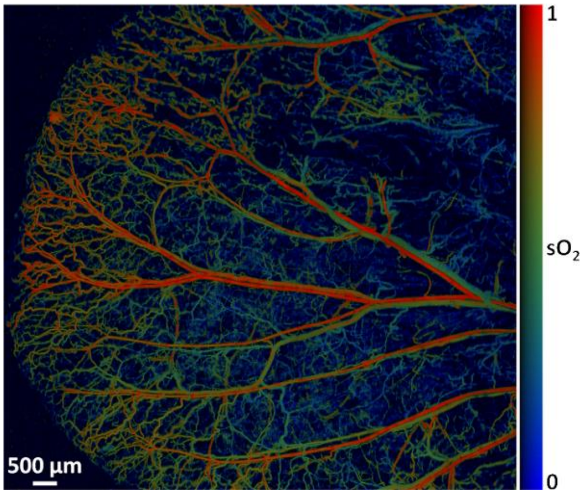

Figure 2.1. Spectrally demixed PA microscopy image of sO_2 in a living mouse ear [64].

2.2.2 Photoacoustic Imaging Configurations

PA imaging offers scalable resolutions, which means with increasing depth penetration there is decreasing lateral resolution. This span of resolution and imaging depth is covered using two main imaging configuration known as PA microscopy (PAM) and PA computed tomography (PACT). PACT has deeper penetration but lower resolutions in comparison to PAM. PAM can be further broken down into optical-resolution PA microscopy (OR-PAM) and acoustic-resolution PA microscopy (AR-PAM). Fig. 2.2 shows a comparison of the depth ranges achievable by OR-PAM, AR-PAM, and PACT.

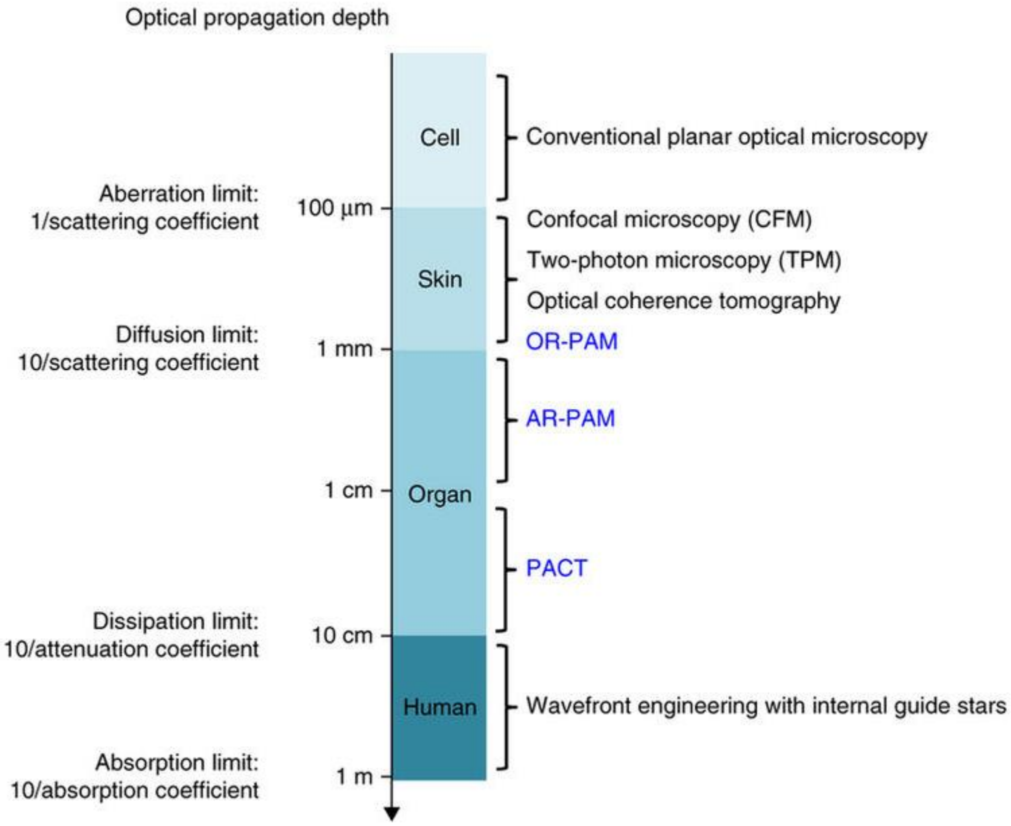

Figure 2.2. Comparison of the depths achievable by OR-PAM, AR-PAM, and PACT [65].

Sub-µm resolutions are obtainable with mm tissue penetration using OR-PAM, while several cm tissue penetration is possible with 100 µm resolutions using PACT. Fig. 2.3 shows the resolution comparison of the different PA imaging configurations. Super-resolution PAM (SR-PAM) is a special class of PA imaging which uses special techniques to break the optical diffraction limit. One example is subdiffraction PAM using photoswitchable chromoproteins like BphP1 [66]. Fig. 2.4 shows the general setup of various PA imaging configurations that will be referenced in the following sections.

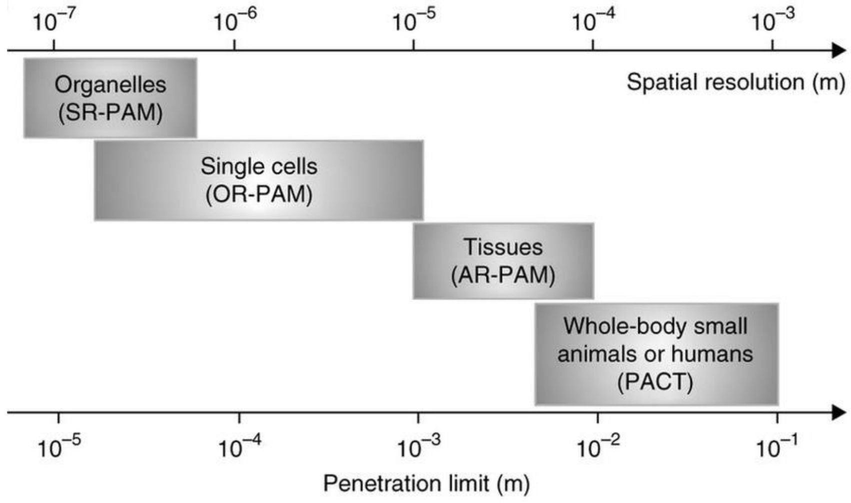

Figure 2.3. Comparison of the resolutions achievable by SR-PAM, OR-PAM, AR-PAM, and PACT [65].

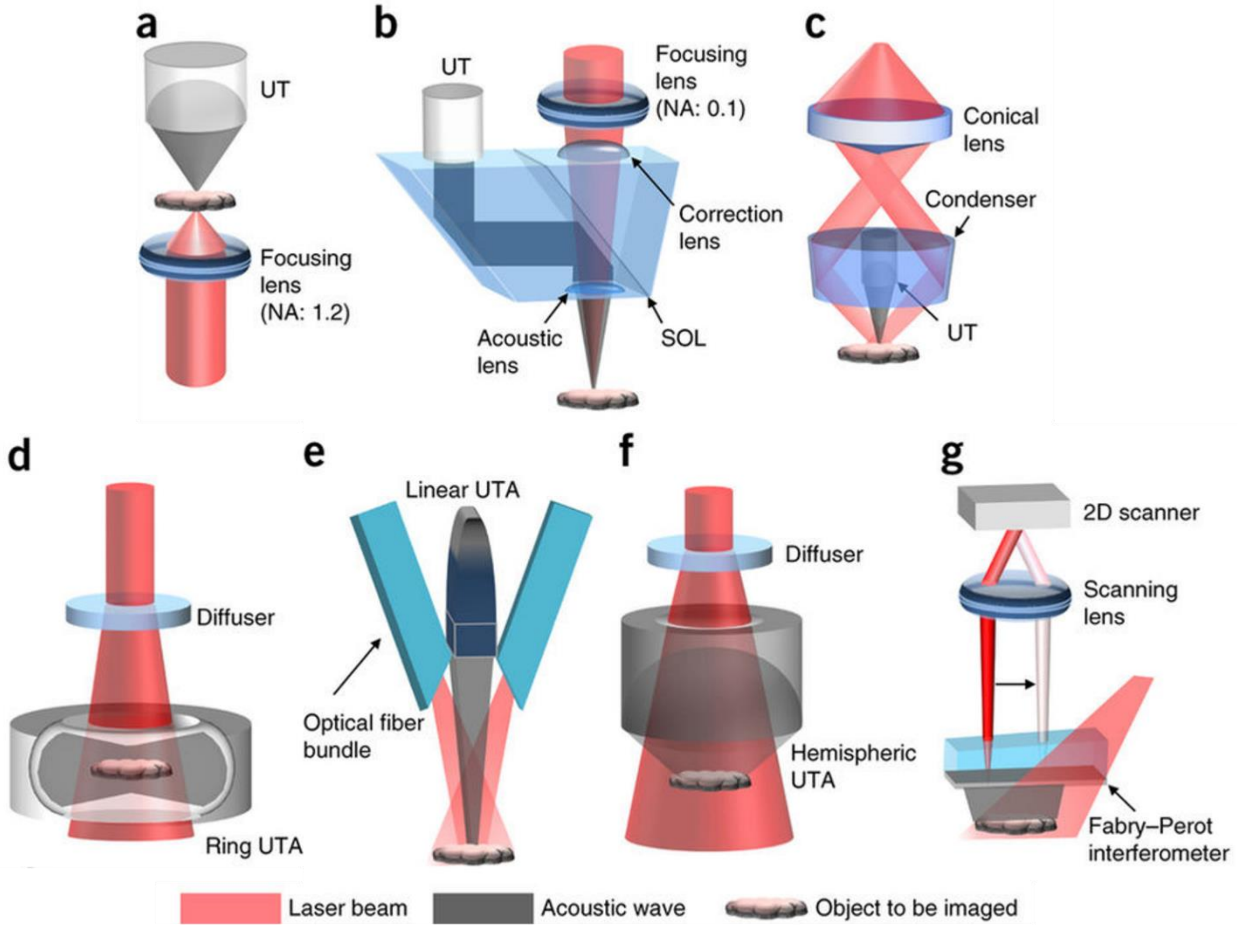

Figure 2.4. PA configuration setups: (a) transmission-mode OR-PAM system, (b) reflection-mode OR-PAM system, (c) AR-PAM system, (d) PACT system using ring array, (e) PACT system using linear array, (f) PACT using hemispherical array, and (g) Fabry-Perot PA setup [65].

2.2.2.1 Photoacoustic Microscopy

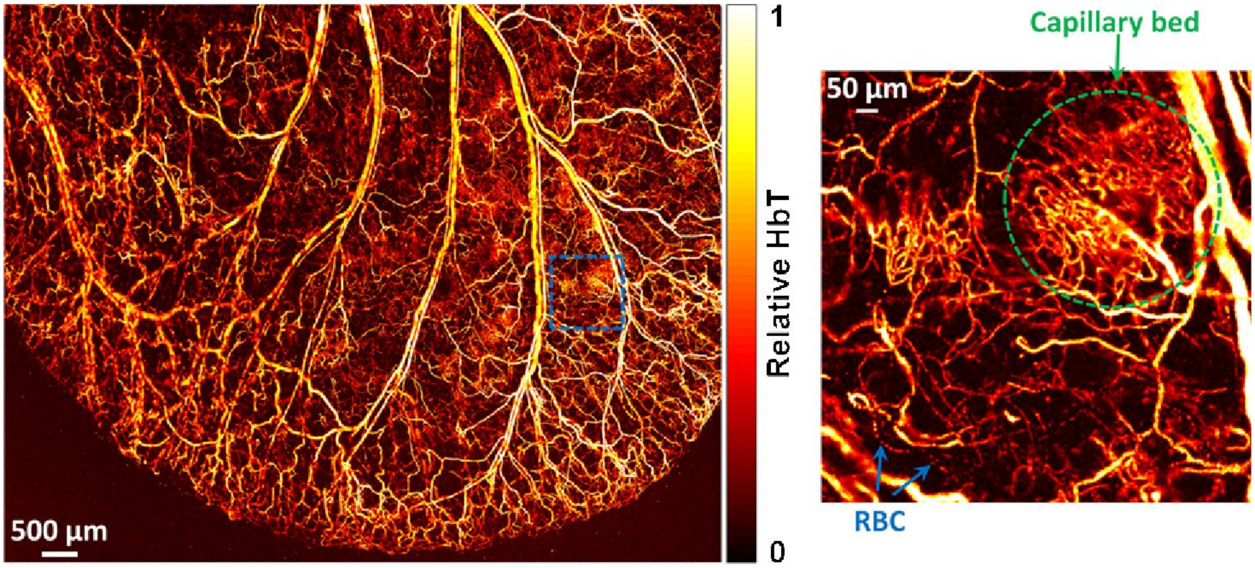

Figure 2.5. OR-PAM image of HbT in a living mouse ear. Capillary beds and red blood cells (RBC) are visible in the image [64].

PAM can divided into OR-PAM and AR-PAM. In both cases, a focused ultrasound transducer is used and the light is optically focused with a lens. The difference is that in OR-PAM the optical focus is tighter than the acoustic focus and vice versa for AR-PAM [65]. Thus for OR-PAM, resolutions approaching the diffraction limit of light are possible [64]. A system capable of switching between OR-PAM and AR-PAM, achieved 4.2 µm lateral resolution at ~1.4 mm imaging depth with OR-PAM and 45 µm lateral resolution at ~7.6 mm imaging depth with AR-PAM [67]. Fig. 2.5 shows an OR-PAM image of the total relative hemoglobin concentration (HbT) in a living mouse. Fig. 2.4 (a) and (b) are two examples of OR-PAM systems, while an AR-PAM system is shown in Fig. 2.4 (c). The lateral resolution of OR-PAM and AR-PAM can be estimated with the same equation, but with one using the optical focusing parameters and the other using the acoustic focusing parameters. The lateral resolution for PA microscopy is given by [68]

$$(6) \qquad Lateral\ Resolution = 1.22\frac{f}{d}\lambda$$

where is f = focal length of the lens (OR-PAM) or ultrasound transducer (AR-PAM), d = diameter of the lens (OR-PAM) or ultrasound transducer (AR-PAM), and λ = wavelength of light (OR-PAM) or center acoustic wavelength (AR-PAM).

The axial resolution is the same for all PA configurations including PAM and PACT. The axial resolution is inversely related to the transducer bandwidth [68] and can be represented as

$$(7) \qquad Axial\ Resolution = \frac{Speed\ of\ Sound\ in\ Tissue}{Bandwidth}$$

2.2.2.2 Photoacoustic Computed Tomography

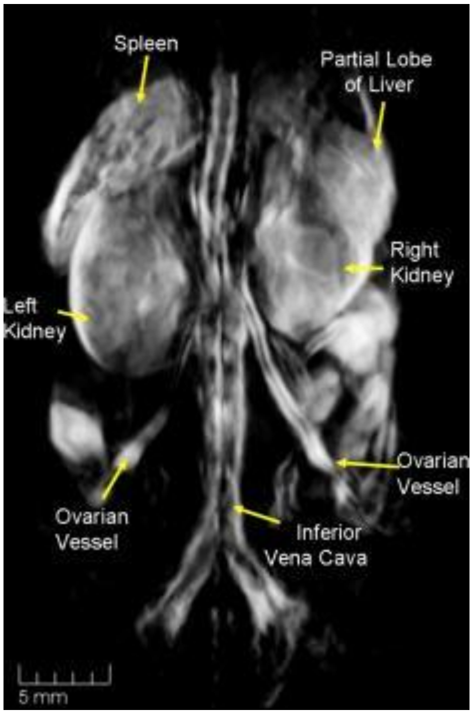

Figure 2.6. PACT image of a nude mouse abdomen obtained using a half-ring array. This image is a 3D image projection [69].

PACT involves wide-field illumination and image reconstruction from an array transducer [65]. PACT ultrasound transducers include linear arrays, 2D arrays, and ring arrays among others. Fig. 2.4 (d), (e), and (f) show PACT systems using a ring array, linear array, and hemispherical array, respectively. PACT has worse resolutions compared to PAM, but it is capable of penetrating deep in tissue, allowing 3D image reconstructions of small animals. PACT has reportedly imaged 5.2 cm deep in tissue with resolutions below 780 um [70]. Fig. 2.6 shows a PACT image of a nude mouse abdomen. The image is a 3D image projection and was obtained with a half-ring array.

The lateral resolution for PA tomography can be represented as [71]

$$(8) \qquad Lateral\ Resolution = 1.42 f_{\#} \lambda$$

where $f_{\#}$ = f-number = focal length of transducer/diameter of a disk transducer and λ = wavelength of light. The axial resolution of PACT can be represented by equation (7) except in the case of PACT using a ring array, where the axial resolution is equivalent to the lateral resolution due to the surrounding transducer positioning.

Different reconstruction methods can be used to recreate 2D and 3D PACT images from the received PA signals. The most common method is universal backprojection (UBP) [57, 72], which is the more general case of the simpler delay-and-sum beamforming. In UBP, the time a signal arrives predicts a hemispherical location of possible sources. By projecting back received signals from all transducer elements, we can quickly get an accurate PACT image. Another popular reconstruction method is time-reversal (TR), which uses model-based simulations to predict the source of a received signal [57, 73]. Full-wave TR can potentially create better PACT images than UBP in heterogeneous media with a priori speed of sound information, but it requires significantly more time. In addition, other methods for image reconstruction also exist including other model-based methods [74-76] and Fourier transform methods [77, 78]. Delay-and-sum beamforming will be used for PACT reconstruction in this thesis work.

Whether in PAM or PACT, common imaging terminology such as A-scan, B-scan, and C-scan are used to describe images. A-scans are single image columns that contains depth and intensity such as a single column in a 2D image. B-scans are extensions of an A-scan in two dimensions such as an entire 2D image. C-scans are extensions of A-scans in three dimensions and are 3D images. Sometimes 2D images are created from C-scans by plotting only the maximum intensity pixel in depth. These are known as maximum intensity projections. Fig. 2.1 and 2.5 are examples of maximum intensity projections.

2.2.3 Photoacoustic Molecular Imaging Sensitivity

Molecular PA imaging sensitivity is limited by significant background blood signals. This can be the case even when imaging within the optical window of 600-1100 nm. PA molecular contrast agents must be developed with higher contrast or background reducing capabilities to compensate for the high blood background. One approach is to optimize fluorescent reporter proteins for PA imaging via directed evolution to reduce their quantum yield [79]. Another approach is to develop photoswitchable reporters capable of reducing background signals. This will be the topic of Chapter 6. Even with enhanced reporter sensitivity, PA molecular imaging requires multiplexing capabilities to image the interactions of multiple targets simultaneously. A novel method to demix multiple photoswitchable reporters will also be discussed in Chapter 6.

2.3 Ultrasound Transducers

Ultrasound transducers have had a long history in biomedical imaging most notably in ultrasound imaging. In recent years, ultrasound transducers have also proven essential for PA imaging. PA signals are essentially just ultrasound waves that have been generated by rapid expansion of a target due to heating by light. Ultrasound transducers detect these PA signals and convert them into electrical signals for image reconstruction.

2.3.1 Ultrasound Imaging Fundamentals

For PACT, PA images are often overlaid on an ultrasound image background. This is possible because a PA transducer is essentially an ultrasound transducer capable of receiving and transmitting ultrasound signals. For this reason, it is important to understand some fundamentals about ultrasound imaging.

To generate an ultrasound image, an ultrasound transducer must transmit ultrasound waves which will reflect off of targets back to the transducer. The total time of flight of the transmitted signal indicates the time required to travel to the target and back. The distance of the target can thus be calculated with equation (9)

$$(9)\ d = \frac{c \times t}{2}$$

where d = distance from the transducer to the target, c = speed of sound in the transmit medium, and t = total time of flight for the transmitted signal. Ultrasound reflection is caused by an acoustic impedance mismatch. The acoustic impedance of the transmit medium is defined with equation (10)

$$(10)\ Z = \rho \times c = \sqrt{\rho \times K_s}$$

where Z = acoustic impedance, ρ = transmit medium density, c = speed of sound in the medium, and K_s = the coefficient of stiffness of the medium. The strength of ultrasound reflection is defined by the refection coefficient represented by equation (11)

$$(11)\ R = \frac{(Z_2 - Z_1)^2}{(Z_2 + Z_1)^2}$$

where R = reflection coefficient, Z_1 = acoustic impedance of the initial transmit medium, and Z_2 = acoustic impedance of the encountered transmit medium. Common acoustic impedances include 1.67 for blood/whole body, 1.47 for water, 7.9 for bone, and 0.000413 for dry air [80]. From equation (11), we can derive why bone has such a strong reflection when taking ultrasound images in the body. Likewise, air also has strong reflections when coupling with most media. To reduce reflection from air between an ultrasound transducer and the body, ultrasound gels are used, which have acoustic impedances close to that of water. One of the advantages of capacitive micromachined ultrasonic transducers (CMUTs), which will be discussed in the following sections, is that they can be designed to have better acoustic impedance matching.

Finally, grating lobes should also be discussed regarding their negative effects on the receive capabilities of an ultrasound transducer and how they can be avoided. Grating lobes are symmetric structures located around the center frequency of a transducer in the frequency domain [80] and can result in undesirable imaging artifacts. They are caused by inter-element transducer spacings that are greater than half of the shortest received acoustic wavelength, assuming beam steering angles from –π/2 to π/2 [80]. This can be derived from the Nyquist sampling criterion. In practice, inter-element spacings may be as large as half the center frequency wavelength of the transducer, assuming practical beam steering angles of –π/4 to π/4 [80]. For PA signal receive, where there is no beam steering, the inter-element spacings can be as large as the center frequency wavelength of the transducer and still minimize grating lobes. In the work in this thesis involving multifrequency CMUTs, we interlaced elements of different center frequency to reduce inter-element spacing between those of the same center frequency and thus reduce grating lobes in the multifrequency transducer.

2.3.2 Types of Ultrasound Transducers

Two major types of ultrasound transducers discussed in this thesis are piezoelectric transducers and CMUTs. In addition, there are several less common transducer types that include Fabry-Perot transducers, piezoelectric micromachined ultrasonic transducers (pMUTs), and relaxor arrays. CMUTs will be the main focus of the transducer related advancements presented in this thesis.

2.3.2.1 Piezoelectric Transducers

The piezoelectric effect is the production of a charge across of certain solids when a mechanical force is applied, and was first discovered by the Curie brothers in 1880 [81, 82]. Piezoelectric transducers are based on the piezoelectric effect and were the first ultrasound transducer used during the development of ultrasound imaging for biomedical uses in 1949 [83]. The frequency of a piezoelectric transducer is determined by the thickness of the piezoelectric material. In comparison to other ultrasound transducers, it has relatively low bandwidth, which negatively affects PA axial resolution as described by equation (7). In addition, these low bandwidth are less ideal for detecting all PA signals which can have very broad frequency bands. Peizoelectric transducers have the highest transmit pressures of all ultrasound transducers, which are beneficial for ultrasound imaging but are less important for PA imaging.

2.3.2.2 Capacitive Micromachined Ultrasonic Transducers

The development of CMUTs began in the early 1990s and grew as a result of the advances in micromachining technology [84]. The early developments of CMUTs were pioneered by the work of the Khuri-Yakub group [84-89]. CMUTs have since become a promising alternative to piezoelectrics as a result of having better acoustic impedance matching, wider bandwidth, and easier fabrication for large complex arrays [84, 90]. The easier fabrication of CMUTs is especially valuable in developing new complex architectures. One such example is the top-orthogonal-to-bottom-electrode (TOBE) CMUT, which has been shown to reduce channel requirements in large imaging arrays [91].

CMUTs consist of a membrane over a cavity with a top electrode on the membrane and bottom electrode beneath an insulating layer under the cavity. Membrane displacement will result in a change in capacitance, which can be measured as a voltage change. Fig. 2.7 shows the cross section of a typical CMUT cell.

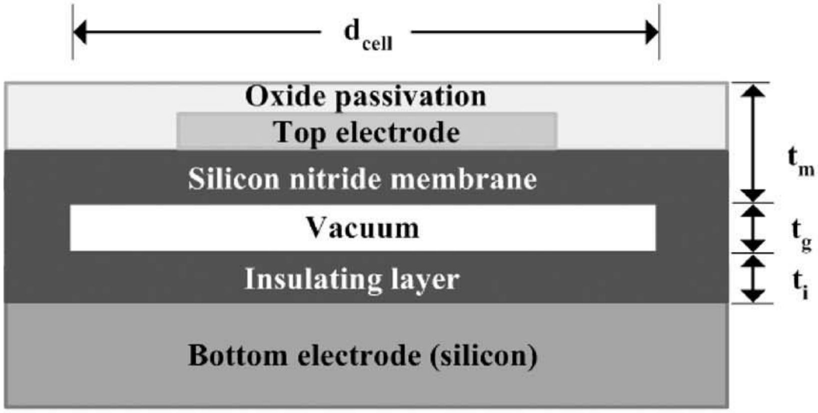

Figure 2.7. Cross section of a CMUT cell. Silicon nitride is used as the membrane, side walls, and insulating layer, but this can vary with design. The oxide passivation layer on top is an insulator and is optional for electrical safety. An example of typical CMUT dimensions are as follows: d_{cell} (cell diameter) = 36 µm, t_m (membrane thickness) = 0.9 µm, t_g (gap thickness) = 0.11 µm, and t_i (insulating layer thickness) = 0.2 µm [84]. © 2002 IEEE.

CMUTs require a bias voltage to operate. As shown in Fig. 2.8, as the bias voltage increases the slopes of the capacitance and membrane displacement graphs becomes steeper. This continues until the bias voltage is strong enough to snap the membrane down. For the most sensitive and efficient operation of a CMUT, a bias voltage must be applied to reach the steepest portion of the curve prior to snap down. At this point, a small change in displacement results in a large voltage signal which means higher sensitivity.

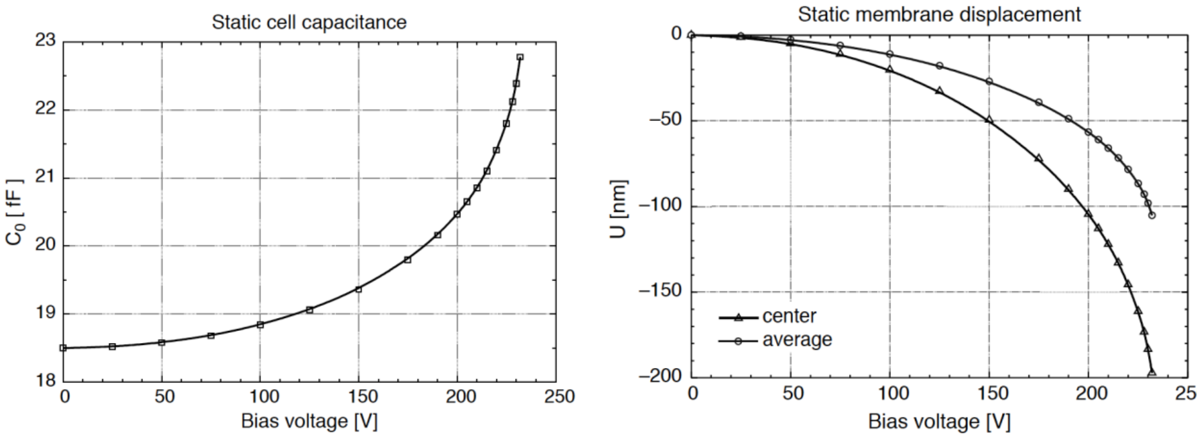

Figure 2.8. (Left) Capacitance vs. Bias Voltage and (Right) Membrane Displacement vs. Bias Voltage. As the bias voltage approaches the voltage required to snap the membrane down, the change in capacitance per change in voltage and the change in membrane displacement per change in voltage increase, which means higher sensitivity [90].

There are two main methods for CMUT fabrication: sacrificial-release and wafer-bonding. The sacrificial-release process was the first method used to fabricate CMUTs. The process flow can be seen in Fig. 2.9.

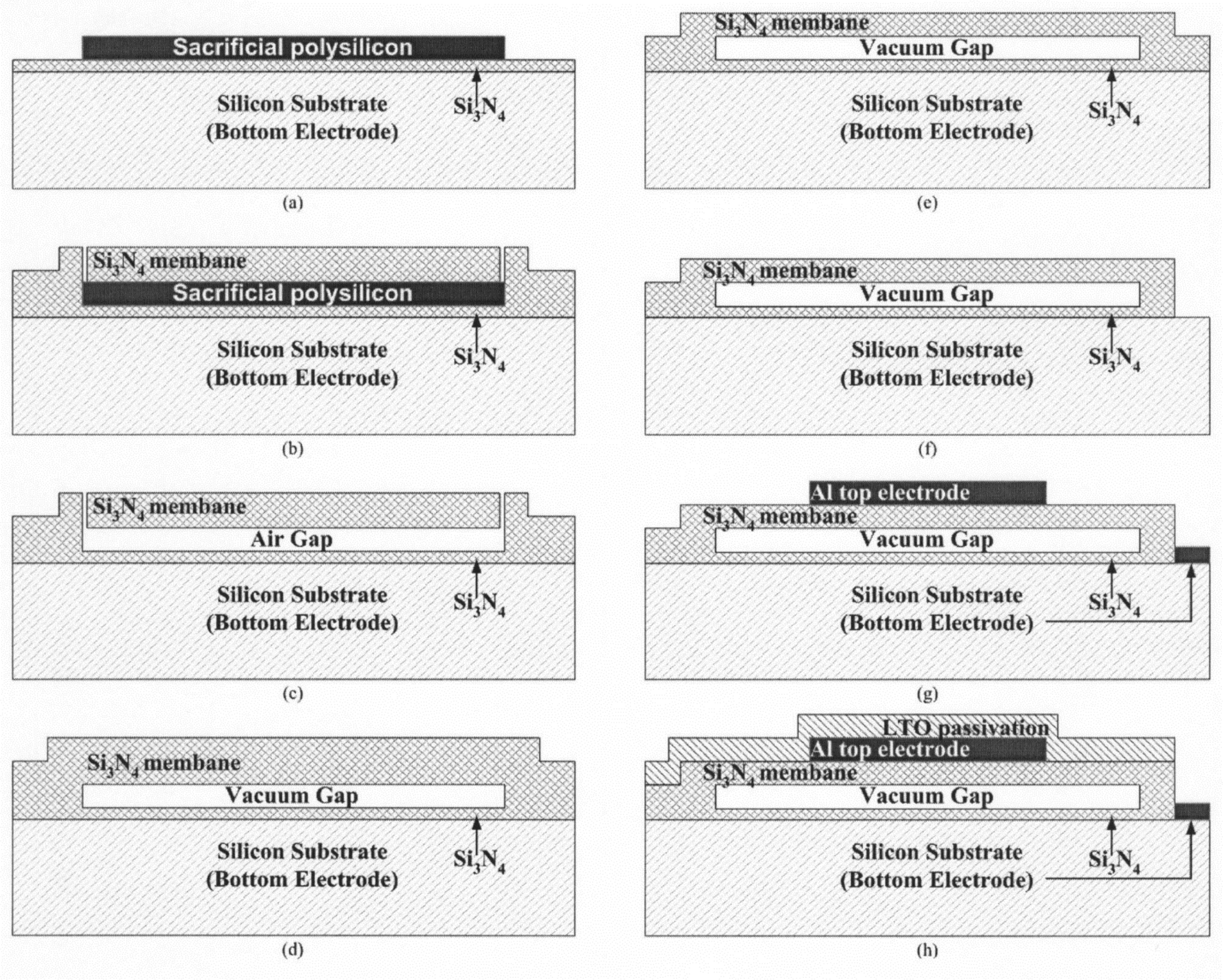

Figure 2.9. Process flow for sacrificial-release CMUT fabrication: (a) sacrificial layer is deposited on Si_3N_4, which sits on top of a heavily doped silicon substrate, (b) Si_3N_4 is deposited to form the membrane and etch holes are created, (c) the sacrificial layer is etched to release the membrane, (d) the etch holes are sealed with another layer of Si_3N_4. (e) [optional] the Si_3N_4 membrane can be etched back, (f) Si_3N_4 is etched to expose the bottom electrode, (g) aluminum is deposited and patterned to form electrical connections and bond pads, and (h) [optional] an electrically insulating LTO layer can be deposited to prevent shorting and corrosion. This figure is reused with permission from ASCE [92].

The sacrificial-release process begins with a highly doped silicon wafer that will act as the conductive bottom electrode. An insulating layer of silicon nitride (Si_3N_4) is deposited using low-pressure chemical vapour deposition (LPCVD). This layer acts as an etch stop for wet etching of the sacrificial layer and an insulating layer for when the top membrane snaps down. A sacrificial layer of polysilicon is then deposited using LPCVD and patterned using photolithography, Fig. 2.9 (a). The remaining polysilicon is known as the sacrificial layer and will later be etched to form the membrane gap. LPCVD is then used to deposit the silicon nitride that will form the sidewalls and membrane. The deposited Si_3N_4 film has a tensile stress of < 100 MPa. A low stress membrane is essential to prevent buckling and device failure once the sacrificial layer is etched away. Photolithography and dry etching are used to create small etch holes through the silicon nitride to reach the sacrificial layer, Fig. 2.9 (b). The wafers are then immersed in potassium hydroxide (KOH) to etch the sacrificial layer through the small etch holes. Fig. 2.9 (c). LPCVD is then used to deposit another layer of Si_3N_4 that will seal the etch holes at low pressure to prevent fluids from leaking in through the etch holes when immersed, Fig. 2.9 (d). If necessary, the Si_3N_4 membrane layer can be etched back to reduce thickness, Fig. 2.9 (e). This step is not necessary and is often difficult to perform without etch stops, which is why many CMUT fabricators choose to skip this step. Now that the CMUT structure has been created, the final few steps are to develop metal contacts for operating the CMUT. Lithography and etching are used to etch away part of the Si_3N_4 to gain access to the bottom electrode, Fig. 2.9 (f). Aluminum is then sputtered, patterned, and wet etched to form the top and bottom metal contacts, Fig. 2.9 (g). The final optional step is to deposit an electrical insulating low temperature oxide (LTO) layer to prevent shorting in conductive fluids and corrosion, Fig. 2.9 (h).

The wafer bonding technique allows for faster CMUT processing speeds at the cost of more expensive silicon-on-insulator (SOI) wafers [89]. The wafer-bonding process flow can be seen in Fig. 2.10.

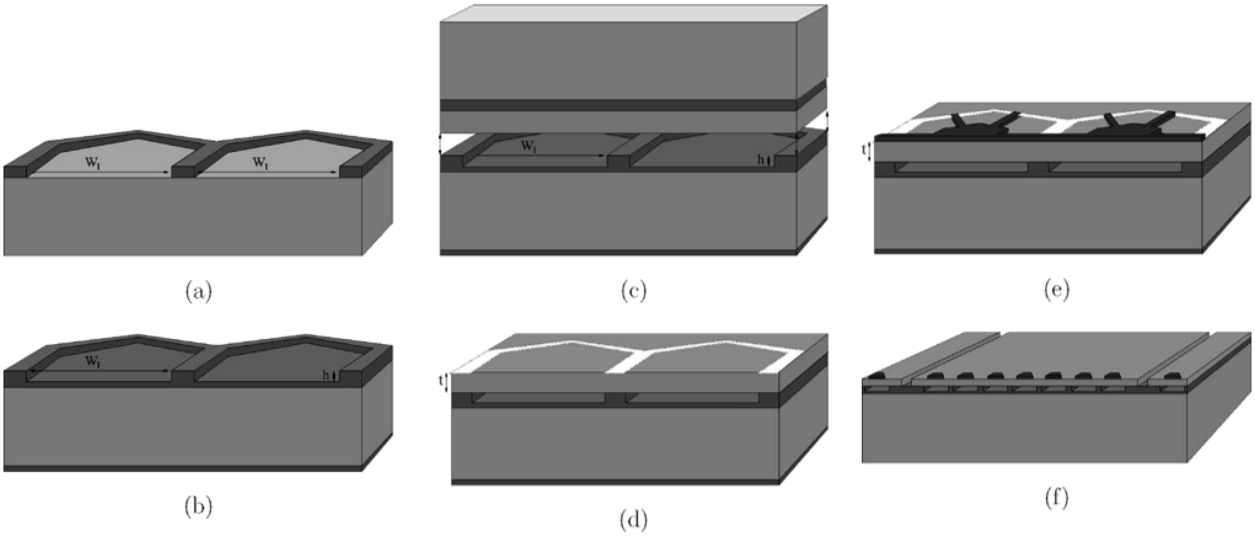

Figure 2.10. Process flow for wafer-bonded CMUT fabrication: (a) a thermal oxide is grown and patterned on a doped silicon wafer, (b) another thermal oxide is grown for electrical insulation from the top membrane, (c) an SOI wafer is bonded to the previous wafer with the device highly doped silicon layer facing the thermally grown oxide, (d) the handle and buried oxide are etched and an opening to the bottom electrode is made, (e) metal contacts and bond pads are created using aluminum sputtering and patterning, and (f) the devices are electrically isolated with trenches [93]. © 2005 IEEE.

A highly doped silicon wafer is used for the bottom electrode. The wafer is thermally oxidized and patterned with photolithography to produce the cavity dimensions. The unmasked silicon dioxide is then etched down to the silicon using hydrofluoric acid, Fig. 2.10 (a). This forms the cavity with the silicon dioxide thickness dictating the CMUT gap height. A second thermal oxidation is performed after removing the photoresist, Fig. 2.10 (b). This oxide layer is used to prevent shorting when the membrane snaps down. This first wafer is then bonded under vacuum with a highly doped SOI wafer on top and annealed, Fig. 2.10 (c). The thick silicon layer of the SOI wafer can be removed with a wet etch using KOH. The buried silicon dioxide in the SOI wafer will act as an etch stop. Once the buried silicon dioxide is exposed, it can be removed using hydrofluoric acid, Fig. 2.10 (d). The silicon membrane will act as an etch stop for the hydrofluoric acid. Holes reaching the bottom electrode must be created using photolithography and etching. To form the metal contacts and bond pads, aluminum is first sputtered on the wafer. Photolithography and wet etching are then performed to define the metal contacts and bond pads, Fig. 2.10 (e). Finally, trenches can be created using photolithography and dry etching to electrically isolate the elements, Fig. 2.10 (f).

2.3.2.2.1 2D Arrays for 3D Photoacoustic Imaging

Linear arrays provide 2D B-scan imaging. To provide 3D PA imaging capabilities, investigators have used mechanically scanned linear array transducers. 2D transducer arrays provide the opportunity of 3D imaging without mechanical scanning. However, fully wired 2D arrays are not widely commercially available and are impractical for large array sizes. Fully wired 2D arrays have large transmit-receive channels numbers that adds significant design complexity. Integrated beamforming electronics are often implemented to reduce channel numbers at the expense of increased cost and decreased imaging speed. Alternatives to piezoelectric 2D arrays include optically interrogated Fabry-Perot etalons, which will be discussed later. However, this approach requires slow scanning of an interrogation beam. To address challenges of addressing large 2D arrays, various groups have considered sparse readout schemes [94]. These approaches use element pitches much larger than the device center frequency wavelength, which results in poor image quality.

2.3.2.2.2 Top-Orthogonal-to-Bottom-Electrode CMUTs

To address the difficulties of reading out signals from large 2D arrays, some groups have proposed crossed electrode transducer architectures. These involve top row electrode strips orthogonal to bottom column electrodes strips. A significant amount of research has been done on this architecture under the name row-column addressing or cross electrode arrays [95-99]. Cross electrode arrays were originally developed using piezoelectric materials for pulse-echo ultrasound 3D imaging. They operated by transmit focusing in the elevational direction and receive focusing in the azimuthal direction. However, these arrays were incapable of reading out from each element of the 2D array as would be required for PA imaging.

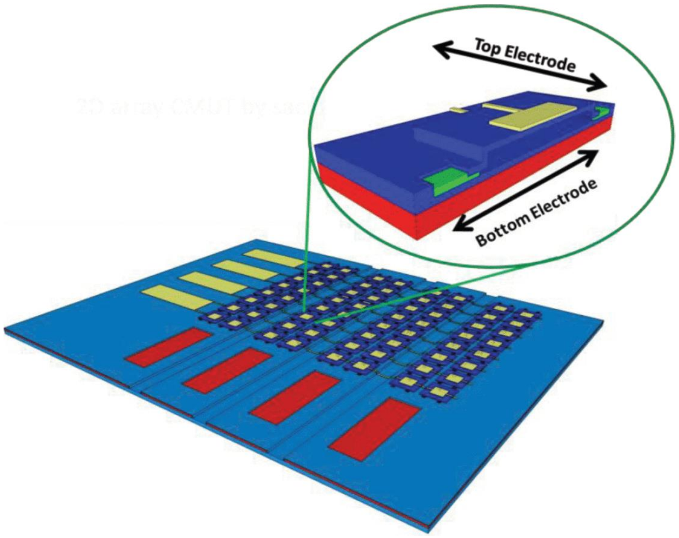

Figure 2.11. Illustration of a TOBE CMUT array. Bottom electrodes are orthogonal to top electrodes [91]. © 2014 IEEE.

The Zemp lab has previously worked on these crossed electrode architectures with CMUTs and referred to them as TOBE CMUTs. The Zemp lab was the first to demonstrate single element control and readout from this architecture. Fig. 2.11 illustrates a TOBE CMUT array with orthogonal top and bottom electrodes. TOBE CMUTs can reduce channel requirements by reading out activated column elements from the rows. The elements in a column are activated when a bias is applied to the column. The signals from these activated elements can be read out from their respective rows. Thus, an array of N rows and N columns only requires N channels instead N^2 channels.

In this thesis, we will expand upon TOBE CMUTs for use in 3D PA imaging. We will also propose a technique for fast 3D PA imaging with TOBE CMUTs called modulation encoding. There has been a significant amount of ongoing research on TOBE CMUTs. This includes research into integrated apodization [100, 101], acoustic crosstalk [102], non-destructive testing [103], increasing field-of-view [104], flow estimation [105, 106], fabrication [107], and probe development [108]. The Zemp lab has also continued to develop these devices including proposing a new electronic scanning scheme [109] and simulation model [110].

2.3.2.2.3 Interlaced Multifrequency CMUTs

An additional architecture afforded by CMUT fabrication ease is the interlaced multifrequency design discussed in chapter 5. Multifrequency transducers are necessary because a large bandwidth is required to detect both large, diffuse molecular contrast agent distributions and fine structures simultaneously. Previous to this contribution, other group have attempted to fabricate piezoelectric multifrequency transducers with various challenges further described in chapter 5.

2.3.2.3 Other Types of Ultrasound Transducers

Fabry-Perot ultrasound transducers are based on optical interferometry and the acousto-optic effect. A Fabry-Perot sensor consists of an etalon layer, which has two parallel, optically reflective surfaces. The etalon layer remains in contact with the imaging target and is interrogated by a broad bandwidth laser and reflects off both surfaces for interferometry. When PA signals interact with the etalon, it changes the optical properties of the etalon, which is known as the acousto-optic effect. This changes the constructive and destructive interference of the reflected interrogation beams, which can be used to determine the PA signal intensity. Fabry-Perot transducers are advantageous because they can be made transparent to light in the PA imaging range, so there is no transducer obstruction in light delivery [111, 112]. They also have the advantage of having relatively higher sensitivity and broader bandwidth than typical broadband transducers [111, 112]. There has been significant recent work on using Fabry-Perot transducers in PA imaging [113-116]. Fig. 2.4 (g) shows a PAM setup using a Fabry-Perot transducer.

pMUTs are another alternative transducer that consists of a single piezoelectric layer on a silicon background [117]. pMUTs attempt to take advantage of the advances in micromachining used by CMUTs and apply it to peizoelectrics [118]. pMUTs tend to have improved transmits pressures in comparison to CMUTs. pMUTS have also been used for PA imaging [119, 120].

Finally, relaxor arrays are a very promising new ultrasound transducer that consists of crossed electrodes and bias sensitive piezoelectric material [121]. The crossed electrode design is similar to that of the TOBE CMUT. Current work is being done to apply relaxor arrays to PA imaging.

2.3.3 Real-Time 3D Photoacoustic Molecular Imaging Transducers

3D PA molecular imaging requires large 2D arrays for large fields-of-view and fast imaging speeds in order to image molecular interactions in real-time. These large arrays must also have high bandwidth to image both fine structures and large, diffuse molecular contrast agent distributions. Very large 2D arrays are a problem for ultrasound transducers because of the complexity and cost of having many transmit-receive channels [123, 124]. It is for this reason that clinical transducer are typically limited to 1024 (32 by 32 elements) transmit-receive channels or less. Approaches like sparse 2D arrays have been proposed as a solution [123], but this approach sacrifices resolution and sensitivity. Integrated beamforming electronics are often implemented to reduce the channel numbers but do so at the expense of imaging speed. Finally, a large bandwidth is required to image molecular PA interactions. This is because fine structures produce high-frequency PA signals, but larger diffuse targets, like contrast agent concentrations, will produce low-frequency PA signals, typically undetectable by high-frequency clinical transducers. Broadband Fabry-Perot transducers may have excellent bandwidth, but they require scanning to produce 3D images and thus would not be able to image in real-time.

References

1. R. Weissleder, "Molecular imaging in cancer," Science **312,** 1168-1171 (2006).

2. T. F. Massoud and S. S. Gambhir, "Molecular imaging in living subjects: seeing fundamental biological processes in a new light," Genes Dev. **17,** 545-580 (2003).

3. S. S. Gambhir, "Molecular imaging of cancer with positron emission tomography," Nature Reviews Cancer **2,** 683 (2002).

4. W. Cai and X. Chen, "Multimodality molecular imaging of tumor angiogenesis," J. Nucl. Med. **49 Suppl 2,** 113S-28S (2008).

5. T. Hussain and Q. T. Nguyen, "Molecular imaging for cancer diagnosis and surgery," Adv. Drug Deliv. Rev. **66,** 90-100 (2014).

6. J. Sorensen, D. Sandberg, M. Sandstrom, A. Wennborg, J. Feldwisch, V. Tolmachev, G. Astrom, M. Lubberink, U. Garske-Roman, J. Carlsson, and H. Lindman, "First-in-human molecular imaging of HER2 expression in breast cancer metastases using the 111In-ABY-025 affibody molecule," J. Nucl. Med. **55,** 730-735 (2014).

7. M. Rudin and R. Weissleder, "Molecular imaging in drug discovery and development," Nature reviews Drug discovery **2,** 123 (2003).

8. J. K. Willmann, N. Van Bruggen, L. M. Dinkelborg, and S. S. Gambhir, "Molecular imaging in drug development," Nature reviews Drug discovery **7,** 591 (2008).

9. C. M. Gomes, A. J. Abrunhosa, P. Ramos, and E. K. Pauwels, "Molecular imaging with SPECT as a tool for drug development," Adv. Drug Deliv. Rev. **63,** 547-554 (2011).

10. L. Cunha, K. Szigeti, D. Mathé, and L. F. Metello, "The role of molecular imaging in modern drug development," Drug Discov. Today **19,** 936-948 (2014).

11. I. J. Hildebrandt and S. S. Gambhir, "Molecular imaging applications for immunology," Clinical immunology **111,** 210-224 (2004).

12. H. W. Lee, P. Gangadaran, S. Kalimuthu, and B. Ahn, "Advances in molecular imaging strategies for in vivo tracking of immune cells," BioMed research international **2016,** (2016).

13. M. L. James and S. S. Gambhir, "A molecular imaging primer: modalities, imaging agents, and applications," Physiol. Rev. **92,** 897-965 (2012).

14. D. Erritzoe, K. Holst, V. G. Frokjaer, C. L. Licht, J. Kalbitzer, F. A. Nielsen, C. Svarer, J. Madsen, and G. Knudsen, "A nonlinear relationship between cerebral serotonin transporter and 5-HT(2A) receptor binding: an in vivo molecular imaging study in humans," J. Neurosci. **30,** 3391-3397 (2010).

15. A. Egerton, M. A. Mehta, A. J. Montgomery, J. M. Lappin, O. D. Howes, S. J. Reeves, V. J. Cunningham, and P. M. Grasby, "The dopaminergic basis of human behaviors: a review of molecular imaging studies," Neuroscience & Biobehavioral Reviews **33,** 1109-1132 (2009).

16. L. W. Dobrucki and A. J. Sinusas, "PET and SPECT in cardiovascular molecular imaging," Nature Reviews Cardiology **7,** 38 (2010).

17. A. Saraste, S. G. Nekolla, and M. Schwaiger, "Cardiovascular molecular imaging: an overview," Cardiovasc. Res. **83,** 643-652 (2009).

18. I. Y. Chen and J. C. Wu, "Cardiovascular molecular imaging: focus on clinical translation," Circulation **123,** 425-443 (2011).

19. R. P. Baum and H. R. Kulkarni, "THERANOSTICS: From Molecular Imaging Using Ga-68 Labeled Tracers and PET/CT to Personalized Radionuclide Therapy - The Bad Berka Experience," Theranostics **2,** 437-447 (2012).

20. M. A. Pysz, S. S. Gambhir, and J. K. Willmann, "Molecular imaging: current status and emerging strategies," Clin. Radiol. **65,** 500-516 (2010).

21. L. V. Wang and H. Wu, *Biomedical optics: principles and imaging* (John Wiley & Sons, 2012).

22. J. Lee, Y. Huh, Y. Jun, J. Seo, J. Jang, H. Song, S. Kim, E. Cho, H. Yoon, and J. Suh, "Artificially engineered magnetic nanoparticles for ultra-sensitive molecular imaging," Nat. Med. **13,** 95 (2007).

23. Y. X. Wang, "Superparamagnetic iron oxide based MRI contrast agents: Current status of clinical application," Quant. Imaging Med. Surg. **1,** 35-40 (2011).

24. D. Artemov, "Molecular magnetic resonance imaging with targeted contrast agents," J. Cell. Biochem. **90,** 518-524 (2003).

25. P. Caravan, J. J. Ellison, T. J. McMurry, and R. B. Lauffer, "Gadolinium (III) chelates as MRI contrast agents: structure, dynamics, and applications," Chem. Rev. **99,** 2293-2352 (1999).

26. P. Caravan, "Protein-targeted gadolinium-based magnetic resonance imaging (MRI) contrast agents: design and mechanism of action," Acc. Chem. Res. **42,** 851-862 (2009).

27. R. Popovtzer, A. Agrawal, N. A. Kotov, A. Popovtzer, J. Balter, T. E. Carey, and R. Kopelman, "Targeted gold nanoparticles enable molecular CT imaging of cancer," Nano letters **8,** 4593-4596 (2008).

28. D. Pan, E. Roessl, J. Schlomka, S. D. Caruthers, A. Senpan, M. J. Scott, J. S. Allen, H. Zhang, G. Hu, and P. J. Gaffney, "Computed Tomography in Color: NanoK-Enhanced Spectral CT Molecular Imaging," Angewandte Chemie **122,** 9829-9833 (2010).

29. S. Chou, Y. Shau, P. Wu, Y. Yang, D. Shieh, and C. Chen, "In vitro and in vivo studies of FePt nanoparticles for dual modal CT/MRI molecular imaging," J. Am. Chem. Soc. **132,** 13270-13278 (2010).

30. C. S. Levin, "Primer on molecular imaging technology," European journal of nuclear medicine and molecular imaging **32,** S325-S345 (2005).

31. M. E. Phelps, "Positron emission tomography provides molecular imaging of biological processes," Proceedings of the National Academy of Sciences **97,** 9226-9233 (2000).

32. T. Knöpfel, J. Díez-García, and W. Akemann, "Optical probing of neuronal circuit dynamics: genetically encoded versus classical fluorescent sensors," Trends Neurosci. **29,** 160-166 (2006).

33. S. Gross and D. Piwnica-Worms, "Spying on cancer: molecular imaging in vivo with genetically encoded reporters," Cancer cell **7,** 5-15 (2005).

34. A. E. Palmer, Y. Qin, J. G. Park, and J. E. McCombs, "Design and application of genetically encoded biosensors," Trends Biotechnol. **29,** 144-152 (2011).

35. D. M. Chudakov, S. Lukyanov, and K. A. Lukyanov, "Fluorescent proteins as a toolkit for in vivo imaging," Trends Biotechnol. **23,** 605-613 (2005).

36. L. V. Wang and S. Hu, "Photoacoustic tomography: in vivo imaging from organelles to organs," Science **335,** 1458-1462 (2012).

37. J. Brunker, J. Yao, J. Laufer, and S. E. Bohndiek, "Photoacoustic imaging using genetically encoded reporters: a review," J. Biomed. Opt. **22,** 070901 (2017).

38. J. Kim, E. I. Galanzha, E. V. Shashkov, H. Moon, and V. P. Zharov, "Golden carbon nanotubes as multimodal photoacoustic and photothermal high-contrast molecular agents," Nature nanotechnology **4,** 688 (2009).

39. K. Pu, A. J. Shuhendler, J. V. Jokerst, J. Mei, S. S. Gambhir, Z. Bao, and J. Rao, "Semiconducting polymer nanoparticles as photoacoustic molecular imaging probes in living mice," Nature nanotechnology **9,** 233 (2014).

40. K. R. Zinn, T. R. Chaudhuri, A. A. Szafran, D. O'Quinn, C. Weaver, K. Dugger, D. Lamar, R. A. Kesterson, X. Wang, and S. J. Frank, "Noninvasive bioluminescence imaging in small animals," ILAR journal **49,** 103-115 (2008).

41. G. Themelis, J. S. Yoo, K. Soh, R. B. Schulz, and V. Ntziachristos, "Real-time intraoperative fluorescence imaging system using light-absorption correction," J. Biomed. Opt. **14,** 064012 (2009).

42. C. Li, G. S. Mitchell, J. Dutta, S. Ahn, R. M. Leahy, and S. R. Cherry, "A three-dimensional multispectral fluorescence optical tomography imaging system for small animals based on a conical mirror design," Optics express **17,** 7571-7585 (2009).

43. J. Gamelin, A. Maurudis, A. Aguirre, F. Huang, P. Guo, L. V. Wang, and Q. Zhu, "A real-time photoacoustic tomography system for small animals," Optics express **17,** 10489-10498 (2009).

44. D. Razansky, A. Buehler, and V. Ntziachristos, "Volumetric real-time multispectral optoacoustic tomography of biomarkers," Nature protocols **6,** 1121 (2011).

45. G. Balasundaram, C. J. Ho, K. Li, W. Driessen, U. S. Dinish, C. L. Wong, V. Ntziachristos, B. Liu, and M. Olivo, "Molecular photoacoustic imaging of breast cancer using an actively targeted conjugated polymer," Int. J. Nanomedicine **10,** 387-397 (2015).

46. M. Heijblom, D. Piras, W. Xia, J. C. van Hespen, J. Klaase, F. Van den Engh, T. Van Leeuwen, W. Steenbergen, and S. Manohar, "Visualizing breast cancer using the Twente photoacoustic mammoscope: what do we learn from twelve new patient measurements?" Optics express **20,** 11582-11597 (2012).

47. M. Heijblom, W. Steenbergen, and S. Manohar, "Clinical photoacoustic breast imaging: the twente experience." IEEE pulse **6,** 42-46 (2015).

48. R. A. Kruger, C. M. Kuzmiak, R. B. Lam, D. R. Reinecke, S. P. Del Rio, and D. Steed, "Dedicated 3D photoacoustic breast imaging," Med. Phys. **40,** (2013).

49. K. E. Wilson, S. V. Bachawal, L. Abou-Elkacem, K. Jensen, S. Machtaler, L. Tian, and J. K. Willmann, "Spectroscopic Photoacoustic Molecular Imaging of Breast Cancer using a B7-H3-targeted ICG Contrast Agent," Theranostics **7,** 1463 (2017).

50. K. Jansen, Van Der Steen, Antonius FW, H. M. van Beusekom, J. W. Oosterhuis, and G. van Soest, "Intravascular photoacoustic imaging of human coronary atherosclerosis," Opt. Lett. **36,** 597-599 (2011).

51. K. Jansen, M. Wu, van der Steen, Antonius FW, and G. van Soest, "Photoacoustic imaging of human coronary atherosclerosis in two spectral bands," Photoacoustics **2,** 12-20 (2014).

52. S. Sethuraman, J. H. Amirian, S. H. Litovsky, R. W. Smalling, and S. Y. Emelianov, "Spectroscopic intravascular photoacoustic imaging to differentiate atherosclerotic plaques," Optics express **16,** 3362-3367 (2008).

53. B. Wang, A. Karpiouk, D. Yeager, J. Amirian, S. Litovsky, R. Smalling, and S. Emelianov, "In vivo intravascular ultrasound-guided photoacoustic imaging of lipid in plaques using an animal model of atherosclerosis," Ultrasound Med. Biol. **38,** 2098-2103 (2012).

54. V. S. Dogra, B. K. Chinni, K. S. Valluru, J. V. Joseph, A. Ghazi, J. L. Yao, K. Evans, E. M. Messing, and N. A. Rao, "Multispectral Photoacoustic Imaging of Prostate Cancer: Preliminary Ex-vivo Results," J. Clin. Imaging Sci. **3,** 41-7514.119139. eCollection 2013 (2013).

55. X. Wang, W. W. Roberts, P. L. Carson, D. P. Wood, and J. B. Fowlkes, "Photoacoustic tomography: a potential new tool for prostate cancer," Biomedical optics express **1,** 1117-1126 (2010).

56. J. Xia, M. R. Chatni, K. I. Maslov, Z. Guo, K. Wang, M. A. Anastasio, and L. V. Wang, "Whole-body ring-shaped confocal photoacoustic computed tomography of small animals in vivo," J. Biomed. Opt. **17,** 050506 (2012).

57. J. Xia and L. V. Wang, "Small-animal whole-body photoacoustic tomography: a review," IEEE Transactions on Biomedical Engineering **61,** 1380-1389 (2014).

58. C. Kim, T. N. Erpelding, L. Jankovic, M. D. Pashley, and L. V. Wang, "Deeply penetrating in vivo photoacoustic imaging using a clinical ultrasound array system," Biomedical optics express **1,** 278-284 (2010).

59. K. Maslov, H. F. Zhang, S. Hu, and L. V. Wang, "Optical-resolution photoacoustic microscopy for in vivo imaging of single capillaries," Opt. Lett. **33,** 929-931 (2008).

60. S. Mallidi, G. P. Luke, and S. Emelianov, "Photoacoustic imaging in cancer detection, diagnosis, and treatment guidance," Trends Biotechnol. **29,** 213-221 (2011).

61. D. Razansky, C. Vinegoni, and V. Ntziachristos, "Multispectral photoacoustic imaging of fluorochromes in small animals," Opt. Lett. **32,** 2891-2893 (2007).

62. H. F. Zhang, K. Maslov, M. Sivaramakrishnan, G. Stoica, and L. V. Wang, "Imaging of hemoglobin oxygen saturation variations in single vessels in vivo using photoacoustic microscopy," Appl. Phys. Lett. **90,** 053901 (2007).

63. H. F. Zhang, K. Maslov, G. Stoica, and L. V. Wang, "Functional photoacoustic microscopy for high-resolution and noninvasive in vivo imaging," Nat. Biotechnol. **24,** 848 (2006).

64. S. Hu, K. Maslov, and L. V. Wang, "Second-generation optical-resolution photoacoustic microscopy with improved sensitivity and speed," Opt. Lett. **36,** 1134-1136 (2011).

65. L. V. Wang and J. Yao, "A practical guide to photoacoustic tomography in the life sciences," Nature methods **13,** 627 (2016).

66. J. Yao, A. A. Kaberniuk, L. Li, D. M. Shcherbakova, R. Zhang, L. Wang, G. Li, V. V. Verkhusha, and L. V. Wang, "Multiscale photoacoustic tomography using reversibly switchable bacterial phytochrome as a near-infrared photochromic probe," Nature methods **13,** 67-73 (2016).

67. M. Moothanchery and M. Pramanik, "Performance Characterization of a Switchable Acoustic Resolution and Optical Resolution Photoacoustic Microscopy System," Sensors **17,** 357 (2017).

68. L. V. Wang, "Tutorial on photoacoustic microscopy and computed tomography," IEEE Journal of Selected Topics in Quantum Electronics **14,** 171-179 (2008).

69. H. Brecht, R. Su, M. Fronheiser, S. A. Ermilov, A. Conjusteau, and A. A. Oraevsky, "Whole-body three-dimensional optoacoustic tomography system for small animals," J. Biomed. Opt. **14,** 064007-064007-8 (2009).

70. G. Ku and L. V. Wang, "Deeply penetrating photoacoustic tomography in biological tissues enhanced with an optical contrast agent," Opt. Lett. **30,** 507-509 (2005).

71. S. Zhang, R. Cheng, C. Tao, and X. Liu, "Photoacoustic tomography with a high lateral resolution and a large field of view using a rectangular focused ultrasound transducer," Applied Physics Express **9,** 047301 (2016).

72. M. Xu and L. V. Wang, "Universal back-projection algorithm for photoacoustic computed tomography," Physical Review E **71,** 016706 (2005).

73. Y. Xu and L. V. Wang, "Time reversal and its application to tomography with diffracting sources," Phys. Rev. Lett. **92,** 033902 (2004).

74. A. Rosenthal, D. Razansky, and V. Ntziachristos, "Fast semi-analytical model-based acoustic inversion for quantitative optoacoustic tomography," IEEE Trans. Med. Imaging **29,** 1275-1285 (2010).

75. B. Cox and P. Beard, "Fast calculation of pulsed photoacoustic fields in fluids using k-space methods," J. Acoust. Soc. Am. **117,** 3616-3627 (2005).

76. A. Rosenthal, V. Ntziachristos, and D. Razansky, "Model-based optoacoustic inversion with arbitrary-shape detectors," Med. Phys. **38,** 4285-4295 (2011).

77. K. P. Köstli, M. Frenz, H. Bebie, and H. P. Weber, "Temporal backward projection of optoacoustic pressure transients using Fourier transform methods," Physics in Medicine & Biology **46,** 1863 (2001).

78. K. P. Köstli and P. C. Beard, "Two-dimensional photoacoustic imaging by use of Fourier-transform image reconstruction and a detector with an anisotropic response," Appl. Opt. **42,** 1899-1908 (2003).

79. Y. Li, A. Forbrich, J. Wu, P. Shao, R. E. Campbell, and R. Zemp, "Engineering dark chromoprotein reporters for photoacoustic microscopy and FRET imaging," Scientific reports **6,** 22129 (2016).

80. R. S. Cobbold, *Foundations of biomedical ultrasound* (Oxford University Press, 2006).

81. S. Katzir, "The discovery of the piezoelectric effect," Archive for history of exact sciences **57,** 61-91 (2003).

82. W. P. Mason, "Piezoelectricity, its history and applications," J. Acoust. Soc. Am. **70,** 1561-1566 (1981).

83. T. L. Szabo, *Diagnostic ultrasound imaging: inside out* (Academic Press, 2004).

84. O. Oralkan, A. S. Ergun, J. A. Johnson, M. Karaman, U. Demirci, K. Kaviani, T. H. Lee, and B. T. Khuri-Yakub, "Capacitive micromachined ultrasonic transducers: Next-generation arrays for acoustic imaging?" IEEE Trans. Ultrason. Ferroelectr. Freq. Control **49,** 1596-1610 (2002).

85. M. I. Haller and B. T. Khuri-Yakub, "A surface micromachined electrostatic ultrasonic air transducer," IEEE Trans. Ultrason. Ferroelectr. Freq. Control **43,** 1-6 (1996).

86. X. Jin, I. Ladabaum, and B. T. Khuri-Yakub, "The microfabrication of capacitive ultrasonic transducers," J Microelectromech Syst **7,** 295-302 (1998).

87. X. Jin, I. Ladabaum, F. L. Degertekin, S. Calmes, and B. T. Khuri-Yakub, "Fabrication and characterization of surface micromachined capacitive ultrasonic immersion transducers," J Microelectromech Syst **8,** 100-114 (1999).

88. I. Ladabaum, X. Jin, H. T. Soh, A. Atalar, and B. Khuri-Yakub, "Surface micromachined capacitive ultrasonic transducers," IEEE Trans. Ultrason. Ferroelectr. Freq. Control **45,** 678-690 (1998).

89. Y. Huang, A. S. Ergun, E. Haeggstrom, M. H. Badi, and B. T. Khuri-Yakub, "Fabricating capacitive micromachined ultrasonic transducers with wafer-bonding technology," J Microelectromech Syst **12,** 128-137 (2003).

90. A. Caronti, G. Caliano, R. Carotenuto, A. Savoia, M. Pappalardo, E. Cianci, and V. Foglietti, "Capacitive micromachined ultrasonic transducer (CMUT) arrays for medical imaging," Microelectron. J. **37,** 770-777 (2006).

91. A. Sampaleanu, P. Zhang, A. Kshirsagar, W. Moussa, and R. Zemp, "Top-orthogonal-to-bottom-electrode (TOBE) CMUT arrays for 3-D ultrasound imaging," IEEE Trans. Ultrason. Ferroelectr. Freq. Control **61,** 266-276 (2014).

92. A. S. Ergun, G. G. Yaralioglu, and B. T. Khuri-Yakub, "Capacitive micromachined ultrasonic transducers: Theory and technology," J. Aerospace Eng. **16,** 76-84 (2003).

93. A. Erguri, Y. Huang, X. Zhuang, O. Oralkan, G. G. Yarahoglu, and B. T. Khuri-Yakub, "Capacitive micromachined ultrasonic transducers: Fabrication technology," IEEE Trans. Ultrason. Ferroelectr. Freq. Control **52,** 2242-2258 (2005).

94. P. Ephrat, L. Keenlislide, A. Seabrook, F. S. Prato, and J. J. Carson, "Three-dimensional photoacoustic imaging by sparse-array detection and iterative image reconstruction," J. Biomed. Opt. **13,** 054052 (2008).

95. C. E. Morton and G. R. Lockwood, "Theoretical assessment of a crossed electrode 2-D array for 3-D imaging," in *Ultrasonics, 2003 IEEE Symposium on,* Anonymous (IEEE, 2003), pp. 968-971.

96. N. M. Daher and J. T. Yen, "2-D array for 3-D ultrasound imaging using synthetic aperture techniques," IEEE Trans. Ultrason. Ferroelectr. Freq. Control **53,** 912-924 (2006).

97. C. H. Seo and J. T. Yen, "A 256 x 256 2-D array transducer with row-column addressing for 3-D rectilinear imaging," IEEE Trans. Ultrason. Ferroelectr. Freq. Control **56,** (2009).

98. C. E. Demore, A. W. Joyce, K. Wall, and G. R. Lockwood, "Real-time volume imaging using a crossed electrode array," IEEE Trans. Ultrason. Ferroelectr. Freq. Control **56,** 1252-1261 (2009).

99. A. S. Logan, L. L. Wong, A. I. Chen, and J. T. Yeow, "A 32 x 32 element row-column addressed capacitive micromachined ultrasonic transducer," IEEE Trans. Ultrason. Ferroelectr. Freq. Control **58,** 1266-1271 (2011).

100. M. F. Rasmussen, T. L. Christiansen, E. V. Thomsen, and J. A. Jensen, "3-D imaging using row-column-addressed arrays with integrated apodization-part i: apodization design and line element beamforming," IEEE Trans. Ultrason. Ferroelectr. Freq. Control **62,** 947-958 (2015).

101. T. L. Christiansen, M. F. Rasmussen, J. P. Bagge, L. N. Moesner, J. A. Jensen, and E. V. Thomsen, "3-D imaging using row–column-addressed arrays with integrated apodization—part II: Transducer fabrication and experimental results," IEEE Trans. Ultrason. Ferroelectr. Freq. Control **62,** 959-971 (2015).

102. T. L. Christiansen, J. A. Jensen, and E. V. Thomsen, "Acoustical cross-talk in row–column addressed 2-D transducer arrays for ultrasound imaging," Ultrasonics **63,** 174-178 (2015).

103. L. L. Wong, A. I. Chen, Z. Li, A. S. Logan, and J. T. Yeow, "A row–column addressed micromachined ultrasonic transducer array for surface scanning applications," Ultrasonics **54,** 2072-2080 (2014).

104. H. Bouzari, M. Engholm, C. Beers, M. B. Stuart, S. I. Nikolov, E. V. Thomsen, and J. A. Jensen, "Curvilinear 3-D Imaging Using Row-Column-Addressed 2-D Arrays With a Diverging Lens: Feasibility Study," IEEE Trans. Ultrason. Ferroelectr. Freq. Control **64,** 978-988 (2017).

105. S. Holbek, T. L. Christiansen, M. B. Stuart, C. Beers, E. V. Thomsen, and J. A. Jensen, "3-D Vector Flow Estimation With Row–Column-Addressed Arrays," IEEE Trans. Ultrason. Ferroelectr. Freq. Control **63,** 1799-1814 (2016).

106. S. Holbek, C. Ewertsen, H. Bouzari, M. J. Pihl, K. L. Hansen, M. B. Stuart, C. Thomsen, M. B. Nielsen, and J. A. Jensen, "Ultrasonic 3-D vector flow method for quantitative in vivo peak velocity and flow rate estimation," IEEE Trans. Ultrason. Ferroelectr. Freq. Control **64,** 544-554 (2017).

107. B. A. Greenlay and R. J. Zemp, "Fabrication of linear array and top-orthogonal-to-bottom electrode cmut arrays with a sacrificial release process," IEEE Trans. Ultrason. Ferroelectr. Freq. Control **64,** 93-107 (2017).

108. M. Engholm, H. Bouzari, T. L. Christiansen, C. Beers, J. P. Bagge, L. N. Moesner, S. E. Diederichsen, M. B. Stuart, J. A. Jensen, and E. V. Thomsen, "Probe development of CMUT and PZT row–column-addressed 2-D arrays," Sensors and Actuators A: Physical **273,** 121-133 (2018).

109. C. Ceroici, T. Harrison, and R. J. Zemp, "Fast Orthogonal Row–Column Electronic Scanning With Top-Orthogonal-to-Bottom Electrode Arrays," IEEE Trans. Ultrason. Ferroelectr. Freq. Control **64,** 1009-1014 (2017).

110. C. Ceroici and R. J. Zemp, "Large-Scale Nonlinear Lumped and Integrated Field Simulations of Top-Orthogonal-to-Bottom-Electrode CMUT Architectures," IEEE Trans. Ultrason. Ferroelectr. Freq. Control **64,** 1087-1091 (2017).

111. E. Zhang, J. Laufer, R. Pedley, and P. Beard, "In vivo high-resolution 3D photoacoustic imaging of superficial vascular anatomy," Physics in Medicine & Biology **54,** 1035 (2009).

112. E. Zhang, J. Laufer, and P. Beard, "Backward-mode multiwavelength photoacoustic scanner using a planar Fabry-Perot polymer film ultrasound sensor for high-resolution three-dimensional imaging of biological tissues," Appl. Opt. **47,** 561-577 (2008).

113. J. Buchmann, J. Guggenheim, E. Zhang, C. Scharfenorth, B. Spannekrebs, C. Villringer, and J. Laufer, "Characterization and modeling of Fabry–Perot ultrasound sensors with hard dielectric mirrors for photoacoustic imaging," Appl. Opt. **56,** 5039-5046 (2017).

114. P. Hajireza, J. Sorge, M. Brett, and R. Zemp, "In vivo optical resolution photoacoustic microscopy using glancing angle-deposited nanostructured Fabry–Perot etalons," Opt. Lett. **40,** 1350-1353 (2015).

115. N. Huynh, F. Lucka, E. Zhang, M. Betcke, S. Arridge, P. Beard, and B. Cox, "Sub-sampled Fabry-Perot photoacoustic scanner for fast 3D imaging," in *Photons Plus Ultrasound: Imaging and Sensing 2017,* Anonymous (International Society for Optics and Photonics, 2017), pp. 100641Y.

116. A. A. Plumb, N. T. Huynh, J. Guggenheim, E. Zhang, and P. Beard, "Rapid volumetric photoacoustic tomographic imaging with a Fabry-Perot ultrasound sensor depicts peripheral arteries and microvascular vasomotor responses to thermal stimuli," Eur. Radiol.1-9 (2017).

117. J. Vernet, W. Steichen, R. Lardat, O. Garcia, and J. Gelly, "PMUTS design optimization for medical probes applications," in *Ultrasonics Symposium, 2001 IEEE,* Anonymous (IEEE, 2001), pp. 899-902.

118. D. Akai, T. Yogi, I. Kamja, Y. Numata, K. Ozaki, K. Sawada, N. Okada, K. Higuchi, and M. Ishida, "Miniature ultrasound acoustic imaging devices using 2-D pMUTs array on epitaxial PZT/SrRuO 3/Pt/^{3}-Al 2 O 3/Si structure," in *Solid-State Sensors, Actuators and Microsystems Conference (TRANSDUCERS), 2011 16th International,* Anonymous (IEEE, 2011), pp. 910-913.

119. B. Chen, F. Chu, X. Liu, Y. Li, J. Rong, and H. Jiang, "AlN-based piezoelectric micromachined ultrasonic transducer for photoacoustic imaging," Appl. Phys. Lett. **103,** 031118 (2013).

120. W. Liao, W. Liu, J. Rogers, F. Usmani, Y. Tang, B. Wang, H. Jiang, and H. Xie, "Piezeoelectric micromachined ultrasound tranducer array for photoacoustic imaging," in *Solid-State Sensors, Actuators and Microsystems (TRANSDUCERS & EUROSENSORS XXVII), 2013 Transducers & Eurosensors XXVII: The 17th International Conference on,* Anonymous (IEEE, 2013), pp. 1831-1834.

121. K. Latham, C. Samson, C. Ceroici, R. J. Zemp, and J. A. Brown, "Fabrication and performance of a 128-element crossed-electrode relaxor array, for a novel 3D imaging approach," in *Ultrasonics Symposium (IUS), 2017 IEEE International,* Anonymous (IEEE, 2017), pp. 1-4.

122. A. Austeng and S. Holm, "Sparse 2-D arrays for 3-D phased array imaging-design methods," IEEE Trans. Ultrason. Ferroelectr. Freq. Control **49,** 1073-1086 (2002).

123. S. W. Smith, R. E. Davidsen, C. D. Emery, R. L. Goldberg, and E. D. Light, "Update on 2-D array transducers for medical ultrasound," in *Ultrasonics Symposium, 1995. Proceedings., 1995 IEEE,* Anonymous (IEEE, 1995), pp. 1273-1278.

3. Top Orthogonal to Bottom Electrode (TOBE) 2D CMUT Arrays for 3D Photoacoustic Imaging

Photoacoustic imaging is a relatively new imaging technique that involves detection and reconstruction of laser-induced ultrasonic signals. Unlike ultrasound imaging, photoacoustic imaging provides optical absorption contrast. Photoacoustic imaging originally required mechanically scanning a single-element transducer over an area, but this is time consuming. Linear transducers were proposed to improve imaging times and have greatly improved the frame rate for B-scan imaging, but mechanical scanning and many laser pulses are still required to obtain a 3D image. Elevational focusing is typically fixed via a physical acoustic lens on linear arrays so resolution away from this fixed focus may be compromised compared to a fully-wired 2D array. 2D arrays would enable 3D images without mechanical scanning. While this has been done with traditional piezoelectric transducers, capacitive micromachined ultrasound transducers (CMUTs) offer numerous advantages including ease of fabrication, broad bandwidth, and high sensitivity. Volumetric ultrasound images have previously been obtained using 2D CMUT arrays [1, 2]. However, large fully-wired 2D arrays may be unfeasible due to extensive channel requirements and complex wiring. Considerable research has been done to address this problem. Forward-facing ring arrays [3] and sparse arrays [4] are some of the architectures that have previously been proposed to address such problems.

Top orthogonal to bottom electrode (TOBE) CMUTs are a new transducer architecture that has recently been proposed to facilitate simple addressing of a 2D CMUT array [5]. In this architecture, the top and bottom electrodes are routed in N orthogonal rows and columns, creating an N×N array. For an N×N array, we previously demonstrated that only N bias channels and N transmit-receive channels are required to address each element of the array, which reduces the number of channels required by a factor of N compared to a fully-wired array. A group of CMUT membranes forming an element are located at each row-column intersection. A similar architecture has been studied before using piezoelectric crossed electrode arrays [6, 7] and CMUT row-column arrays [8, 9]. However, single element actuation was not demonstrated in these architectures. As a result, dynamic receive beamforming was only possible in one direction, while the orthogonal direction was limited to fixed-depth one-way transmit focusing, hence resulting in considerable loss in ultrasound image quality compared to a fully-wired array. Moreover, crossed electrode arrays are limited to one-directional receive focusing, excluding 3D photoacoustic imaging applications. TOBE CMUTs are capable of dominant single element actuation by biasing a column and transmitting a signal on a row. Similarly, single element receive sensitivity is also possible by biasing a column and reading the signal out from a row. Dominant element transmit and receive sensitivity is possible because biased elements exhibit smaller gaps and sensitivity scales as the reciprocal of the gap squared. During dominant single element reception, parasitic capacitance from unused elements can reduce overall sensitivity, however ~100 $mPa/\sqrt{Hz}$ sensitivity was still achievable [5]. TOBE CMUTs have numerous applications for fast 3D medical imaging, but experimental 3D images have yet to be obtained.

In this chapter, the feasibility of 3D photoacoustic imaging using TOBE CMUTs is demonstrated for the first time. Since TOBE CMUTs can read an entire column of data at once, only N laser pulses and N channels are necessary for an N×N TOBE array. Biasing one column at a time effectively selects a linear array which is scanned by switching the bias voltage to a different column as shown in Fig. 3.1. We chose to mechanically scan a small TOBE array with a biased signal column to simply demonstrate that high resolution images can be obtained with TOBE CMUTs. The full functionality of TOBE CMUTs has been verified in [5]. We use a hair phantom in oil immersion as a target. The received data is then dynamically beamformed to obtain high resolution images. This represents the first attempt at applying TOBE CMUTs to imaging applications and photoacoustics.

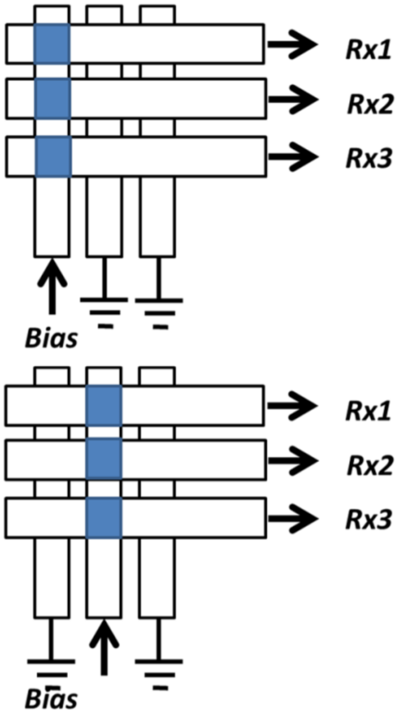

Figure 3.1. Column-by-column readout scheme.

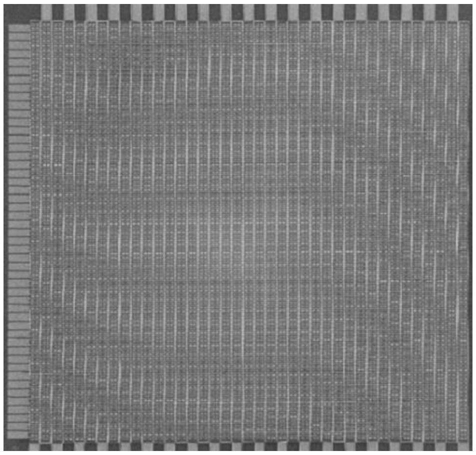

Figure 3.2. SEM image of fabricated TOBE CMUT array.

The fabrication of TOBE CMUTs is described in detail in a previous paper [5]. TOBE CMUTs are fabricated using a modified sacrificial release method on a patterned SOI wafer. The process is similar to that described in [10]. Key differences include the use of an SOI wafer with patterned device layer as the bottom electrode. Individually addressable columns are created using deep reactive ion etching, and individually addressable rows are made during a metal patterning step. In addition, these TOBE CMUTs can currently only be accessed from the top. A detailed description of the patterned SOI wafer fabrication can be found in [11]. CMUTs consist of ~42x42 um rectangular, low-stress (< 100 MPa) nitride membranes over a 350 nm gap. Half-area top electrodes were formed using patterned aluminum. The membrane was 3.66 µm thick. TOBE fabrication can also be accomplished using wafer-bonding or other methods as found in [5]. Fig. 3.2 shows an image of the fabricated TOBE CMUT array under a scanning electron microscope (SEM).

The TOBE CMUT used was a 40×40 element array contained in a 7×7 mm die. The TOBE die was wirebonded to a CFP80 package and attached to a custom printed circuit board with an attachable tank for oil immersion testing. Data was received from a single element of the TOBE CMUT. One column was connected to a high voltage bias while the remaining columns were grounded through grounding caps. Up to 4 row signals were routed through amplifiers for digitization using a multi-channel data acquisition system. The single element signal was read out through the corresponding row. To mimic a large 82×82 TOBE array, we raster scanned the active element(s) over a larger area. We used a step size of 243 µm to create a synthetic aperture of approximately 2×2 cm. Our target phantom was a human hair immersed in oil. An Nd:YAG laser (Continuum Surelight III, San Jose, CA; 8 ns pulses, 10 Hz repetition, ~20 mJ/cm^2) was used to excite the hair phantom. Signals from rows were amplified before being acquired by a data acquisition card. This setup was repeated with the hair at 3 different depths separated by 2 mm. The sample rate was 125 MS/s. The acquired data was then dynamically focused using MATLAB (MathWorks Inc.) along the rows and columns to create 82 high resolution 2D slices that were then stitched together in VolView (Kitware Inc., Clifton Park, NY) to create a 3D photoacoustic image.

The images from different depths are overlaid so that each 2D slice contains the crossection of 3 hairs spaced 2 mm apart. Fig. 3.3 (a) shows a 2D dynamically focused image containing the crossections of 3 hairs spaced 2 mm apart in depth. Fig. 3.3 (b) shows the 3D photoacoustic images of the 3 hairs at different depths. The frequency response of the beamformed data is shown in Fig. 3.4. In an oil immersion, we found the center frequency of our TOBE CMUT devices to be 3.7 MHz and the bandwidth to be 3.9 MHz. The axial and lateral resolution were found using the full width at half maximum (FWHM), which is the width where the magnitude of the signals falls by half or -6 dB. $\text{Magnitude} = 20 \cdot \log\left(\frac{\text{Signal}}{\text{Max Signal}}\right)$. We found the axial resolution to be 296 µm and the lateral resolution to be 866 µm. Fig. 3.5 show the lateral point-spread functions.

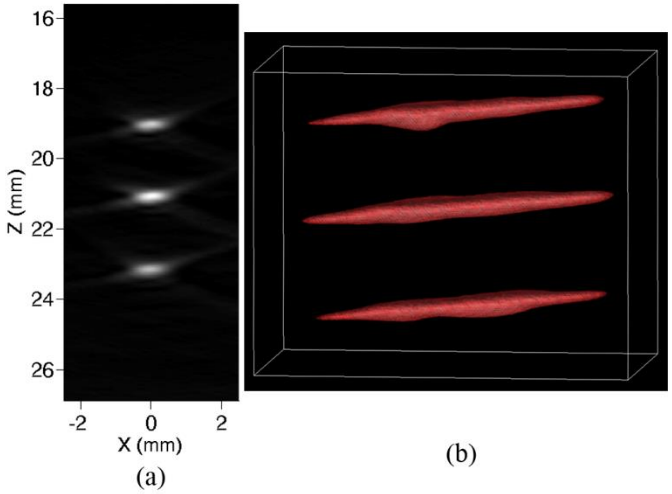

(a)

(b)

Figure 3.3. (a) Photoacoustic B-Scan and (b) 3D image of a hair phantom.

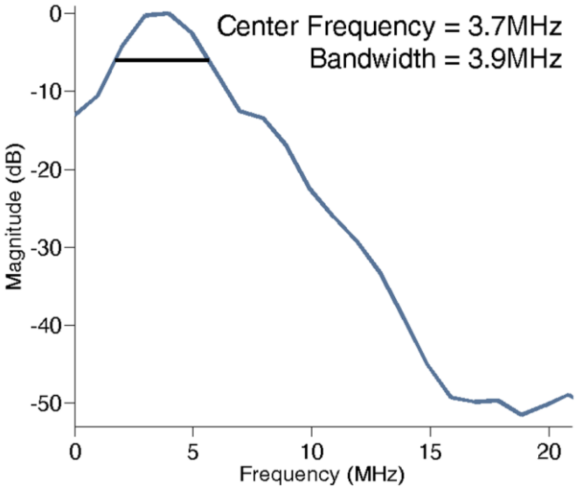

Figure 3.4. Frequency-response of the photoacoustic signals from a hair measured with TOBE CMUT elements.

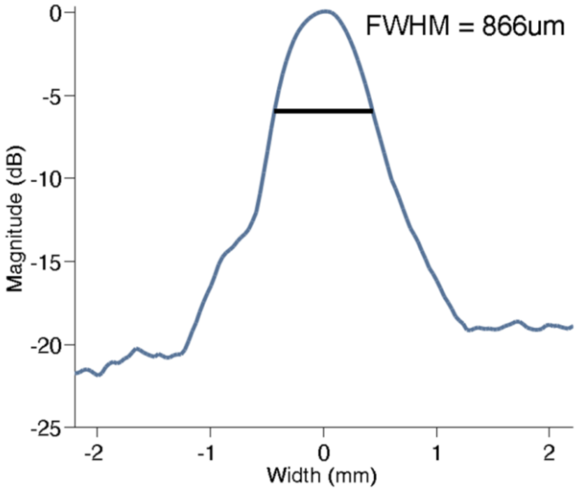

Figure 3.5. Cross-range maximum amplitude lateral point spread function.

The theoretical lateral resolution can be found using the equation $\text{lateral resolution} \approx 1.4 f_{\#}\lambda = 723\ \mu\text{m}$ given the active aperture is limited to $f_{\#} \sim 1.3$ during beamforming. This is comparable to the measured value of 866 µm, especially considering the hair width is ~100 µm. The measured FWHM axial resolution of 296 µm is slightly less than the center-frequency wavelength, as is expected since the fractional bandwidth is 107%.

This experiment represents the first 3D photoacoustic images taken with our TOBE CMUT devices. This experiment demonstrates that TOBE CMUTs can obtain high resolution 3D photoacoustic images. Future work may involve fabrication of large TOBE arrays for the acquisition of fast 3D photoacoustic images using a highly parallelized data acquisition system to leverage the full capabilities of TOBE CMUTs. This paper represents a promising step forward in substantiating the use of TOBE CMUTs to quickly generate images in photoacoustic imaging and other imaging modalities.

References

1. O. Oralkan, A. S. Ergun, C. Cheng, J. A. Johnson, M. Karaman, T. H. Lee, and B. T. Khuri-Yakub, "Volumetric ultrasound imaging using 2-D CMUT arrays," IEEE Trans. Ultrason. Ferroelectr. Freq. Control **50,** 1581-1594 (2003).

2. I. O. Wygant, X. Zhuang, D. T. Yeh, O. Oralkan, A. S. Ergun, M. Karaman, and B. T. Khuri-Yakub, "Integration of 2D CMUT arrays with front-end electronics for volumetric ultrasound imaging," IEEE Trans. Ultrason. Ferroelectr. Freq. Control **55,** (2008).

3. D. T. Yeh, O. Oralkan, I. O. Wygant, M. O'Donnell, and B. T. Khuri-Yakub, "3-D ultrasound imaging using a forward-looking CMUT ring array for intravascular/intracardiac applications," IEEE Trans. Ultrason. Ferroelectr. Freq. Control **53,** 1202-1211 (2006).

4. J. T. Yen, J. P. Steinberg, and S. W. Smith, "Sparse 2-D array design for real time rectilinear volumetric imaging," IEEE Trans. Ultrason. Ferroelectr. Freq. Control **47,** 93-110 (2000).

5. A. Sampaleanu, P. Zhang, A. Kshirsagar, W. Moussa, and R. Zemp, "Top-orthogonal-to-bottom-electrode (TOBE) CMUT arrays for 3-D ultrasound imaging," IEEE Trans. Ultrason. Ferroelectr. Freq. Control **61,** 266-276 (2014).

6. C. E. Demore, A. W. Joyce, K. Wall, and G. R. Lockwood, "Real-time volume imaging using a crossed electrode array," IEEE Trans. Ultrason. Ferroelectr. Freq. Control **56,** 1252-1261 (2009).

7. C. H. Seo and J. T. Yen, "A 256 x 256 2-D array transducer with row-column addressing for 3-D rectilinear imaging," IEEE Trans. Ultrason. Ferroelectr. Freq. Control **56,** (2009).

8. A. S. Logan, L. L. Wong, A. I. Chen, and J. T. Yeow, "A 32 x 32 element row-column addressed capacitive micromachined ultrasonic transducer," IEEE Trans. Ultrason. Ferroelectr. Freq. Control **58,** 1266-1271 (2011).

9. A. S. Logan, L. L. Wong, and J. T. Yeow, "2-D CMUT wafer bonded imaging arrays with a row-column addressing scheme," in *Ultrasonics Symposium (IUS), 2009 IEEE International,* Anonymous (IEEE, 2009), pp. 984-987.

10. S. Calmes, C. Cheng, F. Degertekin, X. Jin, S. Ergun, and B. Khuri-Yakub, "Highly integrated 2-D capacitive micromachined ultrasonic transducers," in *Ultrasonics Symposium, 1999. Proceedings. 1999 IEEE,* Anonymous (IEEE, 1999), pp. 1163-1166.

11. P. Zhang, G. Fitzpatrick, T. Harrison, W. A. Moussa, and R. J. Zemp, "Double-SOI wafer-bonded CMUTs with improved electrical safety and minimal roughness of dielectric and electrode surfaces," J Microelectromech Syst **21,** 668-680 (2012).

4. Feasibility of Modulation Encoded TOBE CMUTs for Real-Time 3D Imaging

4.1 Introduction

Top orthogonal to bottom electrode (TOBE) capacitive micromachined ultrasound transducers (CMUTs) [1, 2] are a type of crossed-electrode 2D array architecture where top electrode rows are routed orthogonal to bottom electrode columns. Other similar crossed-electrode piezoelectric [3, 4] and CMUT [5, 6] arrays have previously been proposed. The key difference is that our TOBE CMUTs allow for dominant single element control at the intersection of a biased column and a transmitting or receiving row, allowing for full focusing capabilities. Previous architectures relied on multiplexing resulting in limited one dimensional focusing. The 2D TOBE architecture with dominant element control relies on bias sensitivity, and thus cannot be implemented in piezoelectrics and is specific to CMUTs.

Real-time 3D imaging applications require 2D ultrasound transducer arrays. A fully wired 2D ultrasound transducer array allows an entire 3D image to be obtained and have been demonstrated for volumetric imaging [7, 8]. However, a fully wired 2D array requires an unfeasibly large number of channels for large arrays. An N×N 2D array would require N^2 channels, so for a 1000×1000 2D array, a million channels would be required. This poses a significant problem due to cost and practicality. To avoid channel complexity, current state of the art uses embedded complimentary metal-oxide-semiconductor (CMOS) microbeamforming electronics to reduce the channel requirements. The trade-off is that an N×N array would require at least N image acquisitions to acquire a 3D image if signals from all elements are to be used. Our TOBE CMUT arrays can provide similar performance without the need for integrated electronics. The TOBE CMUT architecture is capable of obtaining a 3D image in N image acquisitions using only N channels for an N×N array [1, 2].

We propose a technique that could significantly increase 3D image acquisition speed called modulation encoding. Modulation encoded TOBE CMUTs can potentially acquire a 3D image in a single image acquisition. In this paper, we present the feasibility of modulation encoded TOBE CMUTs. This includes theory, feasibility data, and future improvements that would enable crosstalk-mitigated modulation encoding.

4.2 Theory

If more than one column is biased, then the signal read out from any given row will be a mixture of signals received from each active column, Fig. 4.1 (a). In modulation encoded TOBE CMUTs, a different high-frequency carrier wave is applied to each column in addition to the bias. The signal read out from each row, when all columns are active, will still contain a mixed signal, but it will also contain the signal from each column modulated on different carrier frequencies. In the frequency domain, this appears as side lobes on either side of the carrier frequency, Fig. 4.1 (b).

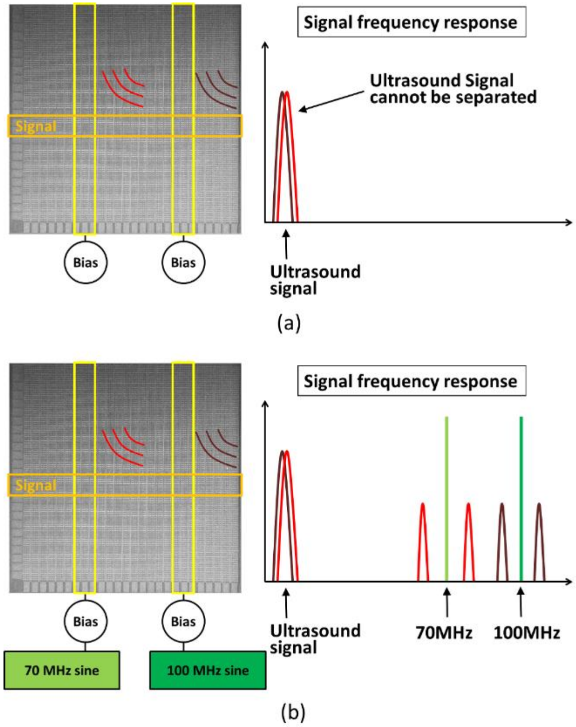

Figure 4.1. Simultaneous signal receive in (a) regular TOBE CMUTs vs. (b) modulation TOBE CMUTs.

These modulated signals can be filtered and demodulated to obtain the signal from every column. Fig. 4.2 shows the process where we first bandpass filter, then multiply by the carrier frequency in the time domain (convolution in the frequency domain), and then low pass filter to obtain the original signal from a column. With this method an entire 3D data set can be obtained in a single image acquisition while still having TOBE dominant single element control.

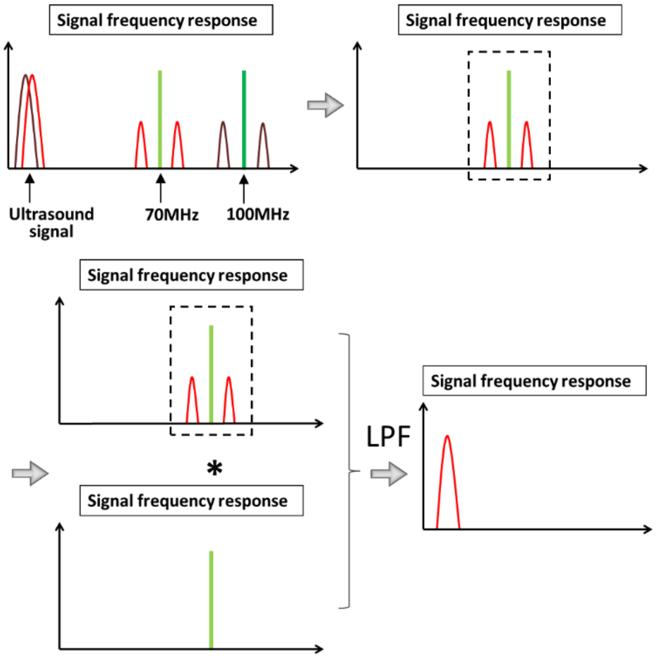

Figure 4.2. Demodulation summary for signals modulated by 70 MHz and 100 MHz carrier frequencies. The carrier and side lobes are bandpass filtered, convolved with the carrier, and then low pass filtered (LPF) to obtain the original signal.

Capacitance at row r and column c, C_{rc}, is modulated as $C_{rc} \cong C_o + \delta C_{rc} \cos(\omega t + \varphi_{rc})$, to first order for small perturbations. Since the charge is $q = CV$, the current from each CMUT cell along row r is given as

$$i_{rc}(t) = \frac{\partial E_c C_{rc}}{\partial t}$$

Now consider that the bias signal on column c has a carrier/modulation wave riding on top of a DC bias: $E_c(t) = E_0 + E_m \sin(\omega_c t)$, where $\omega_c = \omega_m + (c-1)\Delta\omega_m$ is a modulation frequency for column c. ω_m is chosen to be far above membrane resonance frequency and such that the 1/e acoustic penetration depth at this frequency is comparable with the pre-amp saturation-recovery time or dead-zone. $\Delta\omega_m$ is the frequency increment of the modulation frequency between columns, which should be greater than $\Delta\omega$, the bandwidth of the ultrasonic signal. E_m is the modulation amplitude. The current $i_{rc}(t)$ from column c contributing to row r has nonlinear mixing sum and difference frequency components

$$i_{sum,rc}(t) \propto E_m \delta C_{rc} \sin[(\omega_c + \omega)t + \varphi_{rc}]$$

$$i_{diff,rc}(t) \propto E_m \delta C_{rc} \sin[(\omega_c - \omega)t - \varphi_{rc}]$$

Assuming trans-impedance amplifiers and that there is minimal crosstalk between cells, the voltage out from row r is proportional to the sum of the currents: $v_r(t) \propto \sum_{c=1}^{N} i_{rc}(t)$. The receive signal across row r will thus be a complex mixture of signals at ultrasound frequencies (several MHz) and modulated about high-frequency column modulation bands (100's of MHz).

If we bandpass filter about band $\omega_c \pm (\omega + \frac{\Delta\omega_m}{2})$, we can demodulate by beating against $\sin[\omega_c t]$ or $\cos[\omega_c t]$ and low-pass filtering to recover the signal from the CMUT in row r and column c. Both amplitude and phase can be recovered. In this way it should be possible to use digital bandpass filters to extract the signals from all the elements in the NxN 2D array simultaneously using only N receive channels. The above theory predicts that the sum and different frequency amplitudes will be dependent on the modulation amplitude and the capacitive perturbation δC_{rc}, which in turn depends on the strength of the incoming pressure wave and the bias-voltage-dependent sensitivity.

4.3 Experiments

Experiments are performed in immersion using 40×40 element, 7×7 mm TOBE CMUT dies that are wirebonded to CFP80 packages. The fabrication of TOBE CMUTs has been previously discussed in great detail and is not discussed here [1, 9]. The wirebonded packages are attached to printed circuit test boards with attachable tanks for oil immersion. High-frequency carrier frequencies were supplied using either high-frequency oscillators (ZX95-200-S+, Mini-Circuits, Brooklyn, NY) or a high-frequency function generator (Rigol, DG4102). High-frequency carriers were implemented as shown in Fig. 4.1 (b) and Fig. 4.4. Active columns are biased using a DC voltage supply. Ultrasound was applied to the modulated TOBE CMUTs using a focused ultrasound transducer (SLIR10-02, CD International Technology Inc., Santa Clara, CA) driven by a 7.1 MHz sinusoid, to match the center frequency of the TOBE CMUT, at a 1 MHz burst frequency using a function generator (AFG3101, Tektronix Inc., Beaverton, OR). Signals are then amplified before being recorded by a high-frequency oscilloscope (DPO 7054, Tektronix Inc.). All signals were demodulated and processed using MATLAB (MathWorks Inc.). Filtering was done using ideal digital filters.

4.3.1 Modulation Theory and Receive Sensitivity Map

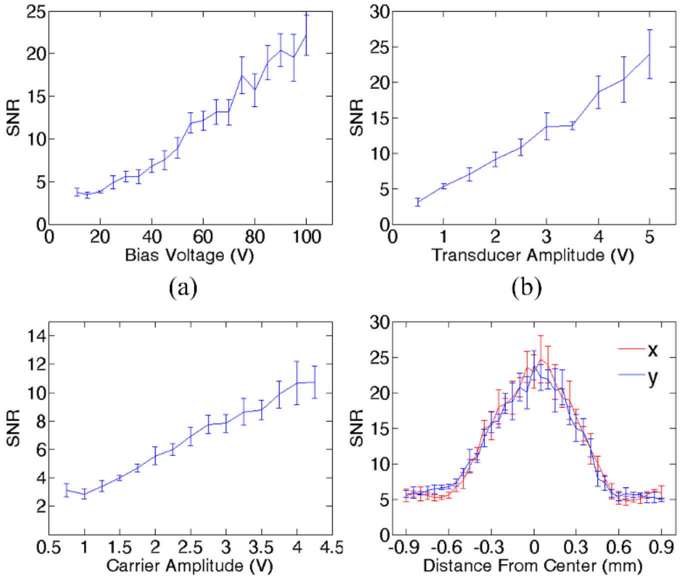

(a) (b)

(c) (d)

Figure 4.3. (a) SNR of demodulated signal vs bias voltage, (b) SNR of demodulated signal vs transducer amplitude (incident pressure), (c) SNR of demodulated signal vs carrier frequency amplitude, and (d) receive sensitivity map of the demodulated signal for the x and y direction.

To validate the principles of modulation encoding we first test some of the conclusions from theory. The theory predicts that the SNR of our demodulated signal increases with bias voltage, carrier amplitude, and incident pressure. We perform these tests using a single channel modulation. A DC bias and a carrier frequency is applied to the column while the receive signal is read out from a row. The modulated TOBE receive sensitivity for the x and y directions are also found by scanning the ultrasonic focus across the active row-column element. The results are shown in Fig. 4.3.

As predicted in the theory, the SNR increases with bias voltage, transducer amplitude (incident pressure), and carrier frequency amplitude. The linear increase with carrier amplitude is especially important as this means the SNR for modulation encoded TOBE CMUTs can approach the SNR of previously-reported TOBE CMUTs by increasing the amplitude of the carrier frequency. The modulated TOBE receive sensitivity map is as expected with higher sensitivity around the desired active element.

4.3.2 High-Frequency Crosstalk and Proposed Solution

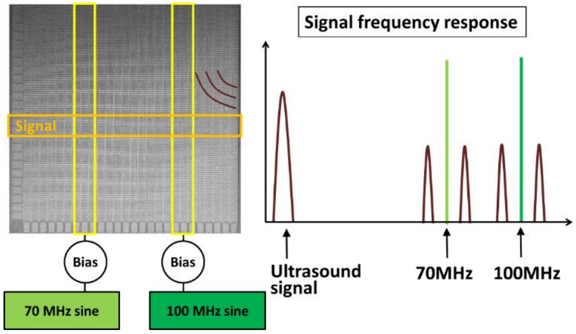

Figure 4.4. Diagram of 2 channel modulation showing high-frequency crosstalk.

We applied a focused ultrasound signal to an element in a column modulated at 100 MHz while also modulating another column at 70 MHz. The setup was similar to Fig. 4.1 (b), except ultrasound was only applied to the 100-MHz column. We expected to see a frequency response with side lobes only on the 100-MHz frequency, but we instead found side lobes on both carrier frequencies, Fig. 4.4.

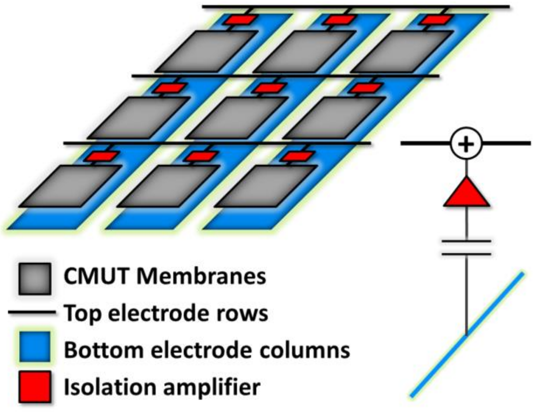

Figure 4.5. Proposed solution to prevent high-frequency crosstalk: (top left) top view, (bottom right) side view.

This result is likely due to high-frequency carriers travelling from one column across a row to another column. One potential solution to this capacitive crosstalk problem is to implement isolation amplifiers between each intersecting row and column. This is illustrated in Fig. 4.5. This would require co-integration of MEMS and electronics and was not realized at this time. However, we proposed a simple experiment to mimic essential features of this future architecture to test its feasibility. Signal detected away from the desired element could also be due to side lobes from the source, crosstalk associated with coupling through the substrate, or even other electrical crosstalk mechanisms.

4.3.3 Two Channel Modulation using Proposed Solution

To test our solution we set up another experiment using two TOBE CMUT devices and two test boards. In this experiment, the high-frequency carrier is applied to columns on two separate TOBE devices. The row output from each is then connected to separate external amplifiers linked via a bias tee before being read by an oscilloscope, Fig. 4.6. The bias tee acts as the row that the high-frequency carriers could potentially cross, and the amplifier will prevent the high-frequency carriers from entering the adjacent column (adjacent TOBE CMUT).

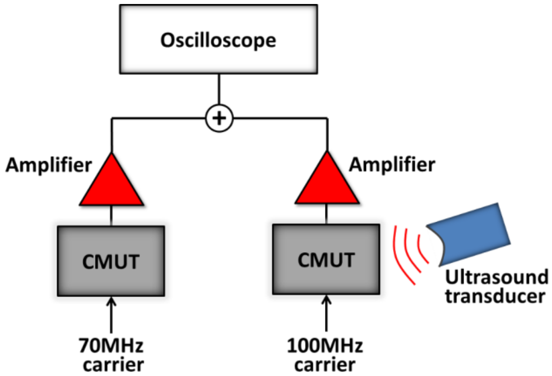

Figure 4.6. Setup for 2 channel modulation using proposed solution.

The results show that our proposed solution was successful in blocking high-frequency carriers from travelling across rows. When we demodulate the 100-MHz signal we recover our signal, Fig. 4.7 (b), but when demodulate the other carrier we recover only noise, Fig. 4.7 (a). This can also be seen in the frequency response where side lobes can only be seen on the 100-MHz carrier, Fig. 4.7 (c). In Fig. 4.7 (a), there appears to be a continuous signal leak of 7-MHz frequency. However, this is likely noise. Because demodulated signals are obtained by bandpassing certain frequency ranges, any noise will also be at the bandpassed frequency range which is around 7 MHz in this case. In Fig. 4.7 (c), there appears to be undesired peaks at 30 and 40 MHz. This may be due to amplifier nonlinearities or mixing of the modulation components due to imperfect isolation mode rejection ratios of the amplifiers. Future work will require optimization of electronics to further reject these unwanted signals.

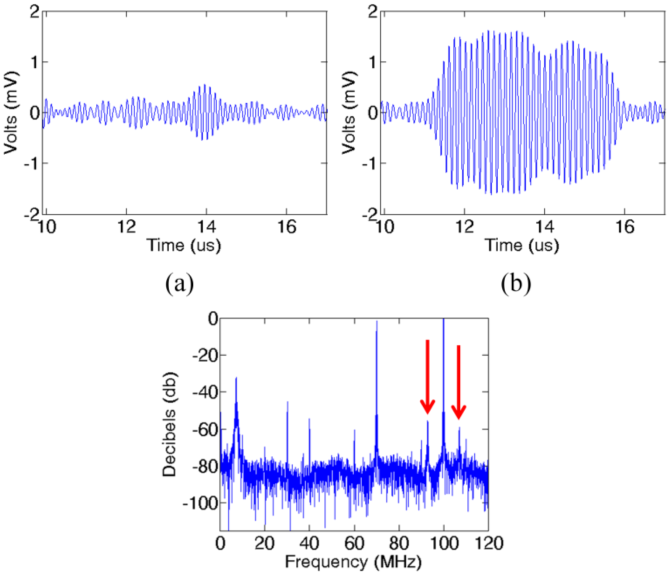

(a) (b)

(c)

Figure 4.7. (a) No signal on the 70-MHz demodulated signal, (b) signal on the 100-MHz demodulated signal, and (c) frequency response showing side lobes on the 100-MHz carrier frequency (red arrows).

4.4 Discussion

The modulation encoding scheme is a new paradigm for 2D arrays because it theoretically permits signals from every element of an NxN 2D array to be read-out simultaneously using only N high-bandwidth channels using frequency multiplexing. The throughput may be limited in bandwidth by present electronics. With receive signal bandwidth of < 20 MHz, and using modulation frequencies between 100 MHz and 2 GHz (100, 120, 140, …. 2000 MHz), each analog-to-digital converter would require several GHz bandwidth. This is non-trivial but would enable nearly two orders of magnitude higher data throughput than present linear arrays. Sparse array and compressed sensing methods could be used to lower bandwidth requirements. It should also be noted that current trends in software-defined radio and other market sectors are driving down costs of such multi-GHz bandwidth integrated circuits. Hence, there is a pathway for economically-viable implementation. Parallel beamformers may also be required to keep up with the high data rates.

A future improvement is modulating on both a sine and a cosine carrier at the same modulation frequency. This would require phase-locking the sine and cosine carriers. Due to hardware requirements, it was not implemented in this paper. However, if this was implemented, it would allow us to cut the modulation frequency range and data rate in half. We leave this for future work.

Additionally, one will need to be careful regarding transmission line effects to and from the TOBE CMUTs as well as along the TOBE CMUT rows and columns.

Signal-to-noise ratios were shown to be linear with modulation amplitude. Note that an effective biasing will occur due to the RMS of the modulation creating a mean displacement. The sum of the DC bias and the modulation RMS voltage is bounded to be less than the collapse voltage for pre-collapse operation. This along with parasitic capacitance will limit SNR. However, careful design of integrated amplifiers could ensure best-possible SNR.

Our proposed TOBE CMUTs with isolation amplifier between the rows and columns can be implemented in a number of ways. Flip-chip packaging or low-temperature wafer bonding on CMOS electronics could be used, and the amplifiers could be designed to reduce noise due to non-linear mixing effects between amplifiers.

4.5 Conclusion

Modulation encoded TOBE CMUTs is the first method to show the promise of acquiring a full 3D image in a single pulse using an N×N 2D array with only N channels. This could significantly increase the speed of real-time 3D ultrasound and photoacoustic imaging. While high-frequency crosstalk is a problem for modulation encoding on our current devices, we proposed and tested a viable solution by implementing isolation amplifiers to block high-frequency crosstalk. We have demonstrated the validity of the theory and have shown that the SNR for modulation encoded TOBE CMUTs could potentially be as good as the SNR for regular TOBE CMUTs given a large enough carrier frequency amplitude. While modulation encoding in TOBE CMUTs is still early in development, it represents the first idea ever proposed capable of such high speeds with low channel requirements. This new ultrasound transducer technology shows potential for many real-time 3D ultrasound imaging applications and may have many more novel uses.

References

1. A. Sampaleanu, P. Zhang, A. Kshirsagar, W. Moussa, and R. Zemp, "Top-orthogonal-to-bottom-electrode (TOBE) CMUT arrays for 3-D ultrasound imaging," IEEE Trans. Ultrason. Ferroelectr. Freq. Control **61,** 266-276 (2014).

2. R. K. Chee, A. Sampaleanu, D. Rishi, and R. J. Zemp, "Top orthogonal to bottom electrode (TOBE) 2-D CMUT arrays for 3-D photoacoustic imaging," IEEE Trans. Ultrason. Ferroelectr. Freq. Control **61,** 1393-1395 (2014).

3. C. E. Demore, A. W. Joyce, K. Wall, and G. R. Lockwood, "Real-time volume imaging using a crossed electrode array," IEEE Trans. Ultrason. Ferroelectr. Freq. Control **56,** 1252-1261 (2009).

4. C. H. Seo and J. T. Yen, "A 256 x 256 2-D array transducer with row-column addressing for 3-D rectilinear imaging," IEEE Trans. Ultrason. Ferroelectr. Freq. Control **56,** (2009).

5. A. S. Logan, L. L. Wong, A. I. Chen, and J. T. Yeow, "A 32 x 32 element row-column addressed capacitive micromachined ultrasonic transducer," IEEE Trans. Ultrason. Ferroelectr. Freq. Control **58,** 1266-1271 (2011).

6. A. S. Logan, L. L. Wong, and J. T. Yeow, "2-D CMUT wafer bonded imaging arrays with a row-column addressing scheme," in *Ultrasonics Symposium (IUS), 2009 IEEE International,* Anonymous (IEEE, 2009), pp. 984-987.

7. O. Oralkan, A. S. Ergun, C. Cheng, J. A. Johnson, M. Karaman, T. H. Lee, and B. T. Khuri-Yakub, "Volumetric ultrasound imaging using 2-D CMUT arrays," IEEE Trans. Ultrason. Ferroelectr. Freq. Control **50,** 1581-1594 (2003).

8. I. O. Wygant, X. Zhuang, D. T. Yeh, O. Oralkan, A. S. Ergun, M. Karaman, and B. T. Khuri-Yakub, "Integration of 2D CMUT arrays with front-end electronics for volumetric ultrasound imaging," IEEE Trans. Ultrason. Ferroelectr. Freq. Control **55,** (2008).

9. P. Zhang, G. Fitzpatrick, T. Harrison, W. A. Moussa, and R. J. Zemp, "Double-SOI wafer-bonded CMUTs with improved electrical safety and minimal roughness of dielectric and electrode surfaces," J Microelectromech Syst **21,** 668-680 (2012).

5. Multifrequency Interlaced CMUTs for Photoacoustic Imaging

5.1 Introduction

Photoacoustic (PA) imaging uses differences in optical absorption to produce high contrast images. PA imaging has the potential for the clinical detection and localization of tumors [1-3] and atherosclerotic plaques [4-6]. Contrast agents such as dyes and nanoparticles are often used to give added contrast. These contrast agents can be genetically encoded [7-9] or injected and molecularly targeted, which result in molecular images that can help to identify and characterize disease. Nanoparticles, for example, can be molecularly targeted to enhance the detection of cancer cells [10-13]. In addition, dyes such as indocyanine green can help to enhance tumour contrast to surrounding tissue [14]. Spectroscopic PA (sPA) imaging is the spectral demixing of PA images of multiple optical wavelengths to quantitatively estimate the concentration of optical absorbers in the body. sPA imaging has been used to image hemoglobin oxygen saturation, total hemoglobin concentration, contrast agent dyes, nanoparticles, and lipid concentrations [4, 15, 16]. Applications include tumour staging in breast cancer [17], lipid monitoring in atherosclerotic plaques [18], and mapping of dye and nanoparticle concentrations [16]. Concentrations of dyes or contrast agents are often only present in diffuse concentrations in the body. PA signals from diffuse concentrations of contrast agents are poorly detected by high-frequency transducers typically used for high resolution PA images. This is in part because the PA signal frequency of an optical absorber is size dependent [19]. Often diffuse distributions of optical dyes or molecularly targeted nanoparticles have slowly-varying spatial profiles and will hence produce very low PA frequencies that are difficult to detect with high-frequency transducers used to visualize microvascular networks. Ku et al. has demonstrated improved PA images using multiple-bandwidth detection [20] using only single-element transducers.

There have been several attempts to develop multifrequency ultrasound array transducers using traditional piezoelectric technology. Stephens et al [21] developed a dual-frequency array transducer consisting of 3 linear arrays, where the central linear array could be used for high frequency imaging while the outer low-frequency arrays could be used for ultrasound therapy. This design has poor beam alignment and compromised elevational focusing for both imaging and therapy applications. Additionally, it is difficult to apply two different acoustic matching layers on the low- and high-frequency arrays. T. Azuma et al. [22] fabricated a 0.5-and 2-MHz dual layer transducer with a frequency selective isolation layer, but non-trivial acoustic impedance matching was again required. A similar dual layer design featuring 6.5 MHz and 30 MHz has also recently been introduced [23]. Gessner et al. [24, 25] demonstrated a dual-frequency (4-MHz transmit and 30-MHz receive) transducer for dual-frequency contrast ultrasound imaging and acoustic angiography, but their system required mechanical scanning and had non-ideally co-aligned beam profiles. Guiroy et al. [26] demonstrate a similar dual-frequency (4-MHz transmit and 14-MHz receive) transducer with curved elements for enhanced sensitivity. None of these prior works has investigated multifrequency arrays for PA applications.

CMUTs offer several advantages over piezoelectric transducers for multifrequency and PA applications. A number of studies have demonstrated the use of CMUTs for PA imaging [27-30]. CMUTs have excellent PA imaging potential as they exhibit wider bandwidth, easier electronic integration, and less restrictive fabrication allowing for larger arrays, higher frequencies, and new architectures and geometries [27-30]. For multifrequency applications, multifrequency CMUTs can be easily impedance matched by matching the radiation impedance to the transmission medium. Less restrictive fabrication greatly simplifies multifrequency transducer fabrication in CMUTs. Thickness and backing define the resonance frequency in piezoelectrics while in CMUTs, for a given membrane thickness, this is defined by transducer membrane width, which is far easier to vary within an array. Kupnik et al. proposed varying CMUT membrane sizes to develop wide-bandwidth air-coupled transducers for use in range finding and gas flow applications [31]. They showed that it was possible to obtain increased bandwidth operation when membrane sizes were varied in a monotonically increasing radial pattern from the center of the wafer. However, they did not explore multifrequency CMUTs for medical imaging applications. In addition, papers by Bayram et al [32] and Olcum et al [33] have modeled the effect of varying membrane widths on bandwidth improvements and have theoretically shown the potential for bandwidth improvement in both air and immersion operation by using this method, but they did not fabricate or test their designs. Eames et al. fabricated and modelled CMUTs that could operate at low frequencies in pre-collapse mode, and then operate at high frequencies by collapsing the top membrane onto a frame to define an effectively smaller membrane size [34, 35].

Our multifrequency interlaced CMUTs consist of 36-μm (high frequency) and 82-μm (low frequency) cells that have been interlaced on a scale smaller than the smallest operating wavelength. Transducer array elements have been fabricated with a pitch less than the wavelength of the center-operating frequency (the lambda-pitch requirement) resulting in minimal grating lobes. The shortest center-operating wavelength of our high-frequency transducer is 290 μm while the pitch of our devices can be as little as 235 μm. To the best of our knowledge, no one has taken advantage of the capabilities of CMUTs to be interlaced on a scale smaller than the shortest acoustic wavelength in water/tissue. Our interlaced low- and high-frequency CMUTs will have ideally co-aligned beam profiles with optimal imaging resolutions and minimal deleterious grating lobes.

As an extension to our conference proceedings [36], we have fabricated our multifrequency interlaced CMUTs and have demonstrated their application for wide bandwidth PA imaging. We first demonstrate via simulations that PA signal frequency is target size dependent and that our interlaced multifrequency CMUT scheme is ideal for minimal grating lobes. We characterize the resonant frequencies, beam co-alignment, and PA lateral resolutions of our devices. Finally, we present sPA images illustrating the ability to better visualize large optical absorber distributions with the low-frequency subarrays while imaging with high resolution with the high-frequency subarrays. We show that the low-frequency subarrays have improved signal-to-noise ratio for low-frequency PA content in comparison to the high-frequency subarrays. This paper is the first application of multifrequency CMUT arrays to PA imaging.

5.2 Simulation of Photoacoustic Signal

To illustrate the target size dependence of PA signals, we derive an expression for a 3D Gaussian diffuse dye distribution and simulate the PA signal at an observation point using MATLAB (MathWorks Inc.). The equation used to simulate the signals are found in [37]. The PA signal at observation field point $\boldsymbol{r}$ due to an arbitrary initial pressure distribution is given as:

$$(1) \qquad P(\boldsymbol{r},t) = \frac{1}{4\pi v_s^2}\frac{\partial}{\partial t}\left[\frac{1}{v_s t}\int P_0(\boldsymbol{r}')\delta\left(t-\frac{|\boldsymbol{r}-\boldsymbol{r}'|}{v_s}\right)d\boldsymbol{r}'\right]$$

Here $P_0(\boldsymbol{r}) = \Gamma\mu_a(\boldsymbol{r})\Phi(\boldsymbol{r})$ models the initial pressure distribution where Γ is the Grüneisen parameter (assumed a constant), μ_a is the optical absorption coefficient distribution, and Φ is the optical fluence. To model a diffuse dye distribution, we consider a weak absorption distribution where the fluence is approximately constant and the absorption distribution is a spherical Gaussian shape. Then

$$(2) \qquad \mu_a(\boldsymbol{r}) = \mu_{a0}\exp\left(-\frac{|\boldsymbol{r}-\boldsymbol{r}'|^2}{2\sigma^2}\right)$$

Let the sphere be centered at the origin and the observation point be located a distance r from the center with a standard deviation of σ. To evaluate the PA signal from a diffuse slowly varying distribution at this observation point, we consider spherical shells of infinitesimal thickness with uniform optical absorption. The PA signal from such a shell can be written as the difference between signals from two uniform spheres of radius R_s and $R_s + \Delta R_s$. The signal from a sphere of radius R_s, equation (3), can be derived from equation (1) [37] as

$$(3) \qquad P_{R_s}(r,t) = \frac{r+v_s t}{2r}P_{U,R_S}(r+v_s t) + \frac{r-v_s t}{2r}P_{U,R_S}(-r+v_s t) + \frac{r-v_s t}{2r}P_{U,R_S}(r-v_s t)$$

where

$$(4) \qquad P_{U,R_S}(r) = P_i U(r) U(-r+R_S)$$

for $0 \leq r \leq R_S$ and where P_i is the initial pressure and U is the Heaviside step function. We define the signal from a spherical shell with inner- and outer-radius given as $[R_s, R_s + \Delta R_s]$ as

$$(5) \qquad \delta P(r,t) = P(r,t) - P_{R_s}(r,t)$$

To obtain the PA signal from a diffuse Gaussian distribution we must substitute $P_0 \exp\left(-\frac{1}{2}\frac{R_s^2}{\sigma^2}\right)$ for $P_i(R_s)$ and integrate over spherical shells. This results in the following:

$$(6) \qquad P(\boldsymbol{r},t) = P_0 \left\{\frac{r+v_s t}{2r} \exp\left(-\frac{1}{2}\frac{(r+v_s t)^2}{\sigma^2}\right) + \frac{r-v_s t}{r} \exp\left(-\frac{1}{2}\frac{(r-v_s t)^2}{\sigma^2}\right)\right\}$$

We can use equation (6) to plot the PA signal of diffuse dye distributions. Fig. 5.1 (a) shows the simulated PA signals of diffuse dye distributions represented as Gaussian distributions with Gaussian root mean square widths, σ, of 0.1 mm and 1 mm. Fig. 5.1 (b) shows the frequency spectrum of the simulated PA signals of diffuse dye distribution with σ of 0.1 mm and 1 mm. As expected, the larger optical absorber has significantly lower frequency content than the small optical absorber.

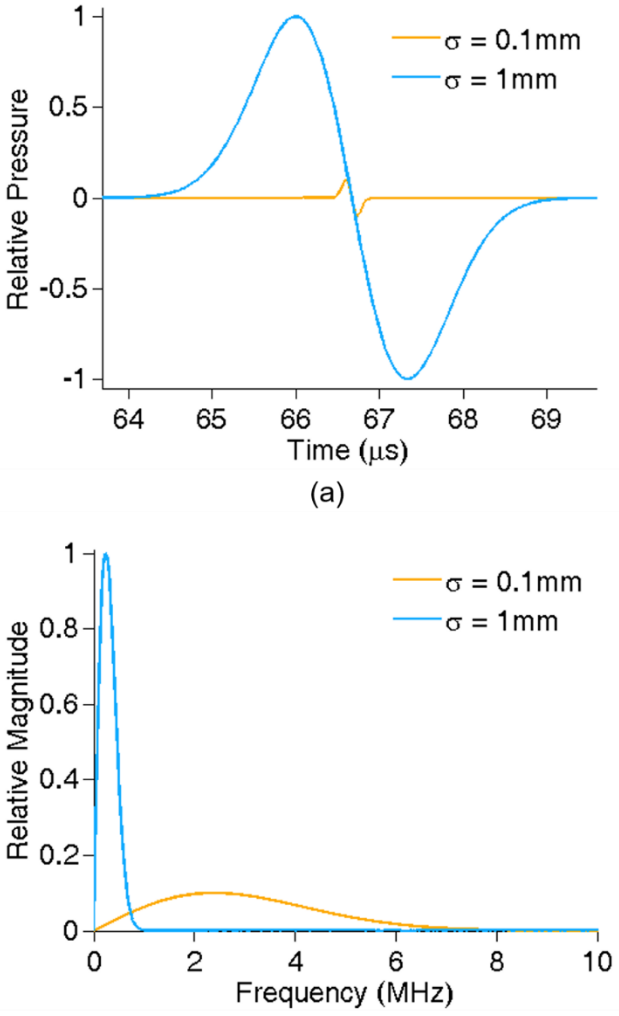

(a)

(b)

Figure 5.1. (a) Simulated PA signals from Gaussian μ_a spatial distributions and (b) spectrum of PA signals from these distributions. The more slowly-varying distributions produce significantly lower frequency content than the rapidly changing distributions.

The slowly-varying 1-mm distribution spectrum appears lower than would be detectable by many commercial and high-frequency ultrasound transducers. More sharply-defined absorption edges may produce more broadband frequency content, but this may not always be the case for contrast agents and dyes, which have a tendency to diffuse in tissues. Given that many pre-clinical PA imaging systems use high-frequency transducers to achieve high resolutions, Fig. 5.1 suggests that such transducers may miss capturing lower frequency signals important for molecular imaging applications. This motivated us to develop multifrequency transducers capable of high-resolution imaging but also with high sensitivity to diffuse optical distributions.

5.3 Simulated Beam Profiles and Pulse-Echo Point Spread Function

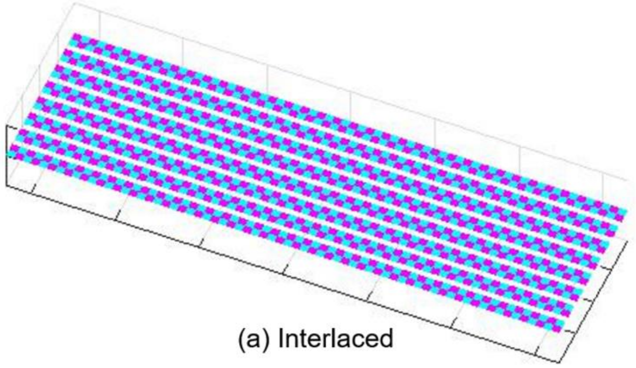
(a) Interlaced

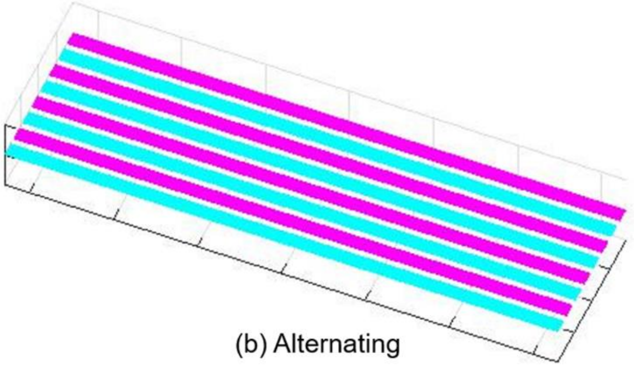
(b) Alternating

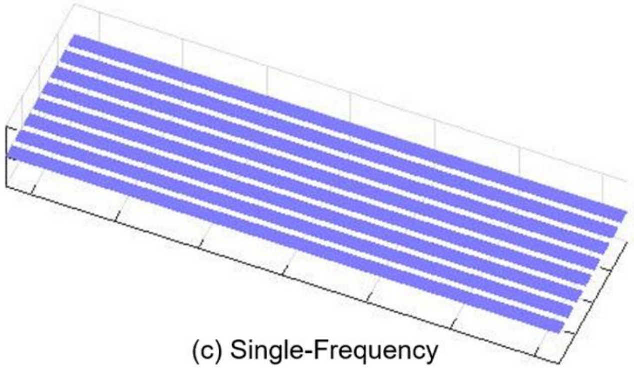
(c) Single-Frequency

Figure 5.2. Simulated transducers (showing only 8 of 99 elements used): (a) interlaced multifrequency transducer similar to our fabricated devices, (b) alternating multifrequency transducer, and (c) single-frequency transducer. Blue: 1-MHz subelements. Pink: 5-MHz subelements.

We considered several multifrequency transducer designs prior to device fabrication. To investigate the issue of grating lobes, we have simulated the acoustic receive point spread functions from several transducer designs. We use Field II in a MATLAB (MathWorks Inc.) environment to perform the simulations [38, 39]. We use three transducers for comparison: an interlaced multifrequency transducer (interlaced), an alternating multifrequency transducer (alternating), and a single-frequency transducer (single-frequency). Fig. 5.2 illustrates the transducers used but includes only 8 of the 99 elements used in the simulation.

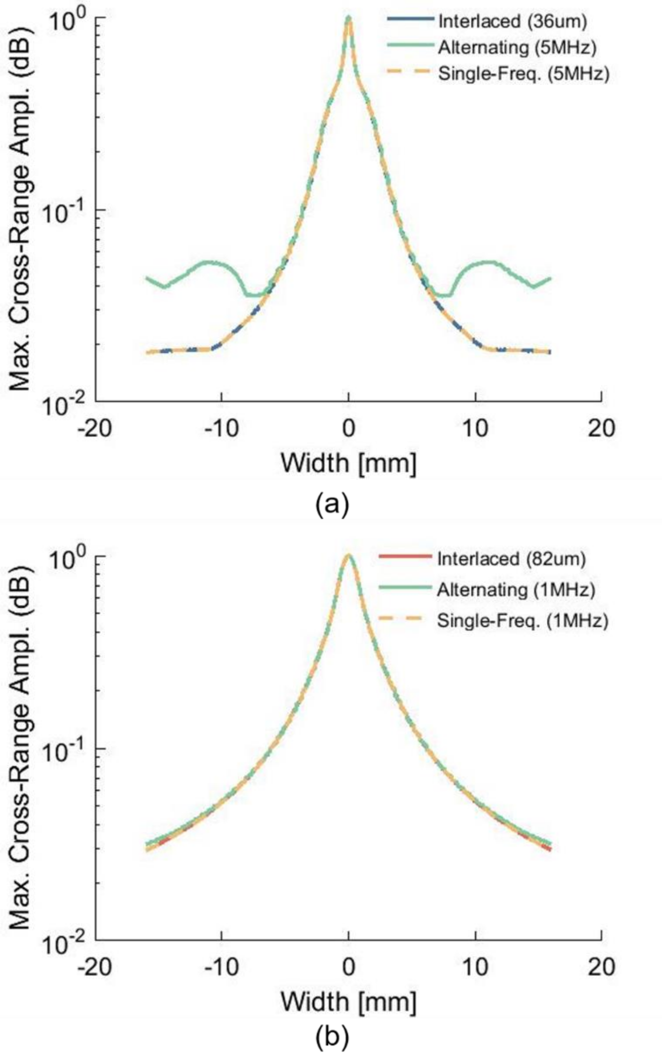

Figure 5.3. (a) Comparison of the lateral profiles of the receive point spread functions for different 5-MHz transducers and (b) comparison of the lateral profiles of the receive point spread functions for different 1-MHz transducers.

The simulated interlaced multifrequency transducer consists of interlaced 1- and 5-MHz devices. The simulated alternating multifrequency transducer consists of alternating 1- and 5-MHz center-frequency elements, and the single-frequency transducers consists of single-frequency elements of either 1- or 5-MHz center frequency. The simulation of the pulse-echo point spread function used 1.5 pulse cycles, 150-MHz sampling frequency, 1450-m/s speed of sound, 99 elements, and device dimensions consistent with the fabricated multifrequency devices (179-µm element width with 250-µm pitch and 6.596-mm height). The receive focus and elevational focusing lens focal length was set to 2 cm above the transducer. A point source was also located at this 2-cm focal position. We obtain the lateral profile of the receive point spread function by finding the maximum value for each lateral position. The lateral profile of the receive point spread function are shown for the interlaced, alternating, and single-frequency transducers operating at 5 MHz and 1 MHz separately.

Fig. 5.3 (a) and (b) shows the comparison of lateral profiles of the receive point spread functions of different transducers operating at 5 MHz and 1 MHz, respectively. The simulations show that our interlaced transducer has a point spread function similar to the single-frequency transducer but with multifrequency functionality. As predicted in theory, the grating lobes can be seen present for the 5-MHz alternating transducer but not the interlaced transducer operating at 5 MHz. The 1-MHz devices have no visible grating lobes. Minimal grating lobes are most important for the high-frequency devices, where large grating lobes can cause unwanted imaging artifacts. These results indicate that interlaced multifrequency CMUTs may be a promising multifrequency transducer architecture.

5.4 Device Design and Fabrication

We chose center frequencies of 1 MHz (low frequency) and 5 MHz (high frequency) primarily based on the convenience of device geometry. We were able to fit 4 smaller membranes into roughly the same area as a larger membrane for interlacing as shown in Fig. 5.4. Multifrequency interlaced CMUTs with a larger difference in center frequencies should be possible in future work by fitting more membranes of smaller size into the area of the larger interlaced membrane.

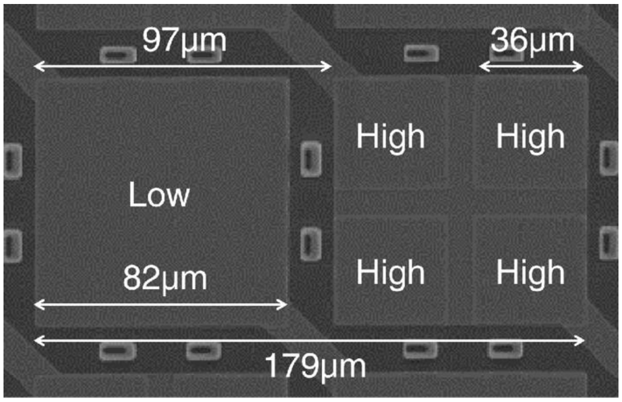

Figure 5.4. Scanning electron microscope image of interlaced 82- and 36-μm CMUTs.

We used ANSYS (ANSYS Inc., Canonsburg, PA, USA) to predict the collapse voltages and resonance frequencies of membranes used in our multifrequency devices, as described in our previous conference paper [36]. We designed linear arrays and composite single-element transducers consisting of interlaced low- and high-frequency membranes.

We fabricated the multifrequency CMUTs using a standard silicon-nitride sacrificial release process with slight modifications. The process flow is shown in Fig. 5.5. A heavily boron-doped prime wafer serves as the bottom electrode. Nitride, oxide and polysilicon are deposited sequentially. The nitride layer acts as a bottom dielectric layer and KOH-etch-stop. The oxide layer acts as an etch-stop layer for the specific inductively-coupled plasma deep-reactive ion etching (ICP-DRIE) process used on the nitride layers. Polysilicon serves as a sacrificial layer, Fig. 5.5 (a). The polysilicon layer is lithographically patterned to form the etching-channel areas, Fig. 5.5 (b). This is followed by another polysilicon deposition, Fig. 5.5 (c). This step increases the thickness of the sacrificial polysilicon in the gap area while creating a thin layer of film within the etch-channel that can be sacrificially removed. Then the polysilicon and oxide layers are patterned to define the active area, including the cavity and etching channel, Fig. 5.5 (d). The next step is the deposition of the top membrane. The top membrane is a 'sandwich structure' composed of one layer of stoichiometric silicon nitride, one layer of low-stress (< 100 MPa tensile) nitride, and another stoichiometric silicon nitride layer, Fig. 5.5 (e). The sandwich structure combines the advantages of ultra-low etch-rates of KOH on stoichiometric silicon nitride and the low-stresses of the Si_3N_4 membrane material. The higher stress of the thin stoichiometric nitride film contributes negligibly to the overall stress of the membrane. After membrane deposition, a sacrificial release window is formed by ICP-DRIE as shown in Fig. 5.5 (f). KOH wet etching is then used to etch away the polysilicon and oxide and release the membranes, Fig. 5.5 (g). Although the etch-rate of oxide is much slower than that of polysilicon, the oxide layer beneath the gap and etch-channel areas will be completely etched away during the long sacrificial etches. In order to seal the cavity and prevent membrane damage, a low stress TEOS PECVD oxide film is deposited and patterned to form etch hole sealing plugs. The TEOS oxide offers non-conformal oxide deposition so that the etch holes may be sealed without coating the gap area, Fig. 5.5 (h). All TEOS oxide is removed from active membrane areas using buffered oxide etch to ensure no added membrane stress or thickness. The next step is the etching of the nitride layer to form access holes to the bottom electrode, Fig. 5.5 (i). Finally, metallization and patterning is performed to form top electrodes, top interconnects, top electrode bond-pads, and the bottom-electrode bond-pads, Fig. 5.5 (j). We coat the final device with parylene c for electrical isolation and additional hermetic sealing in oil.

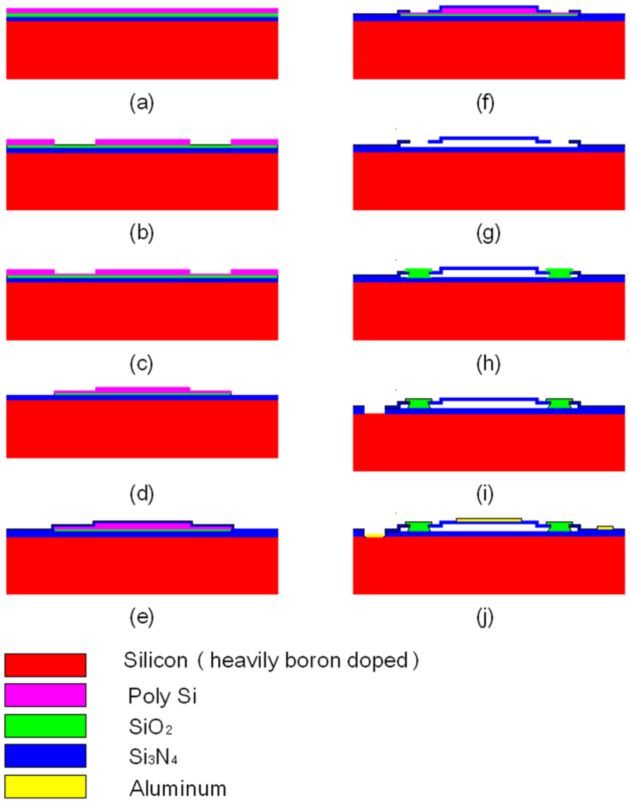

Figure 5.5. Multifrequency sacrificial release fabrication process.

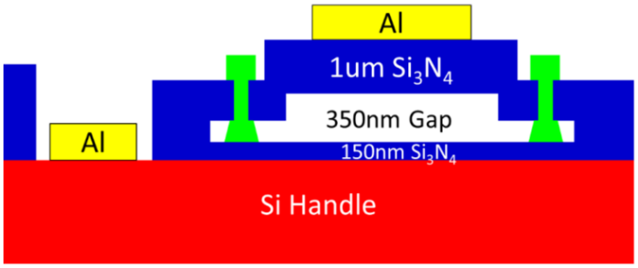

Figure 5.6. CMUT layer dimensions.

We have fabricated 7x7 mm dies containing interlaced 82-µm (low frequency) and 36-µm (high frequency) cells. Fig. 5.6 shows device layer thicknesses.

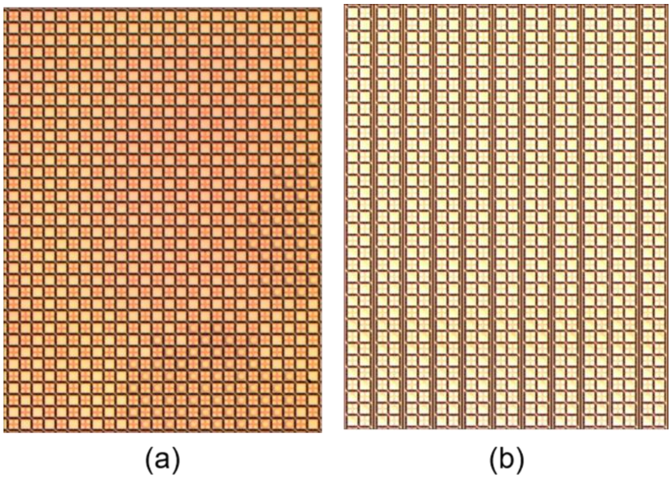

Figure 5.7. (a) Single-element arrays (68×70) (b) Linear arrays (68×2) spaced 235 µm apart to illustrate the scanning arrangement used.

Two types of arrays were fabricated and tested in our experiments. The first are 7x7 mm single-element multifrequency transducers, which have 68×70 connected sub-elements of alternating 82- and 36-µm cells, as shown in Fig. 5.7 (a). The second are linear array transducers, which have 68×2 connected sub-elements of alternating 82- and 36-µm cells. Fig. 5.4 is an example of a 1×2 section. Thus, a 68×2 linear array will have 68 of the 1×2 sections shown in Fig. 5.7, and they will alternate as shown in Fig. 5.2 (a). A 68×70 single-element array will have 68 rows and 35 columns of the 1×2 sections. In the single-element array, all of the 82-µm cells will be connected together and likewise for the 36-µm cells. Fig. 5.7 (b) is a representation of a scanned linear array as was used in our experiments. The pitch in Fig. 5.7 (b) is 250 µm, which is less than the center-frequency wavelength of the 36-µm membranes in immersion (which is 290 µm), thus maintaining the traditional lambda-pitch requirement for optimal imaging resolution. Each 68×2 linear array and 68×70 single-element array has two signal and ground bond-pads for driving the 82- and 36-µm membranes separately.

The multifrequency CMUT die was wirebonded to a CFP80 package and attached to a test fixture (CQFP80-SMA Test Fixture, CMC Microsystems) with a water-tight attachable tank for oil immersion testing, Fig. 5.8 (a). In testing the linear arrays, we mechanically scanned a single 68×2 array over a number of scan positions (n), resulting in a total array size of 68×2n (Fig. 5.7 (b) shows a 68×2n array where n = 11). Fig. 5.8 (b) shows the mechanical scanning setup.

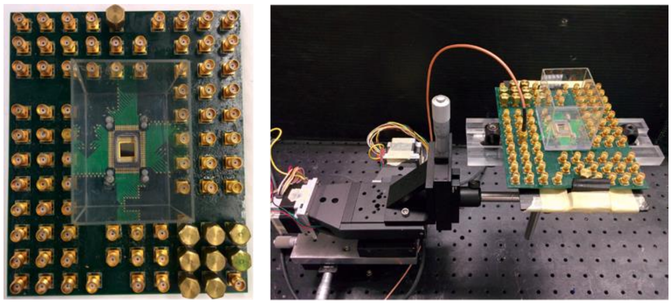

(a) (b)

Figure 5.8. (a) A multifrequency CMUT die wirebonded to a CFP80 package and attached to a test fixture with a water-tight attachable tank for oil immersion testing. (b) Mechanical scanning setup used for mechanical scanning.

5.5 Experiments

5.5.1 Actuation in Air – Single-Element Array

We use a vibrometer (MSA-500, Polytec) to image low- and high-frequency cell operations separately in a single-element array. We grounded the high-frequency cells while low-frequency cells were operating and vice versa. The 36- and 82-µm devices were biased at 100 V and 20 V, respectively. A pseudo-random signal was applied to the 36- and 82-µm devices to determine the center frequency in air. A pseudo-random signal is a signal equally weighted in all frequencies so that a resonance frequency can be detected. Fig. 5.9 shows the center frequencies of the 36- and 82-µm single-element cells in air, which were 11.08 MHz and 2.97 MHz, respectively. The 82-µm devices also had a second modal frequency at 8.85 MHz. The observed resonant frequencies of 11.08 MHz and 2.97 MHz in air are close to the simulated 10.5-MHz and 2.1-MHz resonant frequencies in air simulated using ANSYS (ANSYS Inc., Canonsburg, PA, USA) in our previous conference proceedings [36]. The collapse voltages match the simulated values of ~150 V and ~30 V for the 36- and 82-µm devices, respectively [36].

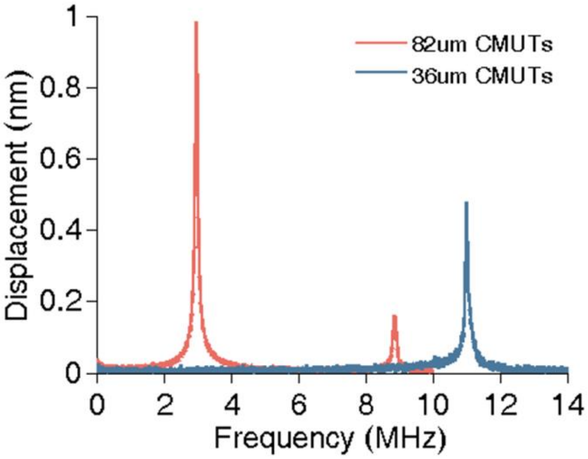

Figure 5.9. Vibrometer frequency response of 36- and 82-µm single-element devices in air.

We obtain device actuation videos by scanning the vibrometer across actuated membranes at a spacing of ~6.5 µm. We drove the 36- and 82-µm single-element subarrays using a 3-V amplitude sine wave at their resonant frequencies.

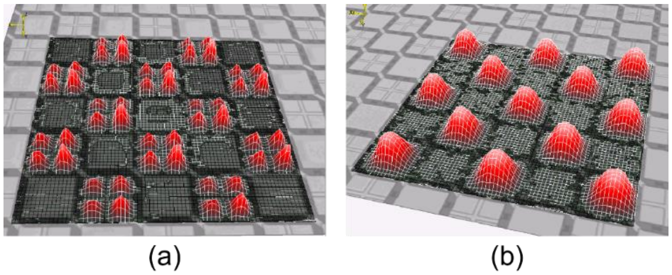

Figure 5.10. (a) Actuation of the 36-µm single-element sub-arrays when driven by a 3-V 11.08-MHz sine wave (+/-60 nm displacement range) and (b) actuation of the 82-µm single-element sub-arrays when driven by a 3-V 2.90-MHz sine wave actuation (+/-80 nm displacement range).

Fig. 5.10 shows the device actuation for the 36- and 82-µm single-element sub-arrays. Fig. 5.10 (a) contains the 36-µm single-element sub-array driven by a 3-V 11.08-MHz sine wave. Fig. 5.10 (b) contains the 82-µm single-element sub-array driven by a 3-V 2.90-MHz sine wave.

5.5.2 Immersion Center Frequency – Single-Element Array

We measured the frequency response of the single-element multifrequency arrays in oil immersion to characterize its performance in a tissue-like medium. A 7×7 mm single-element die was mounted and wirebonded onto a CFP80 package. This was then mounted onto a test fixture with attachable tank and filled with vegetable oil. The transmit pressures were detected with a hydrophone (HNP-0400, Onda), and the signal was amplified by both a pre-amp (AH-2010-DCBNS, Onda) and a 39-dB pulser-receiver amplifier (Model 5073PR, Olympus NDT) before being measured by an oscilloscope using 100-times averaging. A pulser-receiver (Model 5900PR, Olympus NDT) was used to supply a short 16-µJ pulse at a 1-kHz pulse repetition rate to the

CMUTs. A 20-V bias was applied to the 82-µm devices, and a 100-V bias was applied to the 36-µm devices. Low- and high-frequency devices were tested individually while grounding the non-active devices.

We found the center frequency of the 82-µm devices in immersion to be 1.74 MHz with a –6-dB bandwidth of 2.33 MHz, Fig. 5.11. The fractional bandwidth is 134%. The center frequency for the 36-µm devices in immersion was 5.04 MHz with a -6-dB bandwidth of 4.56 MHz, Fig. 5.12. The fractional bandwidth is 90%. There is slight overlap between the high- and low-frequency devices in the 2.760- to 2.905-MHz range. Our –6-dB sensitivity spans from 0.60-7.32 MHz. The effective mean frequency in this range is 3.9 MHz. The best fractional bandwidths reported to date for CMUTs are ~130%. Thus, an equivalent 3.9-MHz-center-frequency CMUT would only have a bandwidth of 5.1 MHz (spanning 1.4-6.5 MHz). Thus, our multifrequency array offers greater fractional bandwidth (effectively 170% fractional bandwidth) compared to most previous CMUTs using uniformly-sized membranes.

We had anticipated a drop from our in-air simulation results to immersion testing because immersion operation causes the CMUTs to be heavily-damped with wide bandwidth. The –3-dB bandwidths in immersion for the 82- and 36-µm devices are 1.39 MHz and 3.72 MHz, respectively. The oscillations in the frequency response may be due to substrate ringing modes and/or mutual acoustic interaction. Substrate ringing modes could potentially be avoided by future wafer thinning.

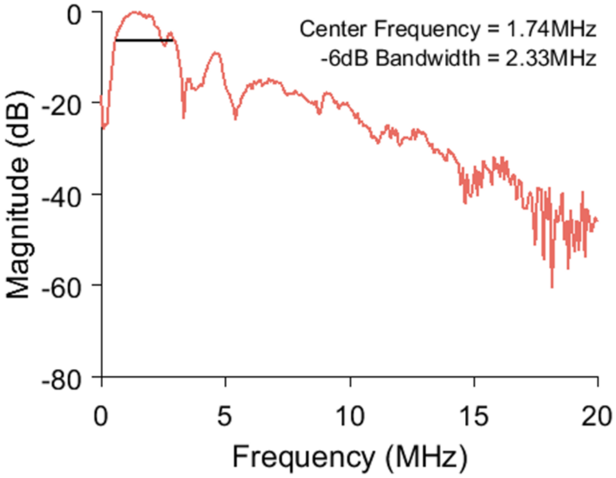

Figure 5.11. 82-µm device frequency response in oil immersion.

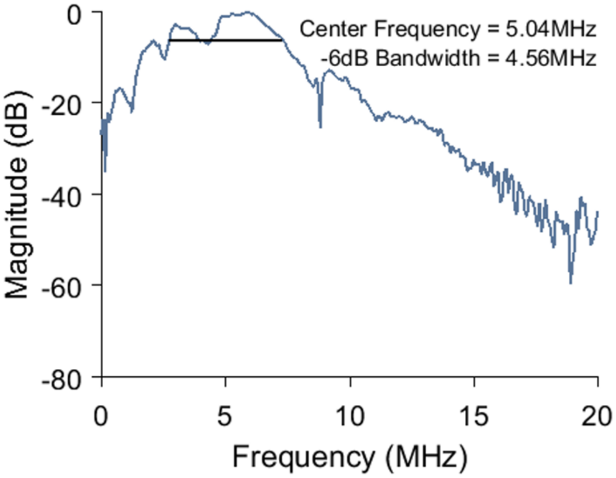

Figure 5.12. 36-µm device frequency response in oil immersion.

5.5.3 Beam Profile Co-alignment – Single-Element Array

We are using 7×7 mm single-element transducers (68×70 elements) to justify low- and high-frequency beam co-alignment. The transmit beam profiles were studied as a surrogate measure of receive spatial sensitivity co-alignment as justified by the principle of reciprocity. We measured the beam profiles along the x and y direction in immersion for the low- and high-frequency CMUTs to verify that the beam profiles were co-aligned. A 7×7 mm single-element die was mounted and wirebonded onto a CFP80 package. We mounted this onto a test fixture with attachable tank and filled it with vegetable oil. We used a hydrophone (HNP-0400, Onda) to measure the transmit pressures. The CMUTs were driven by a pulser-receiver (Model 5073PR, Olympus NDT). The energy was 4 µJ, and the pulse repetition frequency was 1 kHz. The receive signal was amplified by a pre-amp (AH-2010-DCBNS, Onda) and 54-dB pulser-receiver amplifier (Model 5900PR, Olympus NDT). The receive signals were measured by an oscilloscope using 100-times averaging. The hydrophone was scanned across the x and y directions at 0.5-mm increments. This was done for each subarray at 5 different depths starting at 1 cm away from the transducer surface and increasing by 0.254 cm (0.1 inches) to 2.27 cm away. This shows that the beam profiles were co-aligned at several depths. The beam profiles are shown in a 3D graph with the z axis representing the height of the hydrophone above the multifrequency transducer. The x and y axis represent the position of the hydrophone along the lateral and elevational directions. The x and y scans for the low- and high-frequency subarrays are shown side-by-side for comparison. The origin is the same for all scans.

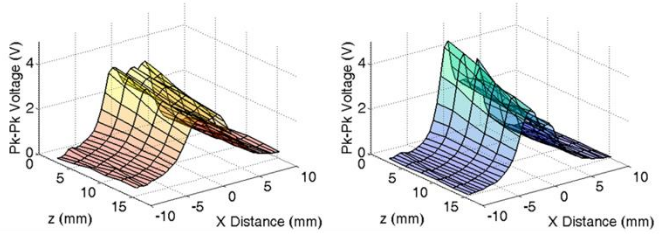

(a) Low Frequency, X Cross-section (b) High Frequency, X Cross-section

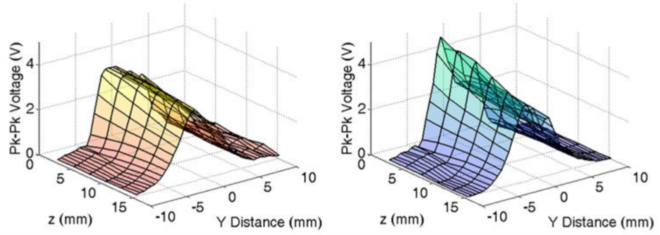

(c) Low Frequency, Y Cross-section (d) High Frequency, Y Cross-section

Figure 5.13. (a) Low-frequency (82 um) beam profile in the x direction, (b) high-frequency (36 um) beam profile in the x direction, (c) low-frequency (82 um) beam profile in the y direction, and (d) high-frequency (36 um) beam profile in the y direction.

Fig. 5.13 (a) and Fig. 5.13 (b) show good co-alignment between low- and high-frequency beams in the x direction at all investigated depths. Fig. 5.13 (c) and Fig. 5.13 (d) show good co-alignment in the y direction at all investigated depths. Some asymmetry is seen in the pressure profiles and is attributed in part to resistive losses in the bottom electrode. In the future, a higher level of doping will be used.

5.5.4 Photoacoustic Imaging

We obtained images using the 82- and 36-μm devices and calculated the lateral resolution. A linear array was scanned linearly to acquire 2D PA images of a hair. Our target phantom was a human hair immersed in oil. The hair phantom was excited via a Nd:YAG laser (Continuum Surelight III, 10-Hz repetition, ~20 mJ/cm^2). Signal from the array was amplified by 40 dB using a pulser-receiver amplifier (Model 5900PR, Olympus NDT) before being acquired by a data acquisition card at a sample rate of 125 MS/s. We biased the 82- and 36-μm devices so that they operated in pre-collapse mode. We scanned the linear arrays over 93 steps with a step size of 235 μm to create a synthetic aperture of 93 active linear array elements, approximately 6.6 mm × 21.9 mm in size. The acquired data was then dynamically focused using MATLAB (MathWorks Inc.) to create a 2D PA image.

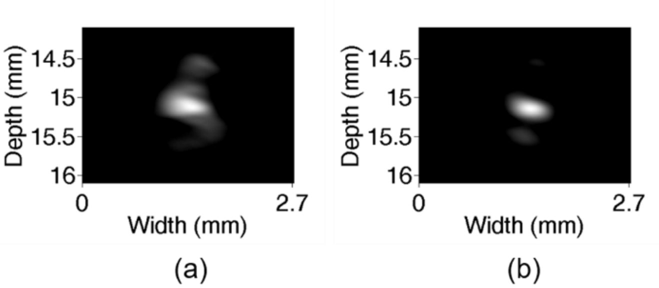

Figure 5.14. (a) PA image from 82-µm devices and (b) PA image from 36-µm devices.

Fig. 5.14 (a) and (b) shows a 2D cross section of a hair obtained using both the 82- and 36-µm devices, respectively. There are sidelobes present in Fig. 5.14 (a) and (b), but they are not visible with the current colormap. We did not use apodizaton during image reconstruction. We obtain the lateral resolution from the full width at half maximum. The lateral resolution for the 82- and 36-µm devices was 673 µm and 492 µm, respectively.

The equation for the theoretical lateral resolution is $\text{lateral resolution} \approx 1.4 f_{\#}\lambda$ where λ is the wavelength and $f_{\#}$ is the f-number. Using a speed of sound in oil of 1430 m/s and with the active aperture limited to give an $f_{\#} \sim 1$ during beamforming, the theoretical lateral resolution for the 82- and 36-µm devices is 1151 µm and 397 µm, respectively. When considering the hair width is ~100 µm, the theoretical lateral resolution for the 360-µm device is comparable to the measured value of 492 µm. For the 82-µm devices, the measured lateral resolution is narrower than the predicted theoretical value. Further device modelling may be required to explain the difference between theoretical and measured lateral resolutions in the 82-µm devices.

5.5.5 Spectroscopic Photoacoustic Imaging

To demonstrate the feasibility of obtaining sPA images of diffuse dye concentrations overlaid on high-resolution images of vasculature, we used two phantom targets, a hair as a small optical absorber mimicking a microvessel and thick dental floss dyed with 0.3% solution of methylene blue (MB) as a large target mimicking a diffuse optical reporter distribution. The term melanin (MEL) is used interchangeably with hair because melanin is the optical absorber in hair. We immersed the phantoms in oil. The hair was roughly 100 µm in diameter versus the dyed floss, which was roughly 1 mm in diameter. The phantoms were excited via a Nd:YAG laser (Continuum Surelight ND6000, 10-Hz repetition, ~20 mJ/cm^2). Signal from the array was amplified by 54 dB before being acquired by a data acquisition card at a sample rate of 125 MS/s. We biased the 82- and 36-µm devices so that they operated in pre-collapse mode. We scanned the linear arrays over 99 steps with a step size of 250 µm to create a synthetic aperture of 99 active linear array elements, approximately 6.6 mm × 24.8 mm in size. The acquired data was then dynamically focused using MATLAB (MathWorks Inc.) to create a 2D PA image. We obtained PA images at optical wavelengths (λ) of 615 nm and 665 nm. The relative absorption coefficients were found using the peak image intensity of the methylene blue and hair in the 615- and 665-nm images. Spectral demixing was done using MATLAB. The problem has previously been described in detail [15]. PA intensity is proportional to the absorption coefficient, which is proportional to the sum of extinction coefficient multiplied by concentration. If we take two PA images at different wavelengths, we will have two equations with different values for extinction and absorption coefficients. Given that we have two unknown concentrations, we will be able to solve these equations for the two unknowns.

Table 5.1 shows a comparison of the PA signal-to-noise ratio (SNR) of the melanin and methylene blue targets obtained from the low- and high-frequency subarrays at 615-nm and 665-nm laser wavelengths. We measured the signal amplitude as the average amplitude contained in circular masks that were similar in size to the actual targets. Table 1 shows that the low-frequency subarrays have higher SNRs for the larger methylene blue target (+12.45-dB average improvement) and the smaller hair target (+2.85-dB average improvement). We indicate the difference in SNR in red. This validates our earlier simulation showing that larger target have lower-frequency PA signal content. The 12.45-dB improvement in SNR using the low-frequency subarrays is greater than the 6-dB improvement that we would expected by using a single-frequency transducer composed of only the high-frequency subarrays.

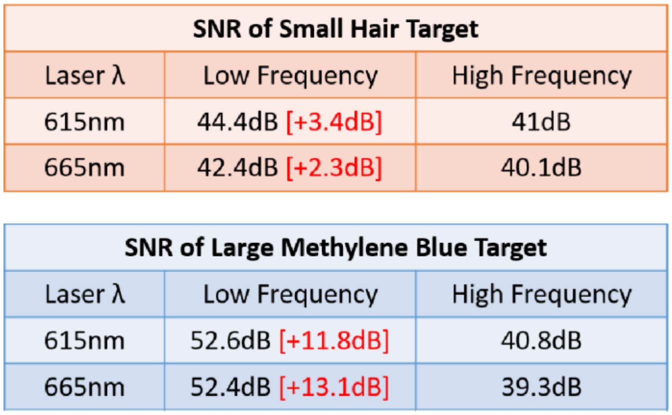

SNR of Small Hair Target

Laser λ	Low Frequency	High Frequency
615nm	44.4dB [+3.4dB]	41dB
665nm	42.4dB [+2.3dB]	40.1dB

SNR of Large Methylene Blue Target

Laser λ	Low Frequency	High Frequency
615nm	52.6dB [+11.8dB]	40.8dB
665nm	52.4dB [+13.1dB]	39.3dB

Table 5.1. PA SNR comparison between the low-frequency subarrays and the high-frequency subarrays for the hair and methylene blue targets at 615- and 665-nm laser wavelengths. Red indicates the SNR difference.

Fig. 5.15 (a) illustrates the sPA image of methylene blue concentration and melanin concentration using the low-frequency devices. Fig. 5.15 (b) illustrates the sPA image of methylene blue concentration and melanin concentration using the high-frequency devices. Fig. 5.15 (c) shows the low-frequency higher amplitude sPA image of methylene blue concentration overlaid on the high-frequency higher resolution sPA image of melanin concentration (microvessel phantom).

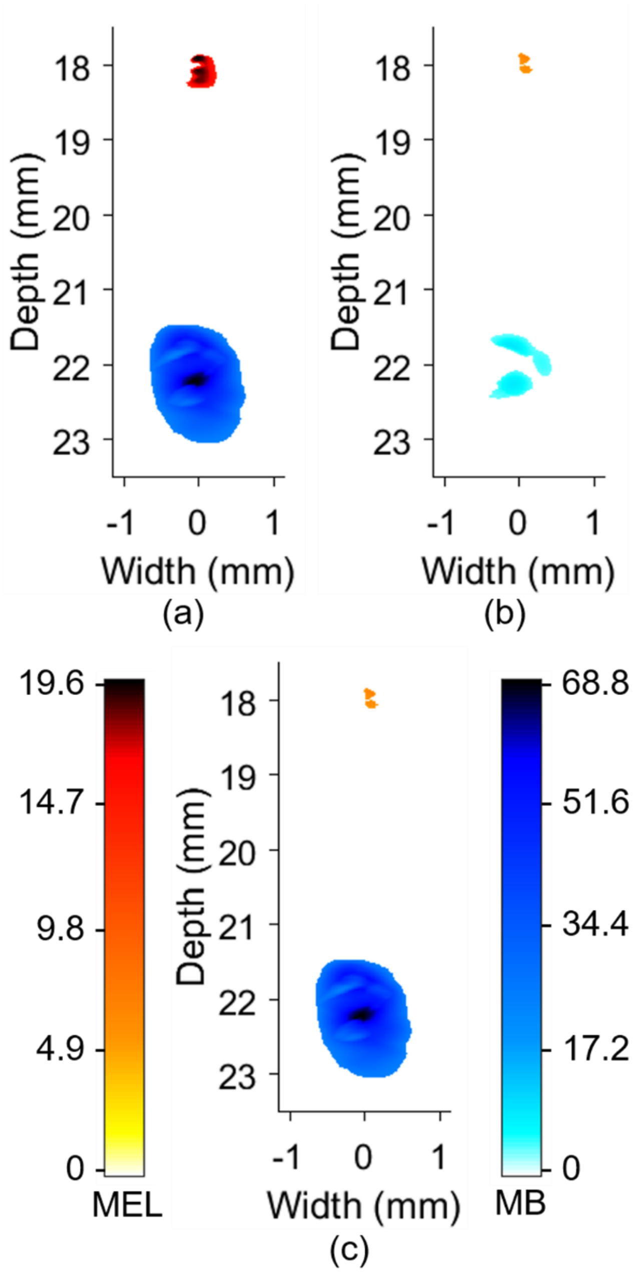

Figure 5.15. (a) sPA image of methylene blue and melanin concentration using 82-um devices (low frequency), (b) sPA image of methylene blue and melanin concentration using 36-um devices (high frequency), and (c) low-frequency sPA image of methylene blue concentration (higher intensity, lower resolution) overlaid on high-frequency sPA image of melanin concentration (higher resolution). [Left: Melanin (MEL) concentration colormap, Right: Methylene blue (MB) concentration colormap]

Table 5.2 shows a comparison of the sPA SNR of the melanin and methylene blue targets obtained from the low- and high-frequency subarrays. Similar to before, we measured the signal amplitude as the average amplitude contained in circular masks that were similar in size to the actual targets. Table 5.2 shows that the low-frequency subarrays have higher SNRs for the larger methylene blue target (+17.3-dB improvement) and the smaller hair target (+9.3-dB improvement) compared to the high frequency subarrays. We indicate the difference in SNR between low- and high-frequency subarrays in red. The 17.3-dB improvement in SNR using the low-frequency subarrays is greater than the 6-dB improvement that we would expected by using a single-frequency transducer composed of only the high-frequency subarrays.

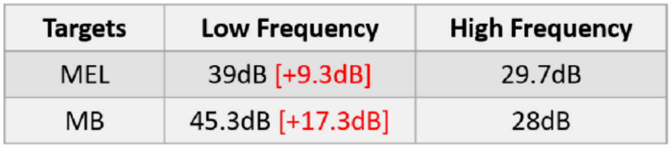

Targets	Low Frequency	High Frequency
MEL	39dB [+9.3dB]	29.7dB
MB	45.3dB [+17.3dB]	28dB

Table 5.2. sPA SNR comparison between the low-frequency subarrays and the high-frequency subarrays for the hair and methylene blue targets. Red indicates the SNR difference.

We want to show that having the low-frequency subarrays offers the opportunity to better visualize diffuse dye distributions while still being able to produce high-resolution images using the high-frequency subarray. One question is whether the low-frequency subarray offers improved visualization and SNR over the high-frequency subarray for visualizing diffuse dye targets. A second question is whether the low-frequency subarray provides SNR greater than what would be possible with a high-frequency array occupying all the active area of the transducer.

To answer the first question, we compare SNR of single targets between high- and low-frequency subarrays and show the low-frequency subarray offers an average 13.1-dB SNR improvement for 665-nm wavelength illumination over the high-frequency subarray for the larger methylene blue target. We also do a similar comparison at 615 nm. For these comparisons, the only factor that is changed is whether we use the low- or high-frequency subarray. We also form spectrally demixed images and compare the SNR of the demixed images between high- and low-frequency subarrays. In this case, we found a 17.3-dB improvement using the low-frequency subarray compared to the high-frequency subarrays. To answer the second question, consider that if the high-frequency subarray were to occupy the whole transducer active area, we would anticipate an additional 6-dB improvement in SNR. Our measured low-frequency subarray sensitivities are still greater. Thus, the low-frequency subarrays provide even higher sensitivity to the diffuse dye target than a fully-populated high-frequency array.

Note that the electromechanical sensitivities and active areas of the low- and high-frequency subarrays are designed to be close but may be different. However, this does not matter for the intended purpose. We could add even more active area to the low-frequency devices to improve sensitivity to diffuse dye distributions at the expense of sensitivity to high-resolution information.

5.6 Discussion

The fabrication process used to make these multifrequency devices has the potential for high-throughput manufacturing. This can be accredited to the use of etch-stops for each etching process, high-selectivity sacrificial-release etching, and ICP-DRIE etch-rates as fast as 32 nm/s. Additionally, the interlacing of different-frequency CMUTs is determined simply by the lithography mask design, making this process no more difficult than fabricating single-frequency arrays. This is in sharp contrast with piezoelectric fabrication technology that is limited because of the need to interlace piezoceramics of different thicknesses, which is a great deal harder than fabricating single-frequency arrays.

A potential disadvantage of the interlacing method is the reduced sensitivities of each frequency component. Reduced sensitivity results from the area for each frequency device being halved from sharing real-estate between interlaced low- and high-frequency elements. There is a potential for nonlinear coupling between low- and high-frequency devices due to mutual acoustic interaction, including higher-order modes of the low-frequency devices interacting with higher-frequency elements and vice versa. Electrical and acoustic crosstalk should be further investigated in future work. In the present paper, we read out signal from each subarray one at a time while the other is grounded so electrical crosstalk is principally avoided. Ongoing work is focused on modelling mutual acoustic impedance between large and small elements to further investigate acoustic crosstalk.

Section 5.5.5 of the experiment section shows the improved wideband detection of both low- and high-frequency PA signal with our multifrequency CMUTs. However, another more direct experiment could have been performed by having a single target type of varying size placed at the same depth location to allow better comparison between detection of low- and high-frequency PA signals with each subarray. The advantage of the experiment we chose to perform is that it more closely simulates a practical application where a diffuse optical dye is present in vasculature.

We have demonstrated that the frequency of PA signals is in part determined by absorber distribution and geometry, which may cause problems when trying to image large slowly-varying distributions such as diffuse optical dyes in the presence of surrounding vasculature. While we have focused on using multi-band CMUTs for wideband sPA imaging, multifrequency CMUTs would prove equally useful in single-wavelength wideband PA imaging.

In future work, in vivo imaging of diffuse dye or reporter distributions could be spectroscopically imaged with the low-frequency sub-aperture for high-sensitivity, and the spectroscopically-separated microvasculature and tissue structure could be rendered using data from the high-frequency sub-aperture.

5.7 Conclusion

Our multifrequency interlaced CMUTs consist of interlaced low-frequency (82-μm membrane) and high-frequency (36-μm membrane) cells. We have developed multifrequency interlaced CMUTs with optimal beam co-alignment, imaging resolution, and minimal grating lobes by interlacing cells on a scale smaller than the shortest operational wavelength. Our multifrequency interlaced CMUTs are better able to detect wideband PA signal content. We have demonstrated the potential of our multifrequency CMUTs to produce high-resolution images of vasculature using the high-frequency subarrays while better visualizing large slowly-varying contrast agent distributions with higher SNR using the low-frequency subarrays. This work represents the first application of our interlaced multifrequency CMUTs for PA and sPA imaging. Multi-band CMUTs may offer a new paradigm for molecular imaging.

References

1. J. L. Su, B. Wang, K. E. Wilson, C. L. Bayer, Y. Chen, S. Kim, K. A. Homan, and S. Y. Emelianov, "Advances in clinical and biomedical applications of photoacoustic imaging," Expert opinion on medical diagnostics **4,** 497-510 (2010).

2. V. S. Dogra, B. K. Chinni, K. S. Valluru, J. V. Joseph, A. Ghazi, J. L. Yao, K. Evans, E. M. Messing, and N. A. Rao, "Multispectral Photoacoustic Imaging of Prostate Cancer: Preliminary Ex-vivo Results," J. Clin. Imaging Sci. **3,** 41-7514.119139. eCollection 2013 (2013).

3. M. Mehrmohammadi, S. Joon Yoon, D. Yeager, and S. Y Emelianov, "Photoacoustic imaging for cancer detection and staging," Current molecular imaging **2,** 89-105 (2013).

4. S. Sethuraman, J. H. Amirian, S. H. Litovsky, R. W. Smalling, and S. Y. Emelianov, "Spectroscopic intravascular photoacoustic imaging to differentiate atherosclerotic plaques," Optics express **16,** 3362-3367 (2008).

5. K. Jansen, Van Der Steen, Antonius FW, H. M. van Beusekom, J. W. Oosterhuis, and G. van Soest, "Intravascular photoacoustic imaging of human coronary atherosclerosis," Opt. Lett. **36,** 597-599 (2011).

6. B. Wang, A. Karpiouk, D. Yeager, J. Amirian, S. Litovsky, R. Smalling, and S. Emelianov, "In vivo intravascular ultrasound-guided photoacoustic imaging of lipid in plaques using an animal model of atherosclerosis," Ultrasound Med. Biol. **38,** 2098-2103 (2012).

7. G. S. Filonov, A. Krumholz, J. Xia, J. Yao, L. V. Wang, and V. V. Verkhusha, "Deep-Tissue Photoacoustic Tomography of a Genetically Encoded Near-Infrared Fluorescent Probe," Angewandte Chemie International Edition **51,** 1448-1451 (2012).

8. A. Krumholz, D. M. Shcherbakova, J. Xia, L. V. Wang, and V. V. Verkhusha, "Multicontrast photoacoustic in vivo imaging using near-infrared fluorescent proteins," Scientific reports **4,** 3939 (2014).

9. L. Li, R. J. Zemp, G. F. Lungu, G. Stoica, and L. V. Wang, "Photoacoustic imaging of lacZ gene expression in vivo," J. Biomed. Opt. **12,** 020504 (2007).

10. A. Agarwal, S. Huang, M. O'donnell, K. Day, M. Day, N. Kotov, and S. Ashkenazi, "Targeted gold nanorod contrast agent for prostate cancer detection by photoacoustic imaging," J. Appl. Phys. **102,** 064701 (2007).

11. S. Mallidi, T. Larson, J. Tam, P. P. Joshi, A. Karpiouk, K. Sokolov, and S. Emelianov, "Multiwavelength photoacoustic imaging and plasmon resonance coupling of gold nanoparticles for selective detection of cancer," Nano letters **9,** 2825-2831 (2009).

12. S. Mallidi, T. Larson, J. Aaron, K. Sokolov, and S. Emelianov, "Molecular specific optoacoustic imaging with plasmonic nanoparticles," Optics Express **15,** 6583-6588 (2007).

13. K. A. Homan, M. Souza, R. Truby, G. P. Luke, C. Green, E. Vreeland, and S. Emelianov, "Silver nanoplate contrast agents for in vivo molecular photoacoustic imaging," ACS nano **6,** 641-650 (2012).

14. C. Xu, P. D. Kumavor, U. S. Alqasemi, H. Li, Y. Xu, S. Zanganeh, and Q. Zhu, "Indocyanine green enhanced co-registered diffuse optical tomography and photoacoustic tomography," J. Biomed. Opt. **18,** 126006 (2013).

15. B. T. Cox, J. G. Laufer, P. C. Beard, and S. R. Arridge, "Quantitative spectroscopic photoacoustic imaging: a review," J. Biomed. Opt. **17,** 061202 (2012).

16. G. P. Luke, S. Y. Nam, and S. Y. Emelianov, "Optical wavelength selection for improved spectroscopic photoacoustic imaging," Photoacoustics **1,** 36-42 (2013).

17. K. E. Wilson, S. V. Bachawal, L. Tian, and J. K. Willmann, "Multiparametric spectroscopic photoacoustic imaging of breast cancer development in a transgenic mouse model," Theranostics **4,** 1062-1071 (2014).

18. K. Jansen, van der Steen, Antonius FW, M. Wu, H. M. van Beusekom, G. Springeling, X. Li, Q. Zhou, K. K. Shung, D. P. de Kleijn, and G. van Soest, "Spectroscopic intravascular photoacoustic imaging of lipids in atherosclerosis," J. Biomed. Opt. **19,** 026006 (2014).

19. G. J. Diebold, M. I. Khan, and S. M. Park, "Photoacoustic "signatures" of particulate matter: optical production of acoustic monopole radiation," Science **250,** 101-104 (1990).

20. G. Ku, X. Wang, G. Stoica, and L. V. Wang, "Multiple-bandwidth photoacoustic tomography," Physics in Medicine & Biology **49,** 1329 (2004).

21. D. N. Stephens, D. E. Kruse, A. S. Ergun, S. Barnes, X. M. Lu, and K. W. Ferrara, "Efficient array design for sonotherapy," Physics in Medicine & Biology **53,** 3943 (2008).

22. T. Azuma, M. Ogihara, J. Kubota, A. Sasaki, S. Umemura, and H. Furuhata, "Dual-frequency ultrasound imaging and therapeutic bilaminar array using frequency selective isolation layer," IEEE Trans. Ultrason. Ferroelectr. Freq. Control **57,** 1211-1224 (2010).

23. J. Ma, K. H. Martin, P. A. Dayton, and X. Jiang, "A preliminary engineering design of intravascular dual-frequency transducers for contrast-enhanced acoustic angiography and molecular imaging," IEEE Trans. Ultrason. Ferroelectr. Freq. Control **61,** 870-880 (2014).

24. R. C. Gessner, C. B. Frederick, F. S. Foster, and P. A. Dayton, "Acoustic angiography: a new imaging modality for assessing microvasculature architecture," Journal of Biomedical Imaging **2013,** 14 (2013).

25. R. Gessner, M. Lukacs, M. Lee, E. Cherin, F. S. Foster, and P. A. Dayton, "High-resolution, high-contrast ultrasound imaging using a prototype dual-frequency transducer: in vitro and in vivo studies," IEEE Trans. Ultrason. Ferroelectr. Freq. Control **57,** 1772-1781 (2010).

26. A. Guiroy, A. Novell, E. Ringgaard, R. Lou-Moeller, J. Gregoire, A. Abellard, T. Zawada, A. Bouakaz, and F. Levassort, "Dual-frequency transducer for nonlinear contrast agent imaging," IEEE Trans. Ultrason. Ferroelectr. Freq. Control **60,** 2634-2644 (2013).

27. S. Vaithilingam, T. Ma, Y. Furukawa, I. O. Wygant, X. Zhuang, A. De La Zerda, O. Oralkan, A. Kamaya, R. B. Jeffrey, and B. T. Khuri-yakub, "Three-dimensional photoacoustic imaging using a two-dimensional CMUT array," IEEE Trans. Ultrason. Ferroelectr. Freq. Control **56,** 2411-2419 (2009).

28. S. Kothapalli, T. Ma, S. Vaithilingam, Ö Oralkan, B. T. Khuri-Yakub, and S. S. Gambhir, "Deep tissue photoacoustic imaging using a miniaturized 2-D capacitive micromachined ultrasonic transducer array," IEEE Transactions on Biomedical Engineering **59,** 1199-1204 (2012).

29. R. K. Chee, A. Sampaleanu, D. Rishi, and R. J. Zemp, "Top orthogonal to bottom electrode (TOBE) 2-D CMUT arrays for 3-D photoacoustic imaging," IEEE Trans. Ultrason. Ferroelectr. Freq. Control **61,** 1393-1395 (2014).

30. X. Cheng, J. Chen, and C. Li, "A miniature capacitive micromachined ultrasonic transducer array for minimally invasive photoacoustic imaging," J Microelectromech Syst **19,** 1002-1011 (2010).

31. M. Kupnik, M. Ho, S. Vaithilingam, and B. T. Khuri-Yakub, "CMUTs for air coupled ultrasound with improved bandwidth," in *Ultrasonics Symposium (IUS), 2011 IEEE International,* Anonymous (IEEE, 2011), pp. 592-595.

32. C. Bayram, S. Olcum, M. N. Senlik, and A. Atalar, "Bandwidth improvement in a cMUT array with mixed sized elements," in *Ultrasonics Symposium, 2005 IEEE,* Anonymous (IEEE, 2005), pp. 1956-1959.

33. S. Olcum, A. Atalar, H. Koymen, and M. N. Senlik, "P3R-4 stagger tuned cMUT array for wideband airborne applications," in *Ultrasonics Symposium, 2006. IEEE,* Anonymous (IEEE, 2006), pp. 2377-2380.

34. M. D. Eames, T. J. Reck, and J. A. Hossack, "Selectable frequency CMUT with membrane stand-off structures," in *Ultrasonics Symposium (IUS), 2009 IEEE International,* Anonymous (IEEE, 2009), pp. 2814-2817.

35. M. D. Eames, T. J. Reck, J. P. Kilroy, and J. A. Hossack, "FEA modeling of CMUT with membrane stand-off structures to enable selectable frequency-mode operation," IEEE Trans. Ultrason. Ferroelectr. Freq. Control **58,** (2011).

36. P. Zhang, W. Zheng, W. Moussa, and R. J. Zemp, "CMUTs with interlaced high-and low-frequency elements," in *Ultrasonics Symposium (IUS), 2011 IEEE International,* Anonymous (IEEE, 2011), pp. 116-119.

37. L. V. Wang and H. Wu, *Biomedical optics: principles and imaging* (John Wiley & Sons, 2012).

38. J. A. Jensen, "Field: A program for simulating ultrasound systems," in *10TH NORDICBALTIC CONFERENCE ON BIOMEDICAL IMAGING, VOL. 4, SUPPLEMENT 1, PART 1: 351--353,* Anonymous (Citeseer, 1996).

39. J. A. Jensen and N. B. Svendsen, "Calculation of pressure fields from arbitrarily shaped, apodized, and excited ultrasound transducers," IEEE Trans. Ultrason. Ferroelectr. Freq. Control **39,** 262-267 (1992).

6. In Vivo Multiplexed Photoacoustic Molecular Imaging with Far-Red Photoswitchable Chromoproteins

6.1 Introduction

Molecular contrast agents are providing scientists with a deeper understanding of biological processes by allowing us to target and image important biological markers in the body [1, 2]. Molecular imaging has promising applications in drug development [3, 4], oncology [5, 6], neurobiology [7], and clinical medicine [2, 8]. There are various imaging modalities capable of molecular imaging including X-ray computed tomography (CT), magnetic resonance imaging (MRI), positron emission tomography (PET), fluorescence imaging, optical coherence tomography, ultrasound imaging, and photoacoustic (PA) imaging. Each have their own set of molecular contrast agents such as fluorine-18-labeled fluorodeoxyglucose for PET [9, 10], Gadolinium agents for MRI [2], Cy5.5 for fluorescence imaging [9], and nanoparticles for PA imaging [11-15].

Among molecular probes, genetically-encoded reporters are especially powerful because they can be expressed by the cells of a subject and thereby enable clear visualization of biochemistry and gene expression profiles in living subjects [16-18]. Genetically-encoded reporters have been developed for both PA and fluorescence imaging, making these especially promising molecular imaging modalities. An example of a genetically-encoded reporter is the green fluorescent protein and its variants, which have had a significant impact on biological research [19]. PA and fluorescent genetically-encoded reporters are closely related. Both require strong optical absorption, but PA reporters preferably have lower quantum yields. In fact, PA proteins have been engineered from fluorescent proteins by reducing the quantum yield to generate greater PA signals [20]. Both PA and fluorescent proteins come in a variety of absorption spectrum ranges [19, 21, 22]. Molecular contrast agents with far-red and near-infrared (NIR) absorption spectra are especially valuable because far-red and NIR light have the deepest penetration in tissue allowing deeper in vivo images [23-25].

PA imaging uses laser stimulation to induce thermoelastic expansion resulting in the release of PA signals which can be detected via an ultrasound (US) transducer. PA imaging can image several centimeters deep in vivo in real-time with resolutions higher than other imaging methods at that depth. This is significantly better than fluorescence imaging, which has difficulty obtaining high-resolution images at depths greater than about 1 mm in tissue. The combination of resolution, depth, and imaging rate makes PA imaging a potentially invaluable imaging modality for longitudinal imaging studies involving small animals. With the help of molecular contrast agents, PA imaging may be further enhanced by molecular specificity, allowing a look into biological processes in vivo. The applications of PA molecular imaging include studies of drug response, cancer development, gene activities, and disease biomarkers [26, 27].

One of the limitations of PA molecular imaging is its poor sensitivity in vivo. High blood background signals prevents sensitive detection of molecular PA contrast agents. Recently, Yao et al developed a reversibly photoswitchable chromoprotein (BphP1) for the reduction of the high background blood signal [28]. The idea of a reversibly switchable proteins for background signal reduction had been previously proposed for fluorescence imaging [29, 30]. Photoswitchable chromoproteins can reversibly switch between two optical absorption states. Subtracting images taken in each absorption state can result in a difference image that shows the change in intensity of the photoswitchable reporter while removing the unchanged background signals. This has resulted in significant PA contrast-to-noise ratio (CNR) improvements in vivo. While this is a significant step forward for molecular PA sensitivity, single reporter imaging is not sufficient for addressing modern molecular imaging needs.

In reality, molecular processes are complex interactions involving multiple targets of interest. Thus, a single molecular reporter is insufficient to capture the complexity of most biological processes. Multiplexed imaging capabilities are limited in many molecular imaging modalities, but multiplexing will be essential to obtaining meaningful molecular information. For PA imaging, this will require the ability to multiplex multiple photoswitchable chromoproteins using a photoswitching specific demixing technique and several different photoswitchable reporters. In this paper, we address this need by proposing a new method for imaging and differentiating multiple photoswitchable chromproteins in vivo called difference-spectra demixing. In addition, we will introduce and characterize a second photoswitchable chromoprotein, sGPC2. In comparison to traditional PA imaging, multiplexed PA imaging of photoswitchable chromoproteins requires more extensive multi-wavelength capabilities. Thus, we built a custom photoswitching PA imaging system to address these needs.

We summarize our approach to multiplexed PA molecular imaging using distinct photoswitchable chromoproteins as follows. We use a near-infrared pulsed laser to photoswitch one of the molecules (e.g. BphP1) from its far-red natural state to an orange absorption state. A difference image is formed by subtracting PA images before and after photoswitching, which removes the hemoglobin background. A red wavelength laser is used to drive the chromoprotein from its orange state back to its far-red state. Subsequently, a third wavelength is used to photoconvert the second reporter (e.g. sGPC2). Again, a difference image retains the photoswitched reporter while removing signal from background hemoglobin. Note that as more distinct photoswitchable chromoproteins are developed, they may have partially overlapping absorption spectra that prevents photoswitching one without partially photoswitching another in the same image. To mitigate the unwanted crosstalk associated with unintended photoconversion of reporters, we propose a novel spectral demixing approach using photoswitchable difference spectra. Fig. 6.1 illustrates the principles of difference-spectra demixing using images of sGPC2 and BphP1 that have been adapted for clarity. Fig. 6.1 (a) shows a timeline detailing the change in optical absorption states in response to laser stimulation at 760 nm, 608 nm, and 710 nm. Fig. 6.1 (b) shows the current optical absorption states when each PA image is taken. Fig. 6.1 (c) shows the difference images and difference spectra involved in difference-spectra demixing. Fig. 6.1 (d) shows a relative concentration image of sGPC2 and BphP1 obtained via difference-spectra demixing in vivo. In this example, sGPC2 does not change significantly with 760 nm laser pulses and vice versa for BphP1 at 710 nm. However, as more distinct photoswitchable chromoproteins are developed and multiplexed, there will not always exist a wavelength that photoswitches only one of the multiplexed chromoproteins.

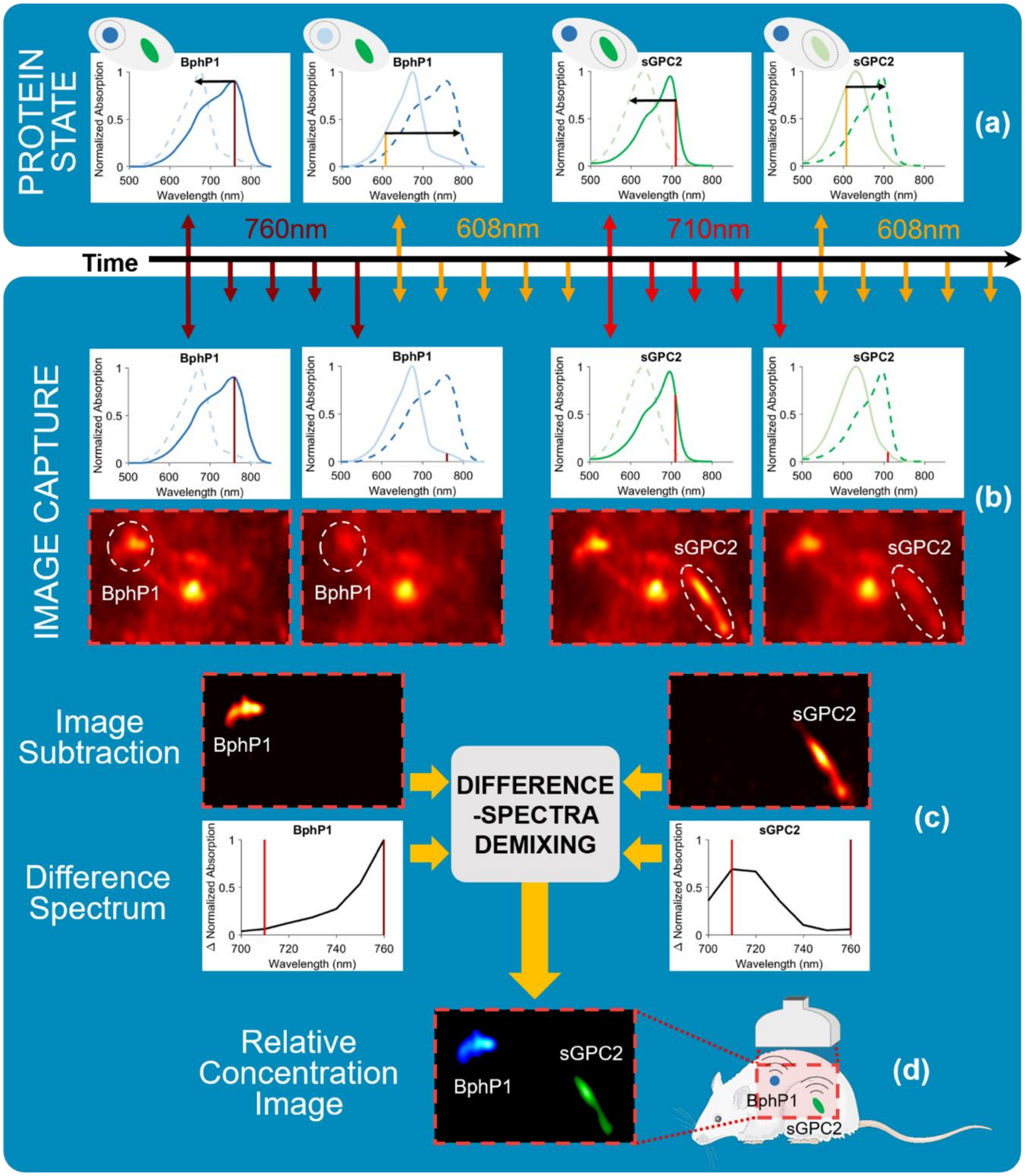

Figure 6.1. Illustration of difference-spectra demixing. The timeline shows an imaging cycle, which consists of a series of laser pulses (wavelengths: 760 nm, 608 nm, 710 nm) separated by 0.1 s. The laser pulses are used to image and photoconvert sGPC2 and BphP1. (a) Illustrates the change in absorption states for sGPC2 and BphP1 following exposure to laser pulses. (b) Shows the PA images obtained during the imaging cycle and the corresponding optical absorption states of sGPC2 and BphP1. (c) Shows the difference images obtained via image subtraction and the experimentally determined difference spectra used in difference-spectra demixing. (d) Shows a relative concentration image of sGPC2 and BphP1 obtained via difference-spectra demixing in vivo. This illustrations shows the simple case involving only 710 nm and 760 nm imaging wavelengths, but in this paper, we will also use 700 nm, 720 nm, 730 nm, 740 nm, and 750 nm wavelengths. [Mouse art from Servier Medical Art (CC by 2.0)]

6.2 Methods

6.2.1 Photoswitching Photoacoustic Setup

We built a custom 3D photoswitching PA imaging system to acquire simultaneous PA and US data with photoconverting and 3D imaging capabilities, Fig. 6.2. This imaging system is capable of both traditional PA imaging as well as photoconversion of reversibly photoswitchable chromoproteins. It employs two Nd:YAG lasers: a Surelite OPO Plus (Continuum, 10 Hz repetition) and a ND6000 (Continuum, 10 Hz repetition). A research US imaging platform (Vantage 256, Verasonics) was used to acquire the PA and US signals. A function generator (AFG 3021B, Tektronix) was used to maintain a 10 Hz laser pulse frequency. The delay function generator (DG645, Stanford Research Systems) controls the triggering of the lasers and signal acquisition card (Octopus, GaGe). The signal acquisition card acquires photodiode (DET100A/M, Thorlabs) signals from the imaging laser for laser intensity normalization. A stepper motor (23Y002D-LW8, Anaheim Automation) translates the PA/US transducer (LZ250, VisualSonics, Fujifilm) linearly to obtain 3D images when desired. The LZ250 transducer has a laser input cable as well as a signal cable, which sends US and PA signals to the Vantage 256. Due to limited PCI slots, the main computer remotely controls a second computer to use the stepper motor. To allow two laser sources to enter the LZ250 laser input for reversible photoconversion, a dichroic mirror (DMLP650, Thorlabs) reflects wavelengths less than 633 nm and transmits wavelengths greater than 685 nm.

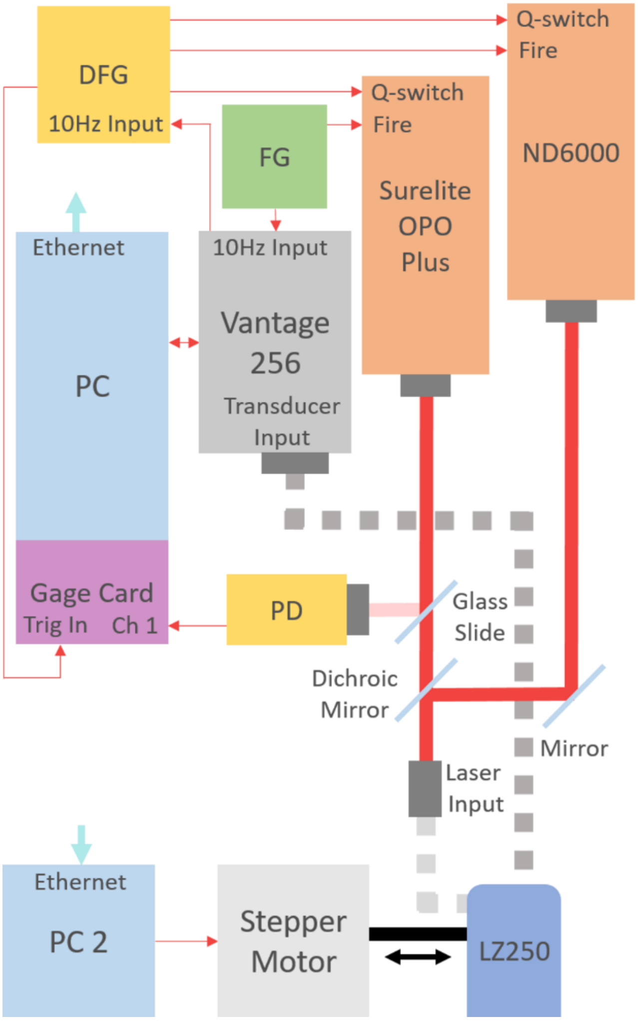

Figure 6.2. Diagram shows the custom photoswitching PA imaging system used to obtain 2D/3D US and PA difference images with reversibly photoswitchable chromoproteins. DFG = delay function generator, FG = function generator, PD = photodiode, PC = personal computer, PC2 = personal computer 2, and Fire = flashlamp trigger.

In the PA experiments requiring photoconversion in this paper, we used the switching cycle shown in Fig. 6.3. The laser pulses at a 10 Hz repetition rate. 608 nm wavelength light converts the chromoproteins from the orange state to the far-red state in the first half of the imaging cycle. Image acquisition occurs at a 10 Hz rate in the second half of the imaging cycle using 700+ nm wavelength light, which simultaneously photoconverts the chromoprotein from the far-red state back to the orange state. Difference images result from subtracting the final image from the first. This custom imaging system has acquired difference image data at a rate of 1 frame per second, which is 32-times faster than previously reported photoswitching PA imaging speeds [28].

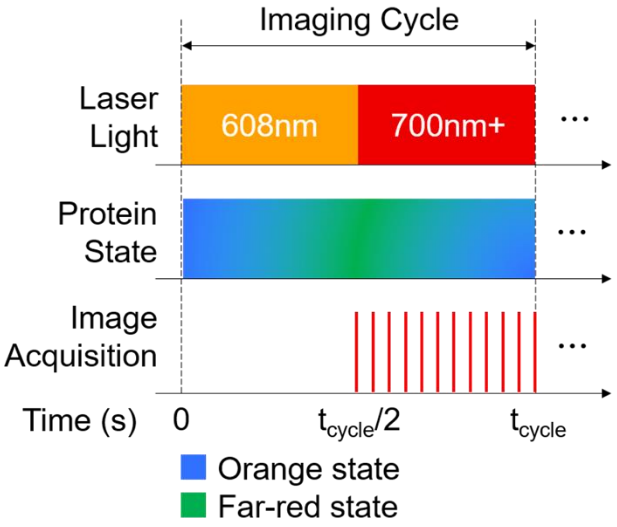

Figure 6.3. A single imaging cycle for imaging reversibly switchable chromoproteins.

6.2.2 sGPC2 Development

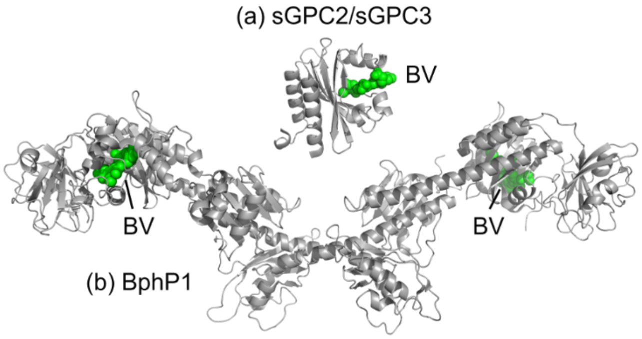

Figure 6.4. Molecular models of sGPC2/sGPC3 and BphP1. (a) The x-ray crystal structure for AnPixJg2 (PDB ID 3W2Z) *[31]* is used here to represent sGPC2/sGPC3. (b) The x-ray crystal structure for BphP1-70 (PDB ID 4GW9) *[32]* is used to represent BphP1. The biliverdin chromophore (BV), responsible for the protein's color and photochromic properties, is represented with green spheres.

We have thus far referred mostly to sGPC2, but we did also develop a second photoswitchable chromoprotein sGPC3 with very similar optical properties. sGPC2 and sGPC3 were engineered from the biliverdin-binding second GAF domain (AM1_1557g2, residues ~220 – 364) of the cyanobacteriochrome of *Acaryochloris marina* MBIC11017 cyanobacteria [33]. This protein domain undergoes reversible photoswitching between a far-red (absorbance maximum ~692 nm) and an orange state (absorbance maximum ~620 nm) [33]. Starting with a variant known as GAF2 that was optimized for brighter fluorescence (AM1_1557g2 with mutations I10N, I13T, R24G, V147E, and Q165L), we performed 8 additional iterative rounds of directed evolution involving library generation by error-prone PCR and visual inspection of bacterial colonies on plates to identify the most brightly colored colonies. The most colored colonies were cultured overnight, and the variants demonstrating reversible photoswitchability and the highest absorbance at ~692 nm were used as the template for subsequent rounds. We removed regions of the protein that we suspected of being required for dimerization. Fig. 6.4 shows models of sGPC2/sGPC3 and BphP1 at equivalent scaling. As these models reveal, the monomeric sGPC2 and sGPC3 are just one-tenth the size of the dimeric BphP1 protein.

6.2.2.1 General Methods and Materials

All synthetic DNA oligonucleotides used for cloning and library construction were purchased from Integrated DNA Technologies (Coralville, IA). Minipreparation of plasmid DNA using the GeneJET plasmid miniprep kit (Thermo Fisher Scientific), polymerase chain reactions (PCR), restriction enzyme digestion, ligation, and agarose gel electrophoresis were performed according to Sambrook et al [34]. *Pfu* DNA polymerase was obtained from Thermo Fisher Scientific and used for standard PCR. *Taq* DNA polymerase was purchased from New England Biolabs and used for error-prone PCR. All restriction enzymes were obtained from Thermo Fisher Scientific or New England Biolabs. T4 DNA ligase was obtained from Thermo Fisher Scientific. PCR and digestion products were purified with the GeneJET gel extraction kit (Thermo Fisher Scientific) according to the manufacturer's instructions. All sequencing was performed at University of Alberta Molecular Biology Service Unit (MBSU) or the University Core DNA Services at University of Calgary.

6.2.2.2 Random Mutagenesis and Library Creation

A synthetic gene encoding AM1_1557g2 (Integrated DNA Technologies) was used as the initial template for the construction of genetic libraries. Random mutagenesis was performed by error-prone PCR [35]. Full-length gene libraries were digested with XhoI/HindIII (Thermo Fisher Scientific) and ligated into similarly digested engineered pBAD/His B-HO1 plasmids [36] with T4 DNA ligase (Thermo Fisher Scientific). The gene for heme oxygenase-1 (HO1) is necessary for the production of biliverdin from heme in E. coli bacteria. Plasmid libraries were expressed in E. coli strain DH10B (Thermo Fisher Scientific) on lysogeny broth (LB) agar plates supplemented with 0.1 mg/mL ampicillin and 40 ppm L-arabinose at 37 °C overnight.

6.2.2.3 Absorption and Reversible Photoswitchability Screening

E. coli colonies expressing the sGPC2/sGPC3 libraries were grown on 10 cm Petri dishes. The 30-40 colonies with the darkest color were manually picked into 4 mL LB media, supplemented with 0.1 mg/mL ampicillin and 40ppm L-arabinose and incubated overnight. Crude protein extracts were obtained by lysing cells with B-PER Protein Extraction Reagent (Thermo Fisher Scientific). Absorbance spectra (350-800 nm wavelength scan) of the crude protein extracts were recorded with a DU-800 UV-visible spectrophotometer (Beckman). For photoconversion from the orange to far-red state of sGPC2/sGPC3, orange light was applied by a variable wavelength light source (560/40 nm, 10-15 s). For photoconversion from the far-red to orange state of sGPC2/sGPC3, far-red light was applied using a 730nm LED for 10-15 s. After absorption maximum and photoswitchability comparison, 1-2 improved variants were picked and used as the template for the next round of random mutagenesis and library generation.

6.2.2.4 Monomerization

To remove regions of the protein that we suspected of being necessary for dimerization, we genetically deleted 19 residues from the N-terminus and 16 from the C-terminus of the protein. Analysis of protein size with native PAGE confirmed that these deletions did convert the protein from a dimeric to a monomeric state (Fig. 6.5). We also created and screened 13 libraries in which specific residue positions were fully randomized (NNK codon) to all 20 amino acids. The end results of this directed evolution effort were two monomeric proteins designated sGPC2 and sGPC3. Fig. 6.6 shows the sequence alignment of sGPC2 and sGPC3 with AM1_1557g2.

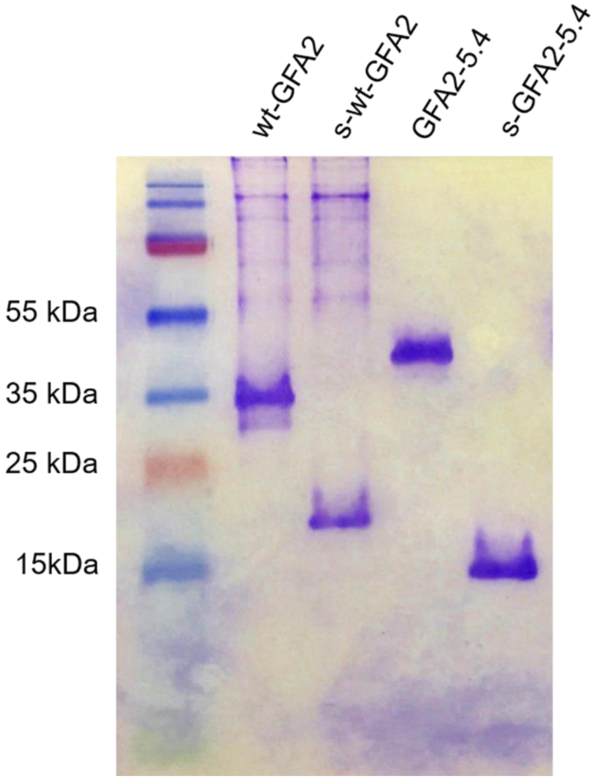

Figure 6.5. Native PAGE analysis comparing non-denatured proteins. Wild type GAF2 (Wt-GAF2) is the initial template; s-wt-GAF2 is wt-GAF2 with truncated N- and C-termini; GAF2-5.4 is a variant from midway during the evolution; and s-GAF2-5.4 is GAF2-5.4 with truncated N- and C-termini.

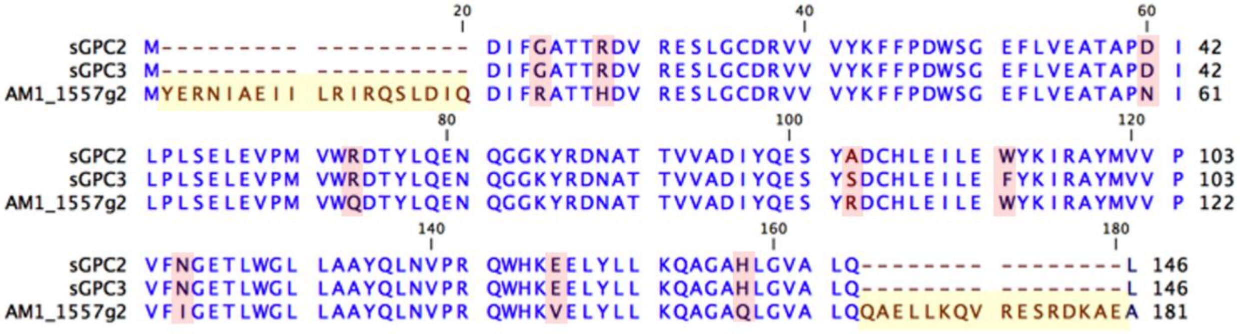

```
                                     20                       40                       60
     sGPC2  M--------- ---------- DIFGATTRDV RESLGCDRVV VYKFFPDWSG EFLVEATAPD I 42
     sGPC3  M--------- ---------- DIFGATTRDV RESLGCDRVV VYKFFPDWSG EFLVEATAPD I 42
AM1_1557g2  MYERNIAEII LRIRQSLDIQ DIFRATTHDV RESLGCDRVV VYKFFPDWSG EFLVEATAPN I 61
                                80                       100                      120
     sGPC2  LPLSELEVPM VWRDTYLQEN QGGKYRDNAT TVVADIYQES YADCHLEILE WYKIRAYMVV P 103
     sGPC3  LPLSELEVPM VWRDTYLQEN QGGKYRDNAT TVVADIYQES YSDCHLEILE FYKIRAYMVV P 103
AM1_1557g2  LPLSELEVPM VWQDTYLQEN QGGKYRDNAT TVVADIYQES YRDCHLEILE WYKIRAYMVV P 122
                                140                      160                      180
     sGPC2  VFNGETLWGL LAAYQLNVPR QWHKEELYLL KQAGAHLGVA LQ-------- --------L 146
     sGPC3  VFNGETLWGL LAAYQLNVPR QWHKEELYLL KQAGAHLGVA LQ-------- --------L 146
AM1_1557g2  VFIGETLWGL LAAYQLNVPR QWHKVELYLL KQAGAQLGVA LQQAELLKQV RESRDKAEA 181
```

Figure 6.6. Sequence alignment of sGPC2, sGPC3, and AM1_1557g2. The yellow highlights are residues we deleted, and the red highlights are mutation positions.

6.2.2.5 Sample Preparation for PA Imaging

E. coli strain ElectroMAX^{TM} DH10B (Invitrogen) was transformed by electroporation with pBAD/His B plasmids containing genes encoding the protein of interest and HO1. A 200 mL culture of LB medium containing 0.1 mg/mL ampicillin and 40 ppm L-arabinose was inoculated with a single colony. This culture was grown in a 500 mL baffled shake flask overnight (225 rev./min, ~24 h) at 37 °C before cells were harvested by centrifugation and resuspended in PBS (pH 7.4).

6.2.3 Difference-Spectra Demixing

Difference-spectra demixing can be used to obtain relative concentrations of reversibly switchable chromoproteins and offers improved differentiation and CNR in comparison to traditional spectral demixing. We describe the methodology in this section using sGPC2 and BphP1.

The PA signal at a location r in vivo with sGPC2 and BphP1 present can be described by $P(r,\lambda,\eta_S,\eta_B) = \Gamma\mu_a(r,\lambda,\eta_S,\eta_B)\Phi(r,\lambda)$ where Γ is the Gruneisen parameter, μ_a is the optical absorption coefficient, Φ is the fluence, λ is the laser wavelength, and $\eta_{S/B}$ are the state of photoconversion for sGPC2/BphP1. $\eta = 0$ represents the protein in its orange state, and $\eta = 1$ represents the protein in its far-red state. The absorption coefficient can be written as

$$(1)\qquad \mu_a(r,\lambda,\eta_S,\eta_B) = \varepsilon_{HbO_2}(\lambda)C_{HbO_2}(r) + \varepsilon_{Hb}(\lambda)C_{Hb}(r) + \varepsilon_{\mathrm{sGPC2}}(\lambda,\eta_S)C_{\mathrm{sGPC2}}(r) + \varepsilon_{BphP1}(\lambda,\eta_B)C_{BphP1}(r)$$

where ε is the extinction coefficient, C is concentration, HbO_2 is oxygenated hemoglobin, and Hb is deoxygenated hemoglobin. For simplicity, we will assume that difference images are taken when sGPC2 and/or BphP1 are completely in either the orange or far-red state. Taking a difference image at λ_1 where sGPC2 is fully photoconverted and BphP1 is not photoconverted, we have $\Delta P_1(r,\lambda_1) = P(r,\lambda_1,\eta_S = 1,\eta_B = 1) - P(r,\lambda_1,\eta_S = 0,\eta_B = 1) = \Gamma\Delta\mu_a(r,\lambda_1)\Phi(r,\lambda_1)$. This equation represents the difference between sGPC2 in its far-red state minus sGPC2 in its orange stage with BphP1 unchanged. The difference in molar extinction coefficients for sGPC2 between the far-red and orange states at wavelength λ_1 can be represented as $\Delta\varepsilon_{\mathrm{sGPC2}}(\lambda_1) = [\varepsilon_{\mathrm{sGPC2}}(\lambda_1, \eta_S = 1) - \varepsilon_{\mathrm{sGPC2}}(\lambda_1, \eta_S = 0)]$. At other wavelengths used for imaging, one or both of the chromoproteins may photoconvert, depending on respective absorption edges. More generally, $\Delta\varepsilon_{\mathrm{sGPC2}}(\lambda_j) = [\varepsilon_{\mathrm{sGPC2}}(\lambda_j, \eta_S(\lambda_j)) - \varepsilon_{\mathrm{sGPC2}}(\lambda_j, \eta_S(\lambda_j))]$. In our experiments, we used the following wavelengths: 700 nm, 710 nm, 720 nm, 730 nm, 740 nm, 750 nm, and 760 nm. Relative values for $\Delta\varepsilon_{\mathrm{sGPC2}}(\lambda_j)$ and $\Delta\varepsilon_{BphP1}(\lambda_j)$ were found experimentally using tube phantoms of E. coli bacteria (100 mg/mL) expressing sGPC2 and BphP1. For a particular wavelength, we obtain the difference image and take the maximum PA signal value in each tube. These experimentally determined difference spectra are shown in Fig. 6.1 (c).

With several of these equations and assuming fluence is approximately wavelength independent, we could solve

$$\begin{bmatrix} \Delta P_1(r, \lambda_1) \\ \vdots \\ \Delta P_N(r, \lambda_N) \end{bmatrix} = \Gamma\Phi(r) \begin{bmatrix} \Delta\varepsilon_{sGPC2}(\lambda_1) & \Delta\varepsilon_{BphP1}(\lambda_1) \\ \vdots & \vdots \\ \Delta\varepsilon_{sGPC2}(\lambda_N) & \Delta\varepsilon_{BphP1}(\lambda_N) \end{bmatrix} \begin{bmatrix} C_{sGPC2}(r) \\ C_{BphP1}(r) \end{bmatrix} \tag{2}$$

for concentrations of sGPC2 and BphP1 for every location r in an image. Simplifying equation (2) to $P = \Delta\varepsilon C$, the solution for concentration can be written as $C = (\Delta\varepsilon)^{-1}P$.

In the case where imaging wavelengths only photoconvert one chromoprotein at a time as is shown in Fig. 6.1, Eq. 2 reduces to the following assuming two chromoproteins and two imaging wavelengths.

$$\begin{bmatrix} \Delta P_1(r, \lambda_1) \\ \Delta P_2(r, \lambda_2) \end{bmatrix} = \Gamma\Phi(r) \begin{bmatrix} \Delta\varepsilon_{sGPC2}(\lambda_1) & 0 \\ 0 & \Delta\varepsilon_{BphP1}(\lambda_2) \end{bmatrix} \begin{bmatrix} C_{sGPC2}(r) \\ C_{BphP1}(r) \end{bmatrix} \tag{3}$$

In this case, the difference images may simply be normalized by their difference molar extinction spectra to produce relative concentration estimates. However, Eq. 2 is more general.

6.3 Results

6.3.1 Characterization

6.3.1.1 Optical Properties

We characterized sGPC2 and sGPC3, and compared them to similar far-red chromoproteins. We summarize the peak absorption wavelength (λ_{ab}), molar extinction coefficients ($\varepsilon_{\mathrm{max}}$), quantum yield (QY), molecular weight (Mw), and oligomeric state for the different chromoproteins in Table 6.1. Overall, we show that sGPC2 and sGPC3 share similar optical properties but have different photoconversion rates. Compared to BphP1 and similar chromoproteins, sGPC2 and sGPC3 have comparable extinction coefficient, lower quantum yield, and much smaller size. The molecular weight of sGPC2 and sGPC3 is 2 to 4.8 times smaller than other chromoproteins with similar photophysical properties. Since sGPC2 and sGPC3 exist as monomers, they are actually one-tenth the size of BphP1. This reduction in size means that there is a lower likelihood that it will interfere with the normal function of a protein partner to which it could be genetically fused.

To determine the quantum yield of chromoproteins, iRFP713 was used as a reference. Briefly, the concentration of a purified protein was adjusted by PBS buffer until absorbance at the excitation wavelength was between 0.2-0.6. A series of dilution of samples and reference with absorbance ranging from 0.01-0.1 were prepared, and the fluorescence spectra were recorded on a QuantaMaster spectrofluorometer (Photon Technology International). Integration of the total fluorescence intensity vs. absorbance was plotted for each sample and reference. Quantum yield could be determined from the slopes of each line.

Protein	**$\lambda_{Ab.**}$ [nm]**	**ε_{max} $\left[\frac{10^3}{M \cdot cm}\right]$ Method**		**QY [%]**	**Mw*** [kDa]**	**Oligomeric State**
		1	**2**			
iRFP	691	105.4	85	5.9	34.6	Dimer
mIFP	683	82	55	8.4	35.1	Monomer
sGPC2*	696	87.2	45.5	0.3	16.8	Monomer
sGPC3*	698	89	41.7	0.2	16.8	Monomer
BphP1*	756	40.4	48.8	0.6	80.3	Dimer

Table 6.1. Comparison of various chromoproteins with far-red absorption spectra [28, 37-39]. ε_{max} is calculated based on BV absorbance in method 1 and protein concentration in method 2. *Designates reversibly photoswitchable chromoproteins. **Far-red absorption peaks in the case of photoswitchable chromoproteins. ***The molecular weight of one chain.

We have also plotted the full absorption spectra of both the orange and far-red states of sGPC2 and sGPC3, Fig. 6.7. Absorption spectra were recorded on a DU-800 UV-visible spectrophotometer (Beckman). Absorption measurements were performed with a 1 cm quartz microcell cuvette. The molar extinction coefficients of BV-binding protein were determined as described by Filonov et al [37] and Shu et al [40]. The absorption spectra of sGPC2 and sGPC3 are similar, as both have orange state and far-red state peaks around 630 nm and 700 nm, respectively. They differ in that sGPC2 has its highest absorption peak in its orange state, while sGPC3 has its highest absorption peak in its far-red state. An experimentally determined difference spectra is used for difference-spectra demixing by taking the peak chromoprotein signal intensities from difference images taken at different wavelengths.

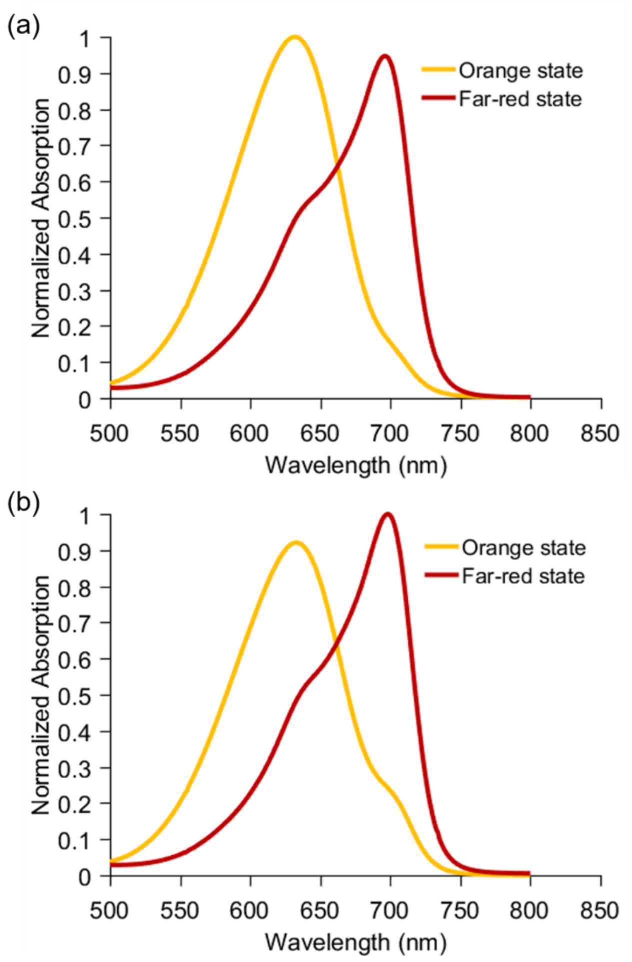

Figure 6.7. Normalized absorption spectrum of (a) sGPC2 and (b) sGPC3.

We compared the photobleaching properties of BphP1 with sGPC2 and sGPC3 by imaging them through 6 photoconversion cycles. We used the photoconversion imaging cycle shown in Fig. 6.3 (t_{cycle} = 40.4 s, 202 pulses per half cycle). We averaged the images acquired from each cycle. We assume photobleaching would affect all images proportionately despite decreasing imaging intensity due to photoconversion. We found that sGPC2 and sGPC3 photobleached 2.8 and 1.5 times faster than BphP1, respectively.

6.3.1.2 Photoconversion Rates

We compared the photoconversion rates of sGPC2, sGPC3, and BphP1. We used the custom PA imaging system shown in Fig. 6.2. PA images of three tubes, submersed in water, containing purified protein samples of sGPC2 (89.53 µM), sGPC3 (133.84 µM), and BphP1 (89.17 µM) were taken at wavelengths near their respective peaks of 710 nm (4.3 mJ/cm^2 fluence) and 780 nm (5.5 mJ/cm^2 fluence) as well as at 730 nm (5.5 mJ/cm^2 fluence). We used the photoconverting imaging cycle shown in Fig. 6.3 (t_{cycle} = 4.4 s, 22 pulses per half cycle) and were able to compare the photoconversion rates of sGPC2, sGPC3, and BphP1 as they were photoconverted back in the second half of the imaging cycle. Fig. 6.8 shows the photoconversion as a function of accumulated fluence (AF) at the wavelengths near their peak absorption wavelength. In those figures, the signal-to-noise ratio (SNR) is in black with the standard error plotted above and below it in red. It is noteworthy that there seems to be some instability in the photoconversion of sGPC2 and sGPC3 at 710 nm. We believe this is due to relatively high levels of absorption by the orange state at 710 nm, which is simultaneously converting some of sGPC2 and sGPC3 back to the far-red state. This seems to be supported by the fact that we found higher photoconversion stability of sGPC2 and sGPC3 when doing the same experiment at 730 nm where there is less absorption by the orange state. A similar instability is seen in BphP1 when the experiment is repeated at 730 nm where there is higher orange state absorption. It is also noteworthy that the dark recovery rate (rate of natural conversion from the orange to far-red state) of sGPC3 is substantially faster than that of sGPC2. However, this does not seem to affect the photoconversion rate at a given fluence.

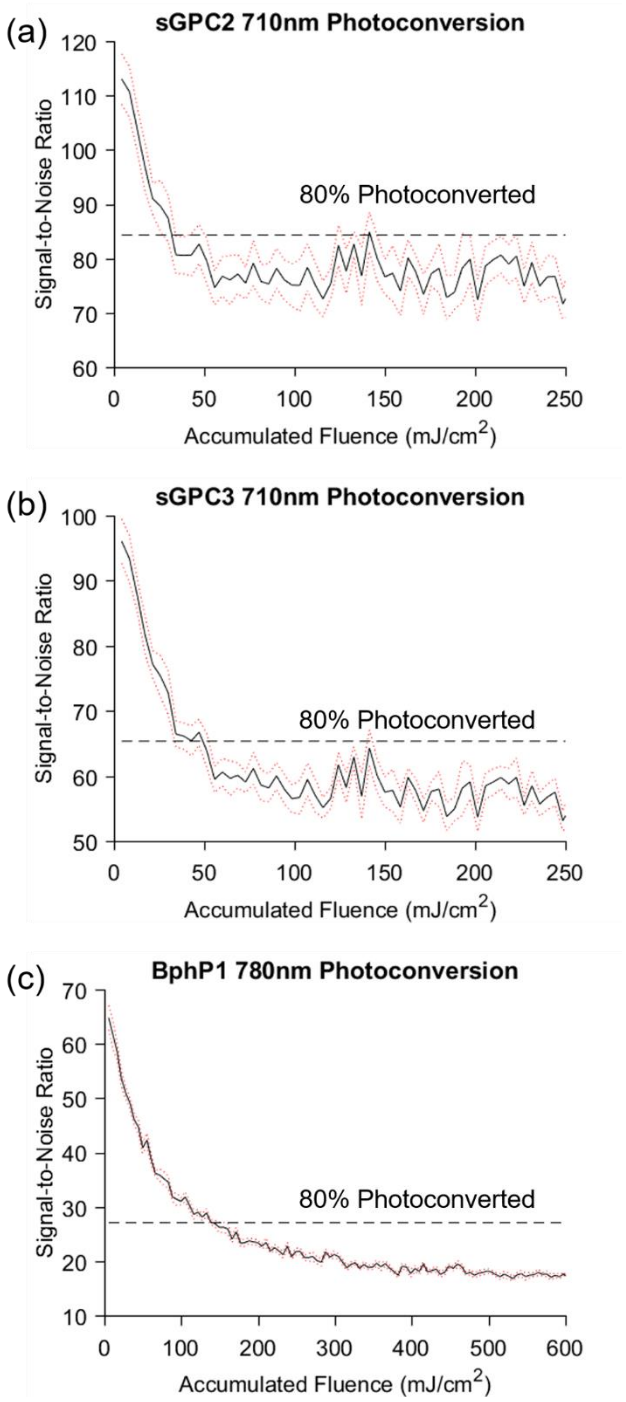

Figure 6.8. Photoconversion rate comparison between (a) sGPC2 at 710 nm, (b) sGPC3 at 710 nm, and (c) BphP1 at 780 nm. Samples are normalized to 100 uM purified protein concentration. The intensity is plotted in black with the standard error in red.

Protein	**80% Photoconverted**		**Photoconversion Rate**	
	ΔSNR	**AF (mJ/cm^2)**	**(ΔSNR per mJ/cm^2)**	**(% per mJ/cm^2)**
sGPC2	28.7	34	0.86	2.4
sGPC3	30.7	49	0.63	1.6
BphP1	37.8	141	0.27	0.6

Table 6.2. Comparison of the change in SNR and photoconversion rate. The comparison of the change in SNR and accumulated fluence is taken at 80% of the fully converted state for sGPC2, sGPC3, and BphP1. Different measures of the photoconversion rates are shown.

Table 6.2 shows the photoconversion rates as well as the change in SNR and accumulated fluence at 80% of the photoconverted state for sGPC2, sGPC3, and BphP1 in Fig. 6.8. The photoconversion rates with respect to percent photoconversion per mJ/cm^2 are 2.4, 1.6, and 0.6 for sGPC2, sGPC3, and BphP1, respectively. The photoconversion rates with respect to change in SNR per mJ/cm^2 are 0.86, 0.63, and 0.27 for sGPC2, sGPC3, and BphP1, respectively. sGPC2 has a 3.2 times faster photoconversion rate than BphP1 when measured by a change in SNR and has a 4 times faster photoconversion rate when measured by photoconversion percentage. This means that at the same fluence, sGPC2 will switch absorption states 4 times as faster than BphP1. BphP1 has the largest change in SNR between photoconverted states at 37.8 in comparison to 28.7 and 30.7 for sGPC2 and sGPC3, respectively. Thus a higher CNR improvement is possible with BphP1.

6.3.1.3 Noise-Equivalent Concentration

Protein	**NEC (μM)**
sGPC2	0.885±0.035
sGPC3	1.041±0.037
BphP1	1.543±0.066

Table 6.3. Comparison of the NEC and standard error of sGPC2, sGPC3, and BphP1.

We compare the purified protein samples of sGPC2, sGPC3, and BphP1 in tube phantoms. We injected purified protein samples of sGPC2, sGPC3, and BphP1 through PFA medical microtubing (BB310-18, Scientific Commodities, Inc.) and immersed them in water. In Table 6.3, we present the noise-equivalent concentration (NEC), which is the minimum detectable concentration, of sGPC2, sGPC3, and BphP1. To determine these values, we used our custom PA imaging system (Fig. 6.2). PA images of 3 tubes in water containing purified protein samples of sGPC2 (89.53 μM), sGPC3 (133.84 μM), and BphP1 (89.17 μM) were taken at wavelengths near their respective peaks of 700 nm (4.3 mJ/cm^2 fluence), 700 nm (4.3 mJ/cm^2 fluence), and 780 nm (5.5 mJ/cm^2

fluence). The protein concentrations were divided by their respective signal-to-noise ratio values to determine their NEC. The NEC and standard error shown are the average of 10 frames.

The NEC of sGPC2 and sGPC3 are slightly better than the NEC of BphP1. These values are better than the 2.7 µM NEC taken at 8 mJ/cm^2 and a depth of 10 mm reported by Yao et al. for BphP1 [28]. This is likely because our experiment was conducted in water so there was effectively no light scattering in comparison to a scattering media at a depth of 10 mm.

6.3.2 Deep Photoacoustic Tube Phantom Imaging

We demonstrate the ability to obtain multiplexed PA difference-spectra demixed images deep in tissue using tube phantoms. We injected 100 mg/mL concentrations of E. coli expressing sGPC2, sGPC3, BphP1, and mIFP through PFA medical microtubing (BB310-18, Scientific Commodities, Inc.) and insert them approximately 10 mm deep in raw chicken breast. mIFP is used as a non-photoconverting contrast agent in addition to the oxygenated and deoxygenated hemoglobin present. We used our custom PA imaging system (Fig. 6.2) and the imaging cycle shown in Fig. 6.3 with t_{cycle} = 20.4 s and 102 pulses per half cycle. The experiment was repeated at 7 different image acquisition wavelengths including 700 nm (9.2 mJ/cm^2), 710 nm (10.7 mJ/cm^2), 720 nm (10.5 mJ/cm^2), 730 nm (10.7 mJ/cm^2), 740 nm (10.9 mJ/cm^2), 750 nm (11.3 mJ/cm^2), and 760 nm (11.3 mJ/cm^2). The imaging wavelengths were also used to simultaneously convert from the far-red to the orange state. The 608 nm wavelength used to photoconvert from the orange to the far-red state had a fluence of 5.4 mJ/cm^2. We compare difference-spectra demixing with traditional spectral demixing.

Fig. 6.9 shows the PA and spectral demixing results. Fig. 6.9 (a) shows the PA difference image taken at 710 nm overlaid on an ultrasound background. Fig. 6.9 (b) shows the PA image taken at 710 nm. Fig. 6.9 (c) and (d) show the PA difference image taken at 710 nm and 760 nm, respectively. Fig. 6.9 (e) and (f) show the traditional PA demixed image and the PA difference-spectra demixed image, respectively. It should be noted that sGPC2 and sGPC3 are demixed together because they have near identical absorption spectra.

PA images are obtained at a depth of around 10 mm in tissue. In Fig. 6.9 (b), signal from the tubes and background blood is visible in addition to the protein signals, but taking the difference image in Fig. 6.9 (c) removes the background and tube signal while leaving the sGPC2 and sGPC3 signal behind. Similarly in Fig. 6.9 (d), the BphP1 signal remains while the other signals are mostly removed. When we compare the traditionally demixed PA image in Fig. 6.9 (e) with the difference-spectra demixed image in Fig. 6.9 (f), we see that the difference-spectra demixed image is better able to distinguish the concentrations of SGPC2/sGPC3 and BphP1. We leave out the demixed oxygenated and deoxygenated hemoglobin in Fig. 6.9 (e) to reduce clutter. mIFP and hemoglobin is not present in the difference-spectra demixed image in Fig. 6.9 (f) because it is subtracted in the difference image. The overall improvement in the difference-spectra demixed image results from the removal of mIFP. It is difficult to demix SGPC2 and mIFP due to their similar absorption spectra and PA signal intensity. It is also noteworthy that in Fig. 6.9 (e), traditional demixing failed to properly demix BphP1 as it was confused with an area of blood outside the highlighted region. While the optical properties of sGPC2 and sGPC3 are the same, differences in expression in E.coli bacteria may account for the differences in PA signal intensities seen in Fig. 6.9.

Comparing the difference image of sGPC2/sGPC3 in Fig. 6.9 (c) to the traditional PA image in Fig. 6.9 (b), we found a 4.2-fold CNR improvement at a 720 nm imaging wavelength, taking blood as the contrast signal. When comparing the difference-spectra demixed image of sGPC2/sGPC3 with traditional demixing, we observe a 1.3-fold CNR improvement using difference-spectra demixing In addition, difference-spectra demixing significantly reduced extraneous signal crosstalk for sGPC2/sGPC3 and BphP1 by 17.9% and 4.8%, respectively.

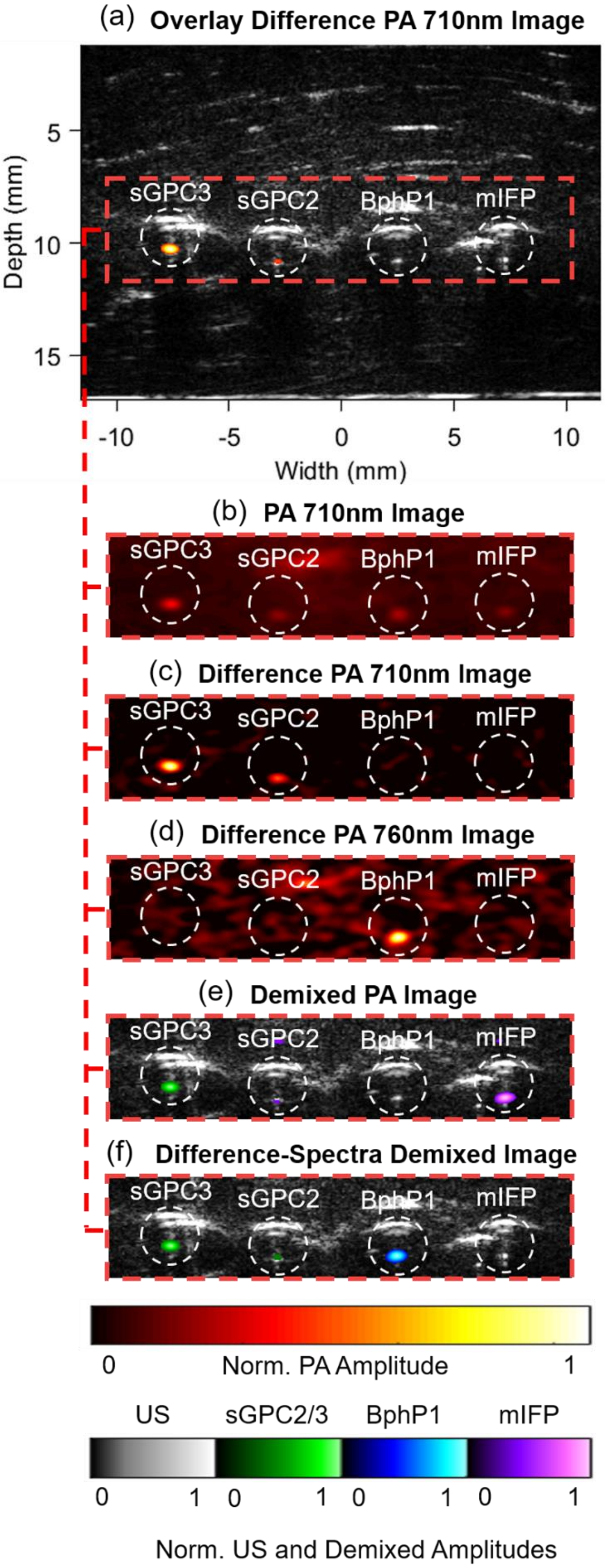

Figure 6.9. Deep tube phantom images of sGPC2, sGPC3, BphP1, and mIFP in chicken breast. (a) PA difference image taken at 710 nm and overlaid on an ultrasound image, (b) PA image taken at 710 nm, (c) PA difference image taken at 710 nm, (d) PA difference image taken at 760 nm, (e) traditionally demixed PA image using 7 wavelengths (700 nm, 710 nm, 720 nm, 730 nm, 740 nm, 750 nm, 760 nm) and overlaid on an ultrasound background, and (f) difference-spectra demixed PA image using the same 7 wavelengths and overlaid on an ultrasound background.

6.3.3 In Vivo Photoacoustic Imaging

We next demonstrate our approach in vivo. We used our custom PA imaging system (Fig. 6.2) and the imaging cycle shown in Fig. 6.3 with $t_{cycle} = 2.4$ s and 12 pulses per half cycle. The experiment was repeated at 7 different image acquisition wavelengths as explained in Section 6.3.2. The 608 nm wavelength was again used to photoconvert from the orange to the far-red state (5.4 mJ/cm^2). We injected 100 mg/mL concentrations of E. coli expressing sGPC2, BphP1, and mIFP into the hind flank of a hairless skid mouse (Nu/Nu, Charles River). mIFP is used as a non-photoconverting contrast agent in addition to the oxygenated and deoxygenated hemoglobin present in vivo. The difference image removes signal from both the mIFP and hemoglobin. In addition, we compare difference-spectra demixing with traditional spectral demixing. All animal experiments were approved by the Animal Care and Use Committee at the University of Alberta.

Fig. 6.10 shows the PA and spectral demixing results. Fig. 6.10 (a) shows the PA difference image taken at 710 nm overlaid on an ultrasound background. Fig. 6.10 (b) shows the PA image taken at 710 nm. Fig. 6.10 (c) and (d) show the PA difference image taken at 710 nm and 760 nm, respectively. Fig. 6.10 (e) and (f) show the traditional PA demixed image and the PA difference-spectra demixed image, respectively.

In Fig. 6.10 (b), a large background signal can be observed in comparison to the sGPC2 signal, but the difference image in Fig. 6.10 (c), removes the background signal. Fig. 6.10 (d) shows the removal of background signal around BphP1 at 760 nm. Comparing the demixed PA image in Fig. 6.10 (e) with the difference-spectra demixed image in Fig. 6.10 (f), we see that the difference-spectra demixed image is again better able to distinguish the concentrations of sGPC2 and BphP1 due to the removal of mIFP, which is difficult to demix due to having a similar absorption spectrum as sGPC2. We leave out the demixed oxygenated and deoxygenated hemoglobin in Fig. 6.10 (e) to reduce clutter. mIFP and hemoglobin is not present in the difference-spectra demixed image in Fig. 6.10 (f) because it is subtracted in the difference images.

Comparing the difference image of sGPC2 to the traditional PA image, we found a 21.6-fold CNR improvement at a 720 nm imaging wavelength and taking mIFP as the reference signal. When comparing the difference-spectra demixed image of sGPC2 with traditional demixing, we observe a 1.7-fold CNR improvement using difference-spectra demixing. In addition, difference spectra demixing significantly reduced extraneous crosstalk for sGPC2 and BphP1 by 8.2% and 40.2%, respectively.

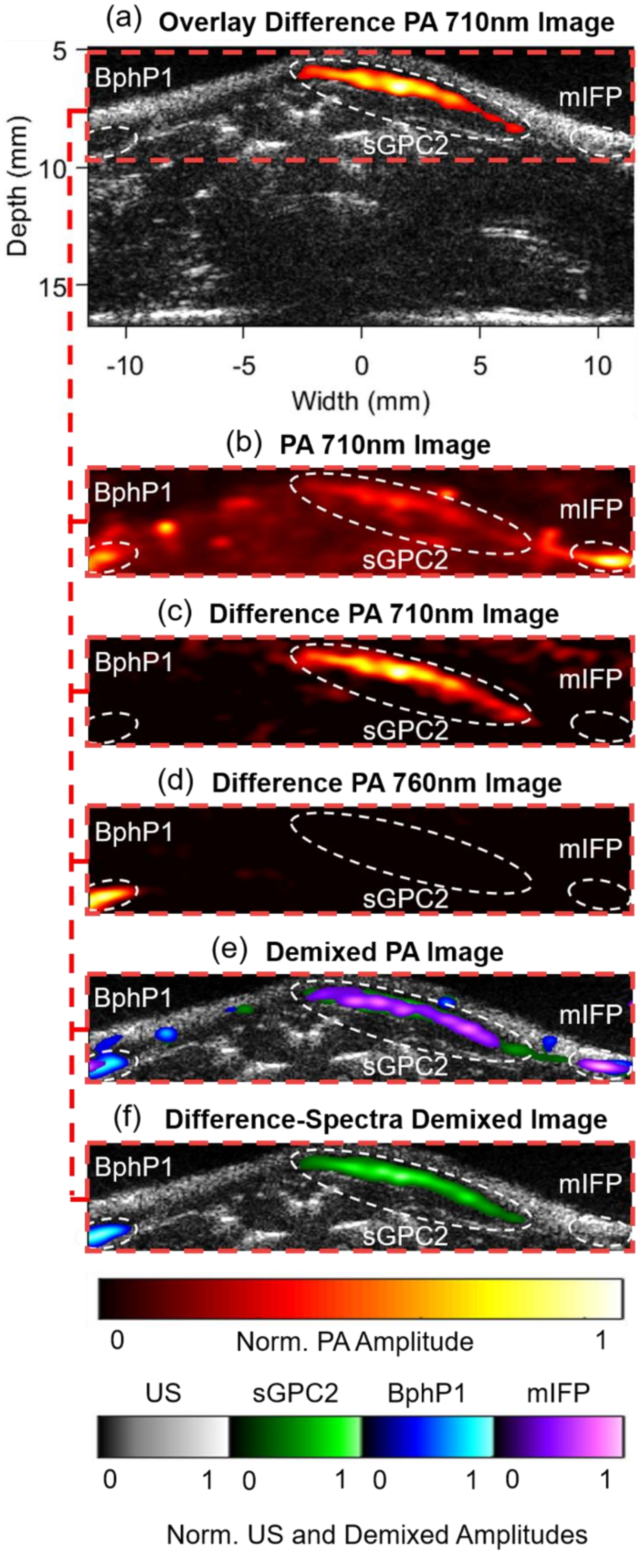

Figure 6.10. In vivo images of sGPC2, BphP1, and mIFP injected into a mouse. (a) PA difference image taken at 710 nm and overlaid on the ultrasound image, (b) PA image taken at 710 nm, (c) PA difference image taken at 710 nm, (d) PA difference image taken at 760 nm, (e) traditionally demixed PA image using 7 wavelengths (700 nm, 710 nm, 720 nm, 730 nm, 740 nm, 750 nm, 760 nm) and overlaid on an ultrasound background, and (f) difference-spectra demixed PA image using the same 7 wavelengths and overlaid on an ultrasound background.

6.4 Discussion

sGPC2 and BphP1 are part of a growing palette of far-red photoswitchable chromoproteins capable of suppressing non-photoconverting blood and significantly improving the CNR in molecular PA images. We have demonstrated the ability to improve spectral demixing using difference images compared to traditional PA spectral demixing. This opens the door to improved multiplexing of low-background molecular contrast agents.

We are currently able to obtain difference PA images at a rate of 1 frame per second. With the implementation of higher laser fluences and faster laser pulse repetition rates, even faster difference PA image acquisition speeds may be possible. While we expect that faster photoconversion will occur with higher fluence, there may be a limit to the fluence that can be used without significant photobleaching.

We have not expressed sGPC2 or sGPC3 in mammalian cells and that is left to future work. We chose to focus on the feasibility of multiplexed imaging of reversibly switchable chromoproteins as a first step. That being said, bacteria models could have important applications in the study of infection and bacterial drug efficacy.

While we use demixing to distinguish different proteins, it may be possible to distinguish between different reversibly switchable chromoproteins by imaging at wavelengths where only one significantly photoconverts as is the case at 710 nm and 760 nm for sGPC2 and BphP1. In addition, we have noted that reversibly photoswitchable chromoproteins have different photoconversion rates depending on the fluence and photoconversion wavelength, so it may be possible to distinguish between spatially separated proteins using their respective photoconversion rates. Similarly, it may also be possible to distinguish between spatially separated photoswitchable chromoproteins via their relative PA intensity changes from the far-red to the orange state. Exploration of these techniques has also been left for future work.

6.5 Conclusion

Multiplexed PA imaging of photoswitchable chromoproteins will be essential to imaging multiple targets with high sensitivity. We have introduced difference-spectra demixing for simultaneously imaging multiple photoswitchable reporters with low PA background. Difference-spectra demixing has shown improved reporter differentiation in comparison to traditional demixing. We present the second far-red reversibly switchable chromoproteins (sGPC2), which is one-tenth the size of BphP1 and photoswitches 4-times faster. We have demonstrated imaging of these photoswitchable reporters in deep tissue and in vivo with improved differentiation and multiplexing. As more reversibly switchable chromoproteins are discovered, scientists will now have the ability to image and track multiple reporters simultaneously, allowing PA molecular imaging to image complex molecular processes with high sensitivity.

References

1. T. F. Massoud and S. S. Gambhir, "Molecular imaging in living subjects: seeing fundamental biological processes in a new light," Genes Dev. **17,** 545-580 (2003).

2. M. A. Pysz, S. S. Gambhir, and J. K. Willmann, "Molecular imaging: current status and emerging strategies," Clin. Radiol. **65,** 500-516 (2010).

3. M. Rudin and R. Weissleder, "Molecular imaging in drug discovery and development," Nature reviews Drug discovery **2,** 123-131 (2003).

4. J. K. Willmann, N. van Bruggen, L. M. Dinkelborg, and S. S. Gambhir, "Molecular imaging in drug development," Nature Reviews Drug Discovery **7,** 591-607 (2008).

5. R. Weissleder and M. J. Pittet, "Imaging in the era of molecular oncology," Nature **452,** 580-589 (2008).

6. R. Weissleder, "Molecular imaging in cancer," Science **312,** 1168-1171 (2006).

7. E. L. Que, D. W. Domaille, and C. J. Chang, "Metals in neurobiology: probing their chemistry and biology with molecular imaging," Chem. Rev. **108,** 1517-1549 (2008).

8. F. A. Jaffer and R. Weissleder, "Molecular imaging in the clinical arena," JAMA **293,** 855-862 (2005).

9. A. Hellebust and R. Richards-Kortum, "Advances in molecular imaging: targeted optical contrast agents for cancer diagnostics," Nanomedicine **7,** 429-445 (2012).

10. M. G. Pomper, "Molecular imaging: an overview," Acad. Radiol. **8,** 1141-1153 (2001).

11. K. Pu, A. J. Shuhendler, J. V. Jokerst, J. Mei, S. S. Gambhir, Z. Bao, and J. Rao, "Semiconducting polymer nanoparticles as photoacoustic molecular imaging probes in living mice," Nature nanotechnology **9,** 233-239 (2014).

12. D. Pan, M. Pramanik, A. Senpan, J. S. Allen, H. Zhang, S. A. Wickline, L. V. Wang, and G. M. Lanza, "Molecular photoacoustic imaging of angiogenesis with integrin-targeted gold nanobeacons," FASEB J. **25,** 875-882 (2011).

13. A. d. l. Zerda, Z. Liu, S. Bodapati, R. Teed, S. Vaithilingam, B. T. Khuri-Yakub, X. Chen, H. Dai, and S. S. Gambhir, "Ultrahigh sensitivity carbon nanotube agents for photoacoustic molecular imaging in living mice," Nano letters **10,** 2168-2172 (2010).

14. D. Pan, M. Pramanik, A. Senpan, X. Yang, K. H. Song, M. J. Scott, H. Zhang, P. J. Gaffney, S. A. Wickline, and L. V. Wang, "Molecular photoacoustic tomography with colloidal nanobeacons," Angewandte Chemie International Edition **48,** 4170-4173 (2009).

15. P. Li, C. C. Wang, D. Shieh, C. Wei, C. Liao, C. Poe, S. Jhan, A. Ding, and Y. Wu, "In vivo photoacoustic molecular imaging with simultaneous multiple selective targeting using antibody-conjugated gold nanorods," Optics Express **16,** 18605-18615 (2008).

16. S. Gross and D. Piwnica-Worms, "Spying on cancer: molecular imaging in vivo with genetically encoded reporters," Cancer cell **7,** 5-15 (2005).

17. T. Knöpfel, J. Díez-García, and W. Akemann, "Optical probing of neuronal circuit dynamics: genetically encoded versus classical fluorescent sensors," Trends Neurosci. **29,** 160-166 (2006).

18. A. E. Palmer, Y. Qin, J. G. Park, and J. E. McCombs, "Design and application of genetically encoded biosensors," Trends Biotechnol. **29,** 144-152 (2011).

19. D. M. Chudakov, S. Lukyanov, and K. A. Lukyanov, "Fluorescent proteins as a toolkit for in vivo imaging," Trends Biotechnol. **23,** 605-613 (2005).

20. Y. Li, A. Forbrich, J. Wu, P. Shao, R. E. Campbell, and R. Zemp, "Engineering Dark Chromoprotein Reporters for Photoacoustic Microscopy and FRET Imaging," Sci. Rep. **6,** 22129 (2016).

21. D. M. Shcherbakova and V. V. Verkhusha, "Near-infrared fluorescent proteins for multicolor in vivo imaging," Nature methods **10,** 751-754 (2013).

22. A. Krumholz, D. M. Shcherbakova, J. Xia, L. V. Wang, and V. V. Verkhusha, "Multicontrast photoacoustic in vivo imaging using near-infrared fluorescent proteins," Sci. Rep. **4,** 3939 (2014).

23. G. S. Filonov, A. Krumholz, J. Xia, J. Yao, L. V. Wang, and V. V. Verkhusha, "Deep-Tissue Photoacoustic Tomography of a Genetically Encoded Near-Infrared Fluorescent Probe," Angewandte Chemie International Edition **51,** 1448-1451 (2012).

24. D. Shcherbo, E. M. Merzlyak, T. V. Chepurnykh, A. F. Fradkov, G. V. Ermakova, E. A. Solovieva, K. A. Lukyanov, E. A. Bogdanova, A. G. Zaraisky, and S. Lukyanov, "Bright far-red fluorescent protein for whole-body imaging," Nature methods **4,** 741-746 (2007).

25. C. Liu, X. Gong, R. Lin, F. Liu, J. Chen, Z. Wang, L. Song, and J. Chu, "Advances in imaging techniques and genetically encoded probes for photoacoustic imaging," Theranostics **6,** 2414 (2016).

26. L. V. Wang and S. Hu, "Photoacoustic tomography: in vivo imaging from organelles to organs," Science **335,** 1458-1462 (2012).

27. S. Y. Emelianov, P. C. Li, and M. O'Donnell, "Photoacoustics for molecular imaging and therapy," Phys Today **62,** 34-39 (2009).

28. J. Yao, A. A. Kaberniuk, L. Li, D. M. Shcherbakova, R. Zhang, L. Wang, G. Li, V. V. Verkhusha, and L. V. Wang, "Multiscale photoacoustic tomography using reversibly switchable bacterial phytochrome as a near-infrared photochromic probe," Nature methods **13,** 67-73 (2016).

29. A. C. Stiel, X. L. Deán-Ben, Y. Jiang, V. Ntziachristos, D. Razansky, and G. G. Westmeyer, "High-contrast imaging of reversibly switchable fluorescent proteins via temporally unmixed multispectral optoacoustic tomography," Opt. Lett. **40,** 367-370 (2015).

30. F. V. Subach, L. Zhang, T. W. Gadella, N. G. Gurskaya, K. A. Lukyanov, and V. V. Verkhusha, "Red fluorescent protein with reversibly photoswitchable absorbance for photochromic FRET," Chem. Biol. **17,** 745-755 (2010).

31. R. Narikawa, T. Ishizuka, N. Muraki, T. Shiba, G. Kurisu, and M. Ikeuchi, "Structures of cyanobacteriochromes from phototaxis regulators AnPixJ and TePixJ reveal general and specific photoconversion mechanism," Proc. Natl. Acad. Sci. U. S. A. **110,** 918-923 (2013).

32. D. Bellini and M. Z. Papiz, "Structure of a bacteriophytochrome and light-stimulated protomer swapping with a gene repressor," Structure **20,** 1436-1446 (2012).

33. R. Narikawa, T. Nakajima, Y. Aono, K. Fushimi, G. Enomoto, Ni-Ni-Win, S. Itoh, M. Sato, and M. Ikeuchi, "A biliverdin-binding cyanobacteriochrome from the chlorophyll d-bearing cyanobacterium Acaryochloris marina," Sci. Rep. **5,** 7950 (2015).

34. J. Sambrook, E. F. Fritsch, and T. Maniatis, *Molecular cloning: a laboratory manual.* (Cold spring harbor laboratory press, 1989).

35. M. Fromant, S. Blanquet, and P. Plateau, "Direct random mutagenesis of gene-sized DNA fragments using polymerase chain reaction," Anal. Biochem. **224,** 347-353 (1995).

36. E. A. Rodriguez, G. N. Tran, L. A. Gross, J. L. Crisp, X. Shu, J. Y. Lin, and R. Y. Tsien, "A far-red fluorescent protein evolved from a cyanobacterial phycobiliprotein," Nature methods **13,** 763-769 (2016).

37. G. S. Filonov, K. D. Piatkevich, L. Ting, J. Zhang, K. Kim, and V. V. Verkhusha, "Bright and stable near-infrared fluorescent protein for in vivo imaging," Nat. Biotechnol. **29,** 757-761 (2011).

38. Y. Wang, J. Xia, and L. V. Wang, "Deep-tissue photoacoustic tomography of Förster resonance energy transfer," J. Biomed. Opt. **18,** 101316-101316 (2013).

39. D. Yu, M. A. Baird, J. R. Allen, E. S. Howe, M. P. Klassen, A. Reade, K. Makhijani, Y. Song, S. Liu, and Z. Murthy, "A naturally monomeric infrared fluorescent protein for protein labeling in vivo," Nature methods **12,** 763-765 (2015).

40. X. Shu, A. Royant, M. Z. Lin, T. A. Aguilera, V. Lev-Ram, P. A. Steinbach, and R. Y. Tsien, "Mammalian expression of infrared fluorescent proteins engineered from a bacterial phytochrome," Science **324,** 804-807 (2009).

7. Photoacoustic Tumour Volume Estimation for p110β Knockout Study

7.1 Introduction

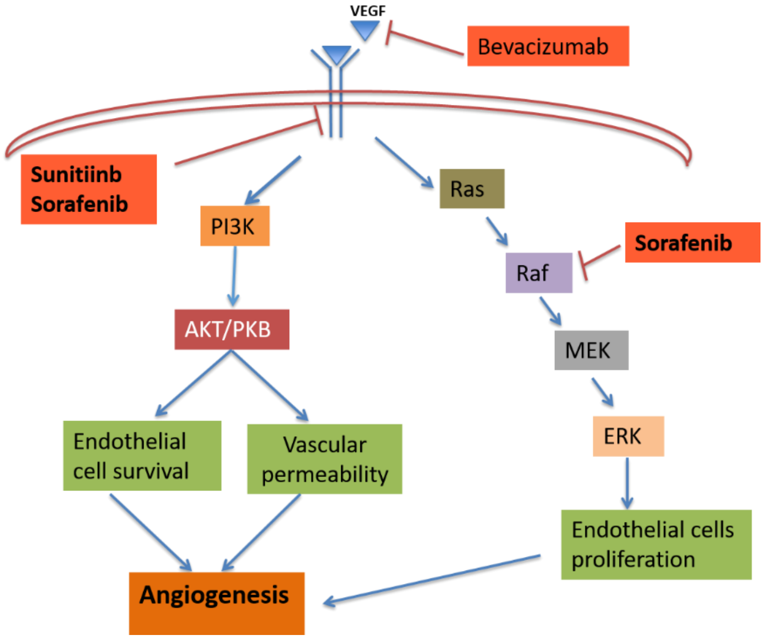

Figure 7.1. The pathways for angiogenesis are shown along with the anti-angiogenic drugs and there regions of effect.

Angiogenesis is essential for tumour growth and metastasis. It is for this reason that numerous anti-angiogenic drugs have been developed and approved for clinical use in cancer treatment [1]. Despite treatment with anti-angiogenic drugs, tumours can develop resistance and continue to grow as was shown in a study of renal-cell carcinoma [2]. Tumour angiogenesis have been shown to occur via various pathways. Signaling of these pathways has been associated with the signaling protein vascular endothelial growth factor (VEGF) [3]. Fig. 7.1 shows the angiogenesis signaling pathways of VEGF. Anti-angiogenic drugs (Bevaizumab, Sunitinib, and Sorafenib) are shown in Fig. 7.1 at the points along the pathway where they inhibit signaling. One of the pathways involved in VEGF signaling of angiogenesis involves isoforms of phosphoinositide 3-kinase (PI3K) [4]. It has been shown that the PI3K pathway may be able to signal itself without VEGF. This was determined because even after sunitinib (an anti-angiogenic drug that blocks the signaling of VEGF) is administered, tumour cells can develop a resistance to the drug and continue to grow. Fig. 7.2 shows the tumour resistance and growth in orthoxenograft mouse models (Ren28 and Ren96) which have been treated with sunitinib [5]. In both models, the tumour progression of a control mouse is compared to that of a mouse treated with sunitinib. It has recently been confirmed that signaling of the PI3K pathway can indeed occur without VEGF signaling via a catalytic subunit of PI3K known as p110β [6]. It was shown that endothelial cells transfected with siRNA to cause p110β deficiency (p110β) had decreased sprouting compared with endothelial cells transfected with nonspecific siRNA (NS) and nontransfected endothelial cells (NT) [6]. p110β is activated by G-protein coupled receptors (GPCRs) which signals angiogenesis through the PI3K pathway. Fig. 7.3 shows the mechanism for p110β signaling of angiogenesis. It is currently under investigation whether inhibition of the p110β combined with the treatment of sunitinib can cause a decrease in tumour metastasis.

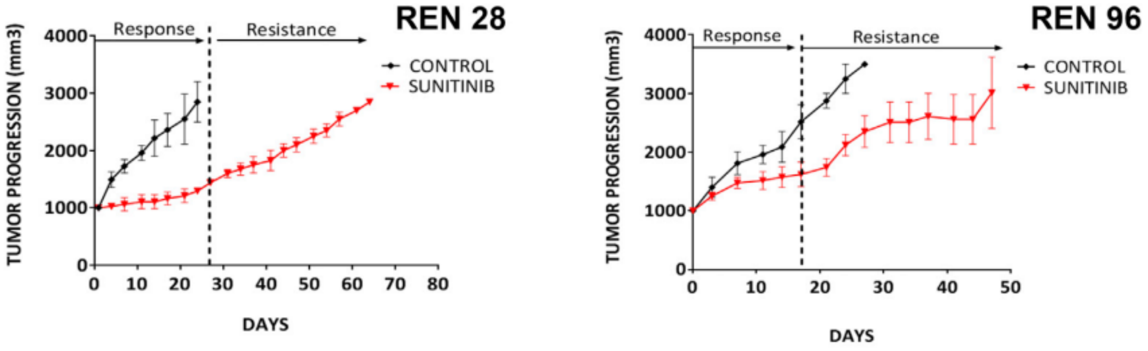

Figure 7.2. Tumour progression in orthoxenograft mouse models (Ren28 and Ren96). The tumour progression of a control mouse is compared to a mouse treated with sunitinib [5].

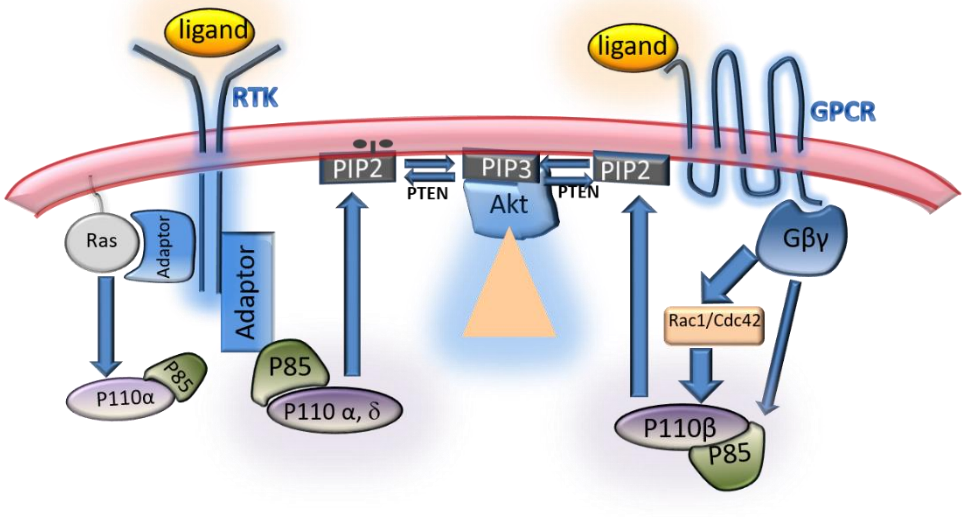

Figure 7.3. The mechanism for p110β signaling of angiogenesis.

Studies of effective tumour treatments are often done first on mice with the effectiveness determined by ex vivo histology obtained by sacrificing mice at certain time points. This method is less than ideal because a single mouse cannot be monitored over the entire duration of treatment.

Instead several mice need to be sacrificed at different time points to perform histology which can lead to variability due to variations in tumour growth in different mice. Ideally, histology could be performed in vivo using a noninvasive imaging technique, but common biomedical imaging techniques lack either the resolution, penetration depth, or specificity required to perform in vivo histology in mice. Photoacoustic (PA) imaging may be the exception to this. Unlike other biomedical imaging techniques, PA imaging has excellent resolution at the depth required to image small animals and is capable of soft tissue specificity. In PA imaging, a laser pulse is used to excite tissue causing thermoacoustic expansion resulting in an ultrasound (US) wave or PA signal. This PA signal is proportional to the optical absorption of the tissue and can be spectrally demixed at different wavelengths to differentiate between different soft tissue like cancerous and noncancerous tissue. Before in vivo histology can be done with PA imaging, it must first be determined whether histology can be done using PA imaging with quantitative accuracy. Unfortunately, quantitative PA imaging is non-trivial. One of the main challenges is non-uniform illumination, which could lead to non-tissue specific variations in PA signal strength. One solution to this could be using multiple illuminations at different angles [7, 8]. In addition, tissue specificity requires spectral demixing using multiple imaging wavelengths to differentiate between different optical absorptions in tissue [9]. In spite of these challenges, PA imaging has been used to quantitatively access blood oxygenation and hemoglobin concentration [10]. In this paper, we will determine whether PA imaging is a viable option for quantitatively determining tumour volumes in ex vivo lung samples by comparing them to histology obtained via traditional staining. If successful, this work could lead to future uses of PA imaging for in vivo histology. This work is done in collaboration with a study to determine the effects of p110β on tumour angiogenesis.

7.2 Methods

We use a p110β knockout mouse model (p110β KO) to determine the effects of p110β on tumour angiogenesis. Tie2-Cre was used to generate endothelial cell specific p110β KO mice. We inject 2×10^5 B16F10 mouse melanoma cells in the tail vein of each mouse and let them grow for 20 days. They are also treated with 40 mg of sunitinib per kg of mouse every day for 20 days. The littermate mice are used as the control. They were born from the same breeding colony as the p110β knockout mice but did not have the p110β deletion. We compare the tumour growth in the lungs between the littermate and p110β KO mice using ex vivo histology. Haemotoxylin and eosin (H&E) staining and PA imaging are used for ex vivo histology of the lung samples. The same lung samples are not used for both H&E staining and PA imaging, but they did originate from the same mice. The sample size for these experiments was 9 littermate mice and 11 p110β KO mice. H&E staining was performed at the HistoCore facility (Alberta Diabetes Institute, University of Alberta) with a slice thickness of 5 µm. Fig. 7.4 (b) shows an example of an H&E stained lung sample slice. Fractional tumour volume is determined by dividing the number of image pixels containing tumours by the total image pixels containing the sample across all slices.

For the PA imaging, we use a pre-clinical PA imaging system (Vevo LAZR, VisualSonics, Fujifilm) with a 40 MHz transducer (VisualSonics LZ550, VisualSonics, Fujifilm) to obtain PA images of the ex vivo lung samples overlaid on an US background. We scan the transducer a total length of 10.160 mm with a step size of 0.102 mm for 101 total frames to obtain a 3D image of the lung samples. PA images are taken at imaging wavelengths of 680 nm, 700 nm, 750 nm, 800 nm, 850 nm, 900 nm, and 950 nm at each scan position. We perform spectral demixing to distinguish the melanin in the melanoma from the blood. Imaging was done with a 34-dB PA gain and a 22-dB US gain. The US and PA image contrast was set to maximum so that all PA and US signals had maximum intensity. PA signal brightness is set to the same value for all PA images. The PA system may initially need to be calibrated to determine the optimal brightness for accurate PA tumour histology. Fig. 7.4 (c) shows an example of a 2D PA image of a lung sample. Tumour quantity is determined by the number of pixels containing PA signal. We determine the fractional tumour volume by dividing the total number of PA tumour signal pixels by the total number of US lung pixels across all slices.

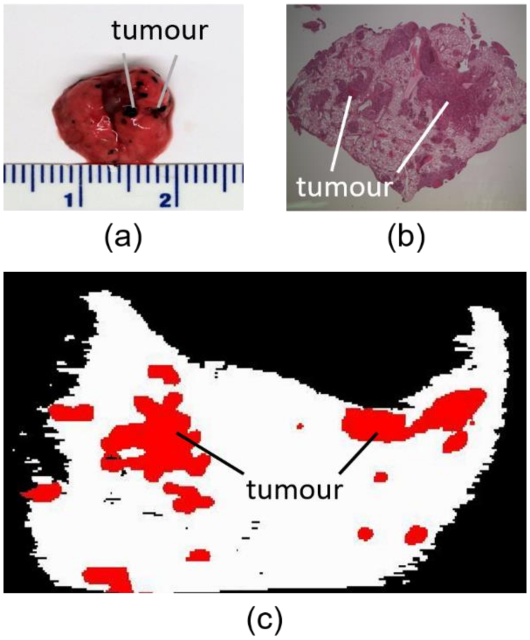

Figure 7.4. Images of lung samples: (a) image of an entire lung sample, (b) 2D slice image of an H&E stained lung sample, and (c) 2D PA image of a lung sample. Examples of tumours in the lung samples are labelled.

Fig. 7.4 (a) shows an example of the mouse lung samples used with the tumours shown in black. The entire sample measures roughly 1.3 cm across. Fig. 7.4 (b) shows a lung sample slice stained with H&E with the tumours shown in purple. Fig. 7.4 (c) shows a single 2D PA image of a lung sample with the tumours shown in red.

7.3 Results

Table 7.1 shows the tumour volume percentage (tumour %) obtained from both PA imaging and H&E staining for both littermate and p110β KO mice. As previously mentioned, both groups are also treated with sunitinib. The results show that there is no significant variation between the tumour % obtained from PA imaging vs H&E staining for both the littermate (0.97) and the p110β KO (0.65) groups, which is promising for PA imaging as a quantitative imaging technique. The study done in collaboration to determine the effects of p110β on tumour angiogenesis is still under underway, and any link between p110β and tumour angiogenesis will be determined upon its completion.

Littermates			p110β KO		
	H&E Tumour %	PA Tumour %		H&E Tumour %	PA Tumour %
Mean	17.7	18.0	Mean	9.8	11.6
Std.	173.9	174.8	Std.	59.8	104.1
Equal-variance Two-tail T-test, P(T<=t)					
Littermate [PA vs H&E]		0.97	p110β KO [PA vs H&E]		0.65

Table 7.1. Comparison of the tumour volume percentage obtained via PA imaging and H&E staining. Results for the littermate mice are contained in the top left half of the table, and results for the p110β KO mice are contained in the top right half of the table. T-test results comparing PA imaging vs H&E staining for the littermate and p110β KO groups are shown in the bottom half of the table.

7.4 Discussion

There appears to be some difference between the tumour volumes of the littermate and p110β KO mice. It will be determined at the completion of the investigation whether such results carry significance. Limiting factors in this experiment include using tumour growth as an indirect measure of angiogenesis and the small sample size.

There is also a limiting factor in the comparison between PA imaging and H&E staining. We use different lung samples from the same mouse to compare PA imaging and H&E staining, which is not ideal due to variation between samples from different parts of the lung. We hoped that over multiple samples the mean tumour % from different lung samples of the same mice would on average be the same, but this may not be the case. Using the same lung sample would be a more accurate measure and allow better calibration of the brightness setting for PA spectral demixing. Future work should compare identical samples using both PA imaging and H&E staining.

7.5 Conclusion

We demonstrate the potential of PA imaging for quantitative biomedical research. PA imaging was able to obtain histology measurements comparable to H&E staining. While we have used it ex vivo, future work could involve using PA imaging for in vivo histology over the duration of treatment. Further research is required to determine the link between p110β and tumour angiogenesis. The results could have significant impact on anti-angiogenic drug treatment.

References

1. J. Folkman, "Angiogenesis: an organizing principle for drug discovery?" Nature reviews Drug discovery **6,** (2007).

2. B. I. Rini and M. B. Atkins, "Resistance to targeted therapy in renal-cell carcinoma," The lancet oncology **10,** 992-1000 (2009).

3. P. Carmeliet and R. K. Jain, "Molecular mechanisms and clinical applications of angiogenesis," Nature **473,** 298-307 (2011).

4. B. Vanhaesebroeck, J. Guillermet-Guibert, M. Graupera, and B. Bilanges, "The emerging mechanisms of isoform-specific PI3K signalling," Nature reviews Molecular cell biology **11,** 329-341 (2010).

5. G. Jiménez-Valerio, M. Martínez-Lozano, N. Bassani, A. Vidal, M. Ochoa-de-Olza, C. Suárez, X. García-del-Muro, J. Carles, F. Viñals, and M. Graupera, "Resistance to antiangiogenic therapies by metabolic symbiosis in renal cell carcinoma PDX models and patients," Cell reports **15,** 1134-1143 (2016).

6. G. Haddad, P. Zhabyeyev, M. Farhan, L. F. Zhu, Z. Kassiri, D. C. Rayner, B. Vanhaesebroeck, G. Y. Oudit, and A. G. Murray, "Phosphoinositide 3-kinase beta mediates microvascular endothelial repair of thrombotic microangiopathy," Blood **124,** 2142-2149 (2014).

7. R. J. Zemp, "Quantitative photoacoustic tomography with multiple optical sources," Appl. Opt. **49,** 3566-3572 (2010).

8. P. Shao, B. Cox, and R. J. Zemp, "Estimating optical absorption, scattering, and Grueneisen distributions with multiple-illumination photoacoustic tomography," Appl. Opt. **50,** 3145-3154 (2011).

9. B. Cox, J. G. Laufer, S. R. Arridge, and P. C. Beard, "Quantitative spectroscopic photoacoustic imaging: a review," J. Biomed. Opt. **17,** 0612021-06120222 (2012).

10. J. Laufer, D. Delpy, C. Elwell, and P. Beard, "Quantitative spatially resolved measurement of tissue chromophore concentrations using photoacoustic spectroscopy: application to the measurement of blood oxygenation and haemoglobin concentration," Phys. Med. Biol. **52,** 141 (2006).

8. Conclusion

8.1 Summary of Thesis

The work in this thesis aims to develop and improve 3D photoacoustic (PA) molecular imaging. PA imaging is a valuable imaging modality as it has higher imaging rates and resolutions at several centimeter depths than any other imaging technique. This makes it possibly ideal for small animal imaging, which is fundamental to scientific research. PA imaging also has many other applications including detecting and managing cancers, imaging atherosclerotic plaques, ocular imaging, and measuring blood oxygen saturation among others. Molecular contrast agents can further enhance PA imaging by allowing it to visualize molecular processes in vivo. This can be applied to understanding disease mechanisms of action, aiding drug development, detecting disease biomarkers, and studying biochemistry. Improved 3D PA molecular imaging will benefit many of these promising applications. This thesis has identified several key developments that will be needed to achieve this vision.

1. **Larger 2D transducer arrays for PA imaging**

   Large 2D ultrasound transducer arrays require many transmit-receive channels to address its many elements. The large number of channels add significant design complexity that prevents very large arrays from being made.

2. **Fast 3D imaging speeds with large 2D transducer arrays**

   Large 2D transducer arrays use integrated beamforming electronics to reduce large channel numbers. The integrated beamforming electronics beamform one 2D image at a time. Thus, 3D imaging speed is significantly reduced because 3D images are composed of multiple 2D slices.

3. **Ultra-broadband transducers for PA molecular imaging**

   Current high-frequency clinical ultrasound transducers are ill-suited for detecting molecular contrast agents required for molecular imaging. Molecular contrast agent distribution produce lower frequency signals that cannot be detected by high-frequency transducers designed to image fine vasculature.

4. **Multiplexed low-background PA molecular imaging**

   PA background reduction is necessary for sensitive contrast agent detection amongst high blood background signals. Multiplexed imaging is necessary because real molecular process are complex interactions involving multiple targets of interest. Thus, the ability to simultaneously image and differentiate multiple background-reducing molecular contrast agents is crucial for PA molecular imaging.

5. **Quantitative PA molecular imaging in vivo**

   The quantitative accuracy of PA imaging in vivo is essential to many of its promising applications. Thus, the accuracy of quantitative PA imaging must be compared to traditional measurement methods.

We have advanced 3D molecular PA imaging by making important contributions to address each of the key areas mentioned above.

1. **TOBE CMUTs for 3D PA imaging**

   Traditional large 2D transducer technology reduces channel complexity via integrated beamforming electronics which limits the addressability of individual elements of an array. The TOBE CMUT has previously been introduced as an ultrasound transducer that reduces channel requirements without the need for potentially complicated and costly integrated beamforming electronics while maintaining individual element addressability. We apply the TOBE CMUT to 3D PA imaging and demonstrate its potential as a PA transducer. The reduced channel requirements will allow larger arrays to be developed, which will result in larger fields-of-view. In addition, the individual element addressability may allow us to implement unique receive aperture patterns for improved PA signal acquisition.

2. **Modulation encoding for fast 3D PA imaging**

   Traditionally, to address the large channel requirements for large 2D transducer arrays, integrated beamforming electronics are implemented, which requires 3D images to be acquired slice by slice. TOBE CMUTs also sacrifice 3D imaging speed to reduce channel complexity by acquiring data column by column. This means that the 3D imaging speed of a TOBE CMUT decreases with array size. We introduce a novel way of operating TOBE CMUTs known as modulation encoding that may allow a 3D PA image to be acquired from the entire transducer array in a single laser shot. In modulation encoding, each column of the array contains a different high frequency carrier signal that modulates the PA signal. All of the PA signals and high frequency carriers are received from the rows at once but can be demodulated to obtain the original PA signals from each element of the array.

3. **Interlaced multifrequency CMUTs for PA molecular imaging**

   Traditional PA imaging transducers are optimized to detect high frequencies, which are the frequencies responsible for imaging fine details in high resolution. However, PA signals consist of a very broad range of frequencies. We show the need for sensitive detection of both low- and high-frequency PA signals in molecular imaging. Low-frequency signals are typically generated by large diffuse contrast agent concentrations, while high-frequency signals will be generated by fine vasculature and structures in the body. To obtain high resolution PA molecular images that are sensitive to molecular contrast agents, we introduce interlaced multifrequency CMUTs with interlaced low- and high-frequency elements. The interlaced multifrequency design minimizes grating lobes, which reduce imaging artifacts. We demonstrate that interlaced multifrequency CMUTs are able to take co-aligned PA images with both the low- and high-frequency elements, allowing both sensitive contrast agent detection and high resolution PA imaging.

4. **sGPC2/sGPC3 and multiplexed low-background PA molecular imaging**

   PA molecular imaging is limited by high blood background signals. The photoswitchable chromoprotein BphP1 was previously developed to reduce background signals. Photoswitchable chromoproteins can be reversibly switched between two absorption states. By subtracting an image taken at one absorption state from an image taken at another absorption state, we can create images of signal intensity change and thus significantly reduce the unchanged background signals. In addition to background reduction, multiplexing is also essential. Molecular processes are complex interactions between many different targets of interest. Imaging these complex molecular processes require several reporters and improved reporter differentiation. We introduce a second photoswitchable chromoprotein (sGPC2) as well as an improved multiplexed photoswitchable imaging technique known as difference-spectra demixing. We characterize sGPC2 and demonstrate the ability to simultaneously image and differentiate between sGPC2 and BphP1 using difference-spectra demixing.

5. **PA imaging for tumour volume estimation**

   PA imaging has potential for taking quantitative measurements in small animal in vivo. However, research has not compared PA imaging with traditional measurement techniques. PA imaging must first be compared ex vivo before it can be confidently used for in vivo longitudinal studies. We apply 3D PA imaging to the quantitative estimation of tumour volumes in a tumour angiogenesis study. We compare mean tumour volume estimations obtained with PA imaging to measurements obtained via traditional staining histology.

8.2 Future Work

The work in this thesis has prompted ongoing research in the field. For TOBE CMUTs, TOBE device modeling [1] and new ultrasound imaging schemes for TOBE CMUTs are being developed [2]. Work is currently being done to wire the TOBE arrays to an imaging board and use unique receive patterns for improved PA signal detection. The concept of a bias sensitive crossed electrode array like the TOBE CMUTs is currently being implemented with bias sensitive piezoelectric relaxor arrays. The concept of modulation encoding for fast 3D PA imaging is being considered for use in the relaxor arrays as well. The interlaced multifrequency CMUTs continue to be optimized. A new device model has been developed to improve the efficiency and performance of the interlaced multifrequency CMUT design [3]. Using this model, new versions of the multifrequency CMUTs are being fabricated and tested for improved performance.

Despite the significant advances in CMUT technology, there are still several limitations that need to be addressed for the field in general. The reliability of CMUTs is of major concern. This includes the ability of CMUTs to be repeatedly used without degradation in performance due to device charging. Device charging changes the effective bias voltage on the devices and thus results in unexpected changes in performance over time, which could makes it more difficult to obtain reliable quantitative imaging results. One approach to address this, which is currently being explored, is to use isolation posts between the top and bottom membranes to mitigate the effective area through which charging can occur. Another reliability concern has to do with the manufacturing of consistently uniform devices. It is challenging to create large arrays that contain a full set of active elements. This may be attributed to the complexity of microfabrication. Creating robust designs that can be repeatedly and easily fabricated with few errors will be vital to the transition of CMUTs from research technology to industry.

More work needs to be done in developing and optimizing PA molecular photoswitchable imaging technology. Complex molecular process will require multiple targets to be tagged and monitored by different photoswitchable reporters. Thus, having a large palette of photoswitchable reporters will be essential to our ability to study complex molecular systems. More work needs to done on sGPC2 to express the protein in mammalian cells to increase the applicability for biomedical research. Doing so will open the door to many more fields of study including oncology, immunology, and cell biology. In addition, multiplexed imaging of photoswitchable chromoproteins requires a complex imaging system involving multiple high-power lasers for both photoconversion and imaging, which is currently not readily accessible to the general public. Commercial imaging systems for multiplexed PA photoswitchable imaging must be developed to make this technology accessible to a non-expert. Of primary concern to these systems will be the long-term reliability of the high-power lasers. Laser with imaging wavelengths and power relevant to biomedical imaging are notoriously difficult to maintain long term. Improvements in laser reliability will be essential to the adoption of PA imaging technology in general.

The promise of PA imaging for in vivo longitudinal studies is one of its most promising applications and requires further development. Improvements in quantitative PA estimation must be done to compensate for non-uniform fluence distributions. With respect to our work, a direct comparison between PA imaging and traditional staining histology on the same samples will be necessary to calibrate the PA imaging measurements and improve measurement comparisons. If accurate ex vivo measurements can be obtained, then an in vivo study using PA imaging should be conducted where in vivo measurements are later verified ex vivo.

Finally, much of this work has been done separately to advance different aspects of 3D PA molecular imaging. It would be valuable to combine these advances into a single system. The development of an interlaced multifrequency TOBE array, for example, could allow large field-of-view imaging with reduced channel requirements, multifrequency capabilities, and modulation encoding potential. Using such an array to image multiplexed photoswitchable reporters would be a significant advance in 3D PA molecular imaging. With these technical advances, we hope to provide toolsets to answer biological questions about multiple signalling pathways in deep tissue in vivo. Such capabilities do not yet exist but could prove highly valuable for fields such as cancer, immunotherapy, neuroscience, etc.

8.3 Outlook

PA imaging is a powerful molecular imaging technique with the potential to be a breakthrough for small animal imaging. There is a wealth of research that is being done on PA molecular imaging, which reflects the promise that it has for science and medicine. The work done in this thesis has pushed the boundaries of 3D PA molecular imaging and inspired many exciting ongoing research developments.

References

1. C. Ceroici and R. J. Zemp, "Large-Scale Nonlinear Lumped and Integrated Field Simulations of Top-Orthogonal-to-Bottom-Electrode CMUT Architectures," IEEE Trans. Ultrason. Ferroelectr. Freq. Control **64,** 1087-1091 (2017).

2. C. Ceroici, T. Harrison, and R. J. Zemp, "Fast Orthogonal Row–Column Electronic Scanning With Top-Orthogonal-to-Bottom Electrode Arrays," IEEE Trans. Ultrason. Ferroelectr. Freq. Control **64,** 1009-1014 (2017).

3. M. Maadi and R. J. Zemp, "Self and mutual radiation impedances for modeling of multi-frequency CMUT arrays," IEEE Trans. Ultrason. Ferroelectr. Freq. Control **63,** 1441-1454 (2016).

References

A. Agarwal, S. Huang, M. O'donnell, K. Day, M. Day, N. Kotov, and S. Ashkenazi, "Targeted gold nanorod contrast agent for prostate cancer detection by photoacoustic imaging," J. Appl. Phys. **102,** 064701 (2007).

D. Akai, T. Yogi, I. Kamja, Y. Numata, K. Ozaki, K. Sawada, N. Okada, K. Higuchi, and M. Ishida, "Miniature ultrasound acoustic imaging devices using 2-D pMUTs array on epitaxial PZT/SrRuO 3/Pt/^{3}-Al 2 O 3/Si structure," in *Solid-State Sensors, Actuators and Microsystems Conference (TRANSDUCERS), 2011 16th International,* Anonymous (IEEE, 2011), pp. 910-913.

D. Artemov, "Molecular magnetic resonance imaging with targeted contrast agents," J. Cell. Biochem. **90,** 518-524 (2003).

A. Austeng and S. Holm, "Sparse 2-D arrays for 3-D phased array imaging-design methods," IEEE Trans. Ultrason. Ferroelectr. Freq. Control **49,** 1073-1086 (2002).

T. Azuma, M. Ogihara, J. Kubota, A. Sasaki, S. Umemura, and H. Furuhata, "Dual-frequency ultrasound imaging and therapeutic bilaminar array using frequency selective isolation layer," IEEE Trans. Ultrason. Ferroelectr. Freq. Control **57,** 1211-1224 (2010).

G. Balasundaram, C. J. Ho, K. Li, W. Driessen, U. S. Dinish, C. L. Wong, V. Ntziachristos, B. Liu, and M. Olivo, "Molecular photoacoustic imaging of breast cancer using an actively targeted conjugated polymer," Int. J. Nanomedicine **10,** 387-397 (2015).

R. P. Baum and H. R. Kulkarni, "THERANOSTICS: From Molecular Imaging Using Ga-68 Labeled Tracers and PET/CT to Personalized Radionuclide Therapy - The Bad Berka Experience," Theranostics **2,** 437-447 (2012).

C. Bayram, S. Olcum, M. N. Senlik, and A. Atalar, "Bandwidth improvement in a cMUT array with mixed sized elements," in *Ultrasonics Symposium, 2005 IEEE,* Anonymous (IEEE, 2005), pp. 1956-1959.

D. Bellini and M. Z. Papiz, "Structure of a bacteriophytochrome and light-stimulated protomer swapping with a gene repressor," Structure **20,** 1436-1446 (2012).

H. Bouzari, M. Engholm, C. Beers, M. B. Stuart, S. I. Nikolov, E. V. Thomsen, and J. A. Jensen, "Curvilinear 3-D Imaging Using Row-Column-Addressed 2-D Arrays With a Diverging Lens: Feasibility Study," IEEE Trans. Ultrason. Ferroelectr. Freq. Control **64,** 978-988 (2017).

H. Brecht, R. Su, M. Fronheiser, S. A. Ermilov, A. Conjusteau, and A. A. Oraevsky, "Whole-body three-dimensional optoacoustic tomography system for small animals," J. Biomed. Opt. **14,** 064007-064007-8 (2009).

J. Brunker, J. Yao, J. Laufer, and S. E. Bohndiek, "Photoacoustic imaging using genetically encoded reporters: a review," J. Biomed. Opt. **22,** 070901 (2017).

J. Buchmann, J. Guggenheim, E. Zhang, C. Scharfenorth, B. Spannekrebs, C. Villringer, and J. Laufer, "Characterization and modeling of Fabry–Perot ultrasound sensors with hard dielectric mirrors for photoacoustic imaging," Appl. Opt. **56,** 5039-5046 (2017).

W. Cai and X. Chen, "Multimodality molecular imaging of tumor angiogenesis," J. Nucl. Med. **49 Suppl 2,** 113S-28S (2008).

S. Calmes, C. Cheng, F. Degertekin, X. Jin, S. Ergun, and B. Khuri-Yakub, "Highly integrated 2-D capacitive micromachined ultrasonic transducers," in *Ultrasonics Symposium, 1999. Proceedings. 1999 IEEE,* Anonymous (IEEE, 1999), pp. 1163-1166.

P. Caravan, "Protein-targeted gadolinium-based magnetic resonance imaging (MRI) contrast agents: design and mechanism of action," Acc. Chem. Res. **42,** 851-862 (2009).

P. Caravan, J. J. Ellison, T. J. McMurry, and R. B. Lauffer, "Gadolinium (III) chelates as MRI contrast agents: structure, dynamics, and applications," Chem. Rev. **99,** 2293-2352 (1999).

P. Carmeliet and R. K. Jain, "Molecular mechanisms and clinical applications of angiogenesis," Nature **473,** 298-307 (2011).

A. Caronti, G. Caliano, R. Carotenuto, A. Savoia, M. Pappalardo, E. Cianci, and V. Foglietti, "Capacitive micromachined ultrasonic transducer (CMUT) arrays for medical imaging," Microelectron. J. **37,** 770-777 (2006).

C. Ceroici, T. Harrison, and R. J. Zemp, "Fast Orthogonal Row–Column Electronic Scanning With Top-Orthogonal-to-Bottom Electrode Arrays," IEEE Trans. Ultrason. Ferroelectr. Freq. Control **64,** 1009-1014 (2017).

C. Ceroici and R. J. Zemp, "Large-Scale Nonlinear Lumped and Integrated Field Simulations of Top-Orthogonal-to-Bottom-Electrode CMUT Architectures," IEEE Trans. Ultrason. Ferroelectr. Freq. Control **64,** 1087-1091 (2017).

R. K. Chee, A. Sampaleanu, D. Rishi, and R. J. Zemp, "Top orthogonal to bottom electrode (TOBE) 2-D CMUT arrays for 3-D photoacoustic imaging," IEEE Trans. Ultrason. Ferroelectr. Freq. Control **61,** 1393-1395 (2014).

R. K. Chee, P. Zhang, M. Maadi, and R. J. Zemp, "Multifrequency Interlaced CMUTs for Photoacoustic Imaging," IEEE Trans. Ultrason. Ferroelectr. Freq. Control **64,** 391-401 (2017).

B. Chen, F. Chu, X. Liu, Y. Li, J. Rong, and H. Jiang, "AlN-based piezoelectric micromachined ultrasonic transducer for photoacoustic imaging," Appl. Phys. Lett. **103,** 031118 (2013).

I. Y. Chen and J. C. Wu, "Cardiovascular molecular imaging: focus on clinical translation," Circulation **123,** 425-443 (2011).

X. Cheng, J. Chen, and C. Li, "A miniature capacitive micromachined ultrasonic transducer array for minimally invasive photoacoustic imaging," J Microelectromech Syst **19,** 1002-1011 (2010).

S. Chou, Y. Shau, P. Wu, Y. Yang, D. Shieh, and C. Chen, "In vitro and in vivo studies of FePt nanoparticles for dual modal CT/MRI molecular imaging," J. Am. Chem. Soc. **132,** 13270-13278 (2010).

T. L. Christiansen, J. A. Jensen, and E. V. Thomsen, "Acoustical cross-talk in row–column addressed 2-D transducer arrays for ultrasound imaging," Ultrasonics **63,** 174-178 (2015).

T. L. Christiansen, M. F. Rasmussen, J. P. Bagge, L. N. Moesner, J. A. Jensen, and E. V. Thomsen, "3-D imaging using row–column-addressed arrays with integrated apodization—part II: Transducer fabrication and experimental results," IEEE Trans. Ultrason. Ferroelectr. Freq. Control **62,** 959-971 (2015).

D. M. Chudakov, S. Lukyanov, and K. A. Lukyanov, "Fluorescent proteins as a toolkit for in vivo imaging," Trends Biotechnol. **23,** 605-613 (2005).

R. S. Cobbold, *Foundations of biomedical ultrasound* (Oxford University Press, 2006).

B. Cox, J. G. Laufer, S. R. Arridge, and P. C. Beard, "Quantitative spectroscopic photoacoustic imaging: a review," J. Biomed. Opt. **17,** 0612021-06120222 (2012).

B. Cox and P. Beard, "Fast calculation of pulsed photoacoustic fields in fluids using k-space methods," J. Acoust. Soc. Am. **117,** 3616-3627 (2005).

L. Cunha, K. Szigeti, D. Mathé, and L. F. Metello, "The role of molecular imaging in modern drug development," Drug Discov. Today **19,** 936-948 (2014).

N. M. Daher and J. T. Yen, "2-D array for 3-D ultrasound imaging using synthetic aperture techniques," IEEE Trans. Ultrason. Ferroelectr. Freq. Control **53,** 912-924 (2006).

A. de La Zerda, Y. M. Paulus, R. Teed, S. Bodapati, Y. Dollberg, B. T. Khuri-Yakub, M. S. Blumenkranz, D. M. Moshfeghi, and S. S. Gambhir, "Photoacoustic ocular imaging," Opt. Lett. **35,** 270-272 (2010).

C. E. Demore, A. W. Joyce, K. Wall, and G. R. Lockwood, "Real-time volume imaging using a crossed electrode array," IEEE Trans. Ultrason. Ferroelectr. Freq. Control **56,** 1252-1261 (2009).

G. J. Diebold, M. I. Khan, and S. M. Park, "Photoacoustic "signatures" of particulate matter: optical production of acoustic monopole radiation," Science **250,** 101-104 (1990).

L. W. Dobrucki and A. J. Sinusas, "PET and SPECT in cardiovascular molecular imaging," Nature Reviews Cardiology **7,** 38 (2010).

V. S. Dogra, B. K. Chinni, K. S. Valluru, J. V. Joseph, A. Ghazi, J. L. Yao, K. Evans, E. M. Messing, and N. A. Rao, "Multispectral Photoacoustic Imaging of Prostate Cancer: Preliminary Ex-vivo Results," J. Clin. Imaging Sci. **3,** 41-7514.119139. eCollection 2013 (2013).

M. D. Eames, T. J. Reck, and J. A. Hossack, "Selectable frequency CMUT with membrane stand-off structures," in *Ultrasonics Symposium (IUS), 2009 IEEE International,* Anonymous (IEEE, 2009), pp. 2814-2817.

M. D. Eames, T. J. Reck, J. P. Kilroy, and J. A. Hossack, "FEA modeling of CMUT with membrane stand-off structures to enable selectable frequency-mode operation," IEEE Trans. Ultrason. Ferroelectr. Freq. Control **58,** (2011).

A. Egerton, M. A. Mehta, A. J. Montgomery, J. M. Lappin, O. D. Howes, S. J. Reeves, V. J. Cunningham, and P. M. Grasby, "The dopaminergic basis of human behaviors: a review of molecular imaging studies," Neuroscience & Biobehavioral Reviews **33,** 1109-1132 (2009).

S. Y. Emelianov, P. C. Li, and M. O'Donnell, "Photoacoustics for molecular imaging and therapy," Phys Today **62,** 34-39 (2009).

M. Engholm, H. Bouzari, T. L. Christiansen, C. Beers, J. P. Bagge, L. N. Moesner, S. E. Diederichsen, M. B. Stuart, J. A. Jensen, and E. V. Thomsen, "Probe development of CMUT and PZT row–column-addressed 2-D arrays," Sensors and Actuators A: Physical **273,** 121-133 (2018).

P. Ephrat, L. Keenlislide, A. Seabrook, F. S. Prato, and J. J. Carson, "Three-dimensional photoacoustic imaging by sparse-array detection and iterative image reconstruction," J. Biomed. Opt. **13,** 054052 (2008).

A. S. Ergun, G. G. Yaralioglu, and B. T. Khuri-Yakub, "Capacitive micromachined ultrasonic transducers: Theory and technology," J. Aerospace Eng. **16,** 76-84 (2003).

A. Erguri, Y. Huang, X. Zhuang, O. Oralkan, G. G. Yarahoglu, and B. T. Khuri-Yakub, "Capacitive micromachined ultrasonic transducers: Fabrication technology," IEEE Trans. Ultrason. Ferroelectr. Freq. Control **52,** 2242-2258 (2005).

D. Erritzoe, K. Holst, V. G. Frokjaer, C. L. Licht, J. Kalbitzer, F. A. Nielsen, C. Svarer, J. Madsen, and G. Knudsen, "A nonlinear relationship between cerebral serotonin transporter and 5-HT(2A) receptor binding: an in vivo molecular imaging study in humans," J. Neurosci. **30,** 3391-3397 (2010).

Q. Fan, K. Cheng, Z. Yang, R. Zhang, M. Yang, X. Hu, X. Ma, L. Bu, X. Lu, and X. Xiong, "Perylene-Diimide-Based Nanoparticles as Highly Efficient Photoacoustic Agents for Deep Brain Tumor Imaging in Living Mice," Adv Mater **27,** 843-847 (2015).

G. S. Filonov, A. Krumholz, J. Xia, J. Yao, L. V. Wang, and V. V. Verkhusha, "Deep-Tissue Photoacoustic Tomography of a Genetically Encoded Near-Infrared Fluorescent Probe," Angewandte Chemie International Edition **51,** 1448-1451 (2012).

G. S. Filonov, K. D. Piatkevich, L. Ting, J. Zhang, K. Kim, and V. V. Verkhusha, "Bright and stable near-infrared fluorescent protein for in vivo imaging," Nat. Biotechnol. **29,** 757-761 (2011).

J. Folkman, "Angiogenesis: an organizing principle for drug discovery?" Nature reviews Drug discovery **6,** (2007).

M. Fromant, S. Blanquet, and P. Plateau, "Direct random mutagenesis of gene-sized DNA fragments using polymerase chain reaction," Anal. Biochem. **224,** 347-353 (1995).

S. S. Gambhir, "Molecular imaging of cancer with positron emission tomography," Nature Reviews Cancer **2,** 683 (2002).

J. Gamelin, A. Maurudis, A. Aguirre, F. Huang, P. Guo, L. V. Wang, and Q. Zhu, "A real-time photoacoustic tomography system for small animals," Optics express **17,** 10489-10498 (2009).

R. C. Gessner, C. B. Frederick, F. S. Foster, and P. A. Dayton, "Acoustic angiography: a new imaging modality for assessing microvasculature architecture," Journal of Biomedical Imaging **2013,** 14 (2013).

R. Gessner, M. Lukacs, M. Lee, E. Cherin, F. S. Foster, and P. A. Dayton, "High-resolution, high-contrast ultrasound imaging using a prototype dual-frequency transducer: in vitro and in vivo studies," IEEE Trans. Ultrason. Ferroelectr. Freq. Control **57,** 1772-1781 (2010).

C. M. Gomes, A. J. Abrunhosa, P. Ramos, and E. K. Pauwels, "Molecular imaging with SPECT as a tool for drug development," Adv. Drug Deliv. Rev. **63,** 547-554 (2011).

B. A. Greenlay and R. J. Zemp, "Fabrication of linear array and top-orthogonal-to-bottom electrode cmut arrays with a sacrificial release process," IEEE Trans. Ultrason. Ferroelectr. Freq. Control **64,** 93-107 (2017).

S. Gross and D. Piwnica-Worms, "Spying on cancer: molecular imaging in vivo with genetically encoded reporters," Cancer cell **7,** 5-15 (2005).

A. Guiroy, A. Novell, E. Ringgaard, R. Lou-Moeller, J. Gregoire, A. Abellard, T. Zawada, A. Bouakaz, and F. Levassort, "Dual-frequency transducer for nonlinear contrast agent imaging," IEEE Trans. Ultrason. Ferroelectr. Freq. Control **60,** 2634-2644 (2013).

G. Haddad, P. Zhabyeyev, M. Farhan, L. F. Zhu, Z. Kassiri, D. C. Rayner, B. Vanhaesebroeck, G. Y. Oudit, and A. G. Murray, "Phosphoinositide 3-kinase beta mediates microvascular endothelial repair of thrombotic microangiopathy," Blood **124,** 2142-2149 (2014).

P. Hajireza, J. Sorge, M. Brett, and R. Zemp, "In vivo optical resolution photoacoustic microscopy using glancing angle-deposited nanostructured Fabry–Perot etalons," Opt. Lett. **40,** 1350-1353 (2015).

M. I. Haller and B. T. Khuri-Yakub, "A surface micromachined electrostatic ultrasonic air transducer," IEEE Trans. Ultrason. Ferroelectr. Freq. Control **43,** 1-6 (1996).

M. Heijblom, D. Piras, W. Xia, J. C. van Hespen, J. Klaase, F. Van den Engh, T. Van Leeuwen, W. Steenbergen, and S. Manohar, "Visualizing breast cancer using the Twente photoacoustic mammoscope: what do we learn from twelve new patient measurements?" Optics express **20,** 11582-11597 (2012).

M. Heijblom, W. Steenbergen, and S. Manohar, "Clinical photoacoustic breast imaging: the twente experience." IEEE pulse **6,** 42-46 (2015).

A. Hellebust and R. Richards-Kortum, "Advances in molecular imaging: targeted optical contrast agents for cancer diagnostics," Nanomedicine **7,** 429-445 (2012).

I. J. Hildebrandt and S. S. Gambhir, "Molecular imaging applications for immunology," Clinical immunology **111,** 210-224 (2004).

S. Holbek, T. L. Christiansen, M. B. Stuart, C. Beers, E. V. Thomsen, and J. A. Jensen, "3-D Vector Flow Estimation With Row–Column-Addressed Arrays," IEEE Trans. Ultrason. Ferroelectr. Freq. Control **63,** 1799-1814 (2016).

S. Holbek, C. Ewertsen, H. Bouzari, M. J. Pihl, K. L. Hansen, M. B. Stuart, C. Thomsen, M. B. Nielsen, and J. A. Jensen, "Ultrasonic 3-D vector flow method for quantitative in vivo peak velocity and flow rate estimation," IEEE Trans. Ultrason. Ferroelectr. Freq. Control **64,** 544-554 (2017).

K. A. Homan, M. Souza, R. Truby, G. P. Luke, C. Green, E. Vreeland, and S. Emelianov, "Silver nanoplate contrast agents for in vivo molecular photoacoustic imaging," ACS nano **6,** 641-650 (2012).

S. Hu, K. Maslov, and L. V. Wang, "Second-generation optical-resolution photoacoustic microscopy with improved sensitivity and speed," Opt. Lett. **36,** 1134-1136 (2011).

Z. Hu, X. Wang, Q. Liu, and Y. Paulus, "Photoacoustic imaging in ophthalmology," Int J Ophthalmol Eye Res **3,** 126-132 (2015).

Y. Huang, A. S. Ergun, E. Haeggstrom, M. H. Badi, and B. T. Khuri-Yakub, "Fabricating capacitive micromachined ultrasonic transducers with wafer-bonding technology," J Microelectromech Syst **12,** 128-137 (2003).

T. Hussain and Q. T. Nguyen, "Molecular imaging for cancer diagnosis and surgery," Adv. Drug Deliv. Rev. **66,** 90-100 (2014).

N. Huynh, F. Lucka, E. Zhang, M. Betcke, S. Arridge, P. Beard, and B. Cox, "Sub-sampled Fabry-Perot photoacoustic scanner for fast 3D imaging," in *Photons Plus Ultrasound: Imaging and Sensing 2017,* Anonymous (International Society for Optics and Photonics, 2017), pp. 100641Y.

F. A. Jaffer and R. Weissleder, "Molecular imaging in the clinical arena," JAMA **293,** 855-862 (2005).

M. L. James and S. S. Gambhir, "A molecular imaging primer: modalities, imaging agents, and applications," Physiol. Rev. **92,** 897-965 (2012).

K. Jansen, Van Der Steen, Antonius FW, H. M. van Beusekom, J. W. Oosterhuis, and G. van Soest, "Intravascular photoacoustic imaging of human coronary atherosclerosis," Opt. Lett. **36,** 597-599 (2011).

K. Jansen, van der Steen, Antonius FW, M. Wu, H. M. van Beusekom, G. Springeling, X. Li, Q. Zhou, K. K. Shung, D. P. de Kleijn, and G. van Soest, "Spectroscopic intravascular photoacoustic imaging of lipids in atherosclerosis," J. Biomed. Opt. **19,** 026006 (2014).

K. Jansen, M. Wu, van der Steen, Antonius FW, and G. van Soest, "Photoacoustic imaging of human coronary atherosclerosis in two spectral bands," Photoacoustics **2,** 12-20 (2014).

A. P. Jathoul, J. Laufer, O. Ogunlade, B. Treeby, B. Cox, E. Zhang, P. Johnson, A. R. Pizzey, B. Philip, and T. Marafioti, "Deep in vivo photoacoustic imaging of mammalian tissues using a tyrosinase-based genetic reporter," Nature Photonics **9,** 239 (2015).

J. A. Jensen, "Field: A program for simulating ultrasound systems," in *10TH NORDICBALTIC CONFERENCE ON BIOMEDICAL IMAGING, VOL. 4, SUPPLEMENT 1, PART 1: 351--353,* Anonymous (Citeseer, 1996).

J. A. Jensen and N. B. Svendsen, "Calculation of pressure fields from arbitrarily shaped, apodized, and excited ultrasound transducers," IEEE Trans. Ultrason. Ferroelectr. Freq. Control **39,** 262-267 (1992).

G. Jiménez-Valerio, M. Martínez-Lozano, N. Bassani, A. Vidal, M. Ochoa-de-Olza, C. Suárez, X. García-del-Muro, J. Carles, F. Viñals, and M. Graupera, "Resistance to antiangiogenic therapies by metabolic symbiosis in renal cell carcinoma PDX models and patients," Cell reports **15,** 1134-1143 (2016).

X. Jin, I. Ladabaum, F. L. Degertekin, S. Calmes, and B. T. Khuri-Yakub, "Fabrication and characterization of surface micromachined capacitive ultrasonic immersion transducers," J Microelectromech Syst **8,** 100-114 (1999).

X. Jin, I. Ladabaum, and B. T. Khuri-Yakub, "The microfabrication of capacitive ultrasonic transducers," J Microelectromech Syst **7,** 295-302 (1998).

S. Katzir, "The discovery of the piezoelectric effect," Archive for history of exact sciences **57,** 61-91 (2003).

C. Kim, T. N. Erpelding, L. Jankovic, M. D. Pashley, and L. V. Wang, "Deeply penetrating in vivo photoacoustic imaging using a clinical ultrasound array system," Biomedical optics express **1,** 278-284 (2010).

J. Kim, E. I. Galanzha, E. V. Shashkov, H. Moon, and V. P. Zharov, "Golden carbon nanotubes as multimodal photoacoustic and photothermal high-contrast molecular agents," Nature nanotechnology **4,** 688 (2009).

T. Knöpfel, J. Díez-García, and W. Akemann, "Optical probing of neuronal circuit dynamics: genetically encoded versus classical fluorescent sensors," Trends Neurosci. **29,** 160-166 (2006).

K. P. Köstli and P. C. Beard, "Two-dimensional photoacoustic imaging by use of Fourier-transform image reconstruction and a detector with an anisotropic response," Appl. Opt. **42,** 1899-1908 (2003).

K. P. Köstli, M. Frenz, H. Bebie, and H. P. Weber, "Temporal backward projection of optoacoustic pressure transients using Fourier transform methods," Physics in Medicine & Biology **46,** 1863 (2001).

S. Kothapalli, T. Ma, S. Vaithilingam, Ö Oralkan, B. T. Khuri-Yakub, and S. S. Gambhir, "Deep tissue photoacoustic imaging using a miniaturized 2-D capacitive micromachined ultrasonic transducer array," IEEE Transactions on Biomedical Engineering **59,** 1199-1204 (2012).

R. A. Kruger, C. M. Kuzmiak, R. B. Lam, D. R. Reinecke, S. P. Del Rio, and D. Steed, "Dedicated 3D photoacoustic breast imaging," Med. Phys. **40,** (2013).

A. Krumholz, D. M. Shcherbakova, J. Xia, L. V. Wang, and V. V. Verkhusha, "Multicontrast photoacoustic in vivo imaging using near-infrared fluorescent proteins," Sci. Rep. **4,** 3939 (2014).

G. Ku and L. V. Wang, "Deeply penetrating photoacoustic tomography in biological tissues enhanced with an optical contrast agent," Opt. Lett. **30,** 507-509 (2005).

G. Ku, X. Wang, G. Stoica, and L. V. Wang, "Multiple-bandwidth photoacoustic tomography," Physics in Medicine & Biology **49,** 1329 (2004).

M. Kupnik, M. Ho, S. Vaithilingam, and B. T. Khuri-Yakub, "CMUTs for air coupled ultrasound with improved bandwidth," in *Ultrasonics Symposium (IUS), 2011 IEEE International,* Anonymous (IEEE, 2011), pp. 592-595.

I. Ladabaum, X. Jin, H. T. Soh, A. Atalar, and B. Khuri-Yakub, "Surface micromachined capacitive ultrasonic transducers," IEEE Trans. Ultrason. Ferroelectr. Freq. Control **45,** 678-690 (1998).

K. Latham, C. Samson, C. Ceroici, R. J. Zemp, and J. A. Brown, "Fabrication and performance of a 128-element crossed-electrode relaxor array, for a novel 3D imaging approach," in *Ultrasonics Symposium (IUS), 2017 IEEE International,* Anonymous (IEEE, 2017), pp. 1-4.

J. Laufer, D. Delpy, C. Elwell, and P. Beard, "Quantitative spatially resolved measurement of tissue chromophore concentrations using photoacoustic spectroscopy: application to the measurement of blood oxygenation and haemoglobin concentration," Phys. Med. Biol. **52,** 141 (2006).

H. W. Lee, P. Gangadaran, S. Kalimuthu, and B. Ahn, "Advances in molecular imaging strategies for in vivo tracking of immune cells," BioMed research international **2016,** (2016).

J. Lee, Y. Huh, Y. Jun, J. Seo, J. Jang, H. Song, S. Kim, E. Cho, H. Yoon, and J. Suh, "Artificially engineered magnetic nanoparticles for ultra-sensitive molecular imaging," Nat. Med. **13,** 95 (2007).

C. S. Levin, "Primer on molecular imaging technology," European journal of nuclear medicine and molecular imaging **32,** S325-S345 (2005).

C. Li, G. S. Mitchell, J. Dutta, S. Ahn, R. M. Leahy, and S. R. Cherry, "A three-dimensional multispectral fluorescence optical tomography imaging system for small animals based on a conical mirror design," Optics express **17,** 7571-7585 (2009).

L. Li, R. J. Zemp, G. F. Lungu, G. Stoica, and L. V. Wang, "Photoacoustic imaging of lacZ gene expression in vivo," J. Biomed. Opt. **12,** 020504 (2007).

P. Li, C. C. Wang, D. Shieh, C. Wei, C. Liao, C. Poe, S. Jhan, A. Ding, and Y. Wu, "In vivo photoacoustic molecular imaging with simultaneous multiple selective targeting using antibody-conjugated gold nanorods," Optics Express **16,** 18605-18615 (2008).

Y. Li, A. Forbrich, J. Wu, P. Shao, R. E. Campbell, and R. Zemp, "Engineering Dark Chromoprotein Reporters for Photoacoustic Microscopy and FRET Imaging," Sci. Rep. **6,** 22129 (2016).

W. Liao, W. Liu, J. Rogers, F. Usmani, Y. Tang, B. Wang, H. Jiang, and H. Xie, "Piezeoelectric micromachined ultrasound tranducer array for photoacoustic imaging," in *Solid-State Sensors,* *Actuators and Microsystems (TRANSDUCERS & EUROSENSORS XXVII), 2013 Transducers & Eurosensors XXVII: The 17th International Conference on,* Anonymous (IEEE, 2013), pp. 1831-1834.

C. Liu, X. Gong, R. Lin, F. Liu, J. Chen, Z. Wang, L. Song, and J. Chu, "Advances in imaging techniques and genetically encoded probes for photoacoustic imaging," Theranostics **6,** 2414 (2016).

A. S. Logan, L. L. Wong, and J. T. Yeow, "2-D CMUT wafer bonded imaging arrays with a row-column addressing scheme," in *Ultrasonics Symposium (IUS), 2009 IEEE International,* Anonymous (IEEE, 2009), pp. 984-987.

A. S. Logan, L. L. Wong, A. I. Chen, and J. T. Yeow, "A 32 x 32 element row-column addressed capacitive micromachined ultrasonic transducer," IEEE Trans. Ultrason. Ferroelectr. Freq. Control **58,** 1266-1271 (2011).

G. P. Luke, S. Y. Nam, and S. Y. Emelianov, "Optical wavelength selection for improved spectroscopic photoacoustic imaging," Photoacoustics **1,** 36-42 (2013).

J. Ma, K. H. Martin, P. A. Dayton, and X. Jiang, "A preliminary engineering design of intravascular dual-frequency transducers for contrast-enhanced acoustic angiography and molecular imaging," IEEE Trans. Ultrason. Ferroelectr. Freq. Control **61,** 870-880 (2014).

M. Maadi and R. J. Zemp, "Self and mutual radiation impedances for modeling of multi-frequency CMUT arrays," IEEE Trans. Ultrason. Ferroelectr. Freq. Control **63,** 1441-1454 (2016).

S. Mallidi, T. Larson, J. Aaron, K. Sokolov, and S. Emelianov, "Molecular specific optoacoustic imaging with plasmonic nanoparticles," Optics Express **15,** 6583-6588 (2007).

S. Mallidi, T. Larson, J. Tam, P. P. Joshi, A. Karpiouk, K. Sokolov, and S. Emelianov, "Multiwavelength photoacoustic imaging and plasmon resonance coupling of gold nanoparticles for selective detection of cancer," Nano letters **9,** 2825-2831 (2009).

S. Mallidi, G. P. Luke, and S. Emelianov, "Photoacoustic imaging in cancer detection, diagnosis, and treatment guidance," Trends Biotechnol. **29,** 213-221 (2011).

K. Maslov, H. F. Zhang, S. Hu, and L. V. Wang, "Optical-resolution photoacoustic microscopy for in vivo imaging of single capillaries," Opt. Lett. **33,** 929-931 (2008).

W. P. Mason, "Piezoelectricity, its history and applications," J. Acoust. Soc. Am. **70,** 1561-1566 (1981).

T. F. Massoud and S. S. Gambhir, "Molecular imaging in living subjects: seeing fundamental biological processes in a new light," Genes Dev. **17,** 545-580 (2003).

M. Mehrmohammadi, S. Joon Yoon, D. Yeager, and S. Y Emelianov, "Photoacoustic imaging for cancer detection and staging," Current molecular imaging **2,** 89-105 (2013).

M. Moothanchery and M. Pramanik, "Performance Characterization of a Switchable Acoustic Resolution and Optical Resolution Photoacoustic Microscopy System," Sensors **17,** 357 (2017).

C. E. Morton and G. R. Lockwood, "Theoretical assessment of a crossed electrode 2-D array for 3-D imaging," in *Ultrasonics, 2003 IEEE Symposium on,* Anonymous (IEEE, 2003), pp. 968-971.

R. Narikawa, T. Ishizuka, N. Muraki, T. Shiba, G. Kurisu, and M. Ikeuchi, "Structures of cyanobacteriochromes from phototaxis regulators AnPixJ and TePixJ reveal general and specific photoconversion mechanism," Proc. Natl. Acad. Sci. U. S. A. **110,** 918-923 (2013).

R. Narikawa, T. Nakajima, Y. Aono, K. Fushimi, G. Enomoto, Ni-Ni-Win, S. Itoh, M. Sato, and M. Ikeuchi, "A biliverdin-binding cyanobacteriochrome from the chlorophyll d-bearing cyanobacterium Acaryochloris marina," Sci. Rep. **5,** 7950 (2015).

J. Oh, M. Li, H. F. Zhang, K. Maslov, and L. V. Wang, "Three-dimensional imaging of skin melanoma in vivo by dual-wavelength photoacoustic microscopy," J. Biomed. Opt. **11,** 034032 (2006).

S. Olcum, A. Atalar, H. Koymen, and M. N. Senlik, "P3R-4 stagger tuned cMUT array for wideband airborne applications," in *Ultrasonics Symposium, 2006. IEEE,* Anonymous (IEEE, 2006), pp. 2377-2380.

O. Oralkan, A. S. Ergun, C. Cheng, J. A. Johnson, M. Karaman, T. H. Lee, and B. T. Khuri-Yakub, "Volumetric ultrasound imaging using 2-D CMUT arrays," IEEE Trans. Ultrason. Ferroelectr. Freq. Control **50,** 1581-1594 (2003).

O. Oralkan, A. S. Ergun, J. A. Johnson, M. Karaman, U. Demirci, K. Kaviani, T. H. Lee, and B. T. Khuri-Yakub, "Capacitive micromachined ultrasonic transducers: Next-generation arrays for acoustic imaging?" IEEE Trans. Ultrason. Ferroelectr. Freq. Control **49,** 1596-1610 (2002).

A. E. Palmer, Y. Qin, J. G. Park, and J. E. McCombs, "Design and application of genetically encoded biosensors," Trends Biotechnol. **29,** 144-152 (2011).

D. Pan, M. Pramanik, A. Senpan, X. Yang, K. H. Song, M. J. Scott, H. Zhang, P. J. Gaffney, S. A. Wickline, and L. V. Wang, "Molecular photoacoustic tomography with colloidal nanobeacons," Angewandte Chemie International Edition **48,** 4170-4173 (2009).

D. Pan, E. Roessl, J. Schlomka, S. D. Caruthers, A. Senpan, M. J. Scott, J. S. Allen, H. Zhang, G. Hu, and P. J. Gaffney, "Computed Tomography in Color: NanoK-Enhanced Spectral CT Molecular Imaging," Angewandte Chemie **122,** 9829-9833 (2010).

D. Pan, M. Pramanik, A. Senpan, J. S. Allen, H. Zhang, S. A. Wickline, L. V. Wang, and G. M. Lanza, "Molecular photoacoustic imaging of angiogenesis with integrin-targeted gold nanobeacons," FASEB J. **25,** 875-882 (2011).

M. E. Phelps, "Positron emission tomography provides molecular imaging of biological processes," Proceedings of the National Academy of Sciences **97,** 9226-9233 (2000).

D. Piras, W. Xia, W. Steenbergen, T. G. van Leeuwen, and S. Manohar, "Photoacoustic imaging of the breast using the twente photoacoustic mammoscope: present status and future perspectives," IEEE Journal of Selected Topics in Quantum Electronics **16,** 730-739 (2010).

A. A. Plumb, N. T. Huynh, J. Guggenheim, E. Zhang, and P. Beard, "Rapid volumetric photoacoustic tomographic imaging with a Fabry-Perot ultrasound sensor depicts peripheral arteries and microvascular vasomotor responses to thermal stimuli," Eur. Radiol.1-9 (2017).

M. G. Pomper, "Molecular imaging: an overview," Acad. Radiol. **8,** 1141-1153 (2001).

R. Popovtzer, A. Agrawal, N. A. Kotov, A. Popovtzer, J. Balter, T. E. Carey, and R. Kopelman, "Targeted gold nanoparticles enable molecular CT imaging of cancer," Nano letters **8,** 4593-4596 (2008).

K. Pu, A. J. Shuhendler, J. V. Jokerst, J. Mei, S. S. Gambhir, Z. Bao, and J. Rao, "Semiconducting polymer nanoparticles as photoacoustic molecular imaging probes in living mice," Nature nanotechnology **9,** 233-239 (2014).

M. A. Pysz, S. S. Gambhir, and J. K. Willmann, "Molecular imaging: current status and emerging strategies," Clin. Radiol. **65,** 500-516 (2010).

E. L. Que, D. W. Domaille, and C. J. Chang, "Metals in neurobiology: probing their chemistry and biology with molecular imaging," Chem. Rev. **108,** 1517-1549 (2008).

M. F. Rasmussen, T. L. Christiansen, E. V. Thomsen, and J. A. Jensen, "3-D imaging using row-column-addressed arrays with integrated apodization-part i: apodization design and line element beamforming," IEEE Trans. Ultrason. Ferroelectr. Freq. Control **62,** 947-958 (2015).

D. Razansky, A. Buehler, and V. Ntziachristos, "Volumetric real-time multispectral optoacoustic tomography of biomarkers," Nature protocols **6,** 1121 (2011).

D. Razansky, C. Vinegoni, and V. Ntziachristos, "Multispectral photoacoustic imaging of fluorochromes in small animals," Opt. Lett. **32,** 2891-2893 (2007).

B. I. Rini and M. B. Atkins, "Resistance to targeted therapy in renal-cell carcinoma," The lancet oncology **10,** 992-1000 (2009).

E. A. Rodriguez, G. N. Tran, L. A. Gross, J. L. Crisp, X. Shu, J. Y. Lin, and R. Y. Tsien, "A far-red fluorescent protein evolved from a cyanobacterial phycobiliprotein," Nature methods **13,** 763-769 (2016).

A. Rosenthal, V. Ntziachristos, and D. Razansky, "Model-based optoacoustic inversion with arbitrary-shape detectors," Med. Phys. **38,** 4285-4295 (2011).

A. Rosenthal, D. Razansky, and V. Ntziachristos, "Fast semi-analytical model-based acoustic inversion for quantitative optoacoustic tomography," IEEE Trans. Med. Imaging **29,** 1275-1285 (2010).

M. Rudin and R. Weissleder, "Molecular imaging in drug discovery and development," Nature reviews Drug discovery **2,** 123-131 (2003).

J. Sambrook, E. F. Fritsch, and T. Maniatis, *Molecular cloning: a laboratory manual.* (Cold spring harbor laboratory press, 1989).

A. Sampaleanu, P. Zhang, A. Kshirsagar, W. Moussa, and R. Zemp, "Top-orthogonal-to-bottom-electrode (TOBE) CMUT arrays for 3-D ultrasound imaging," IEEE Trans. Ultrason. Ferroelectr. Freq. Control **61,** 266-276 (2014).

A. Saraste, S. G. Nekolla, and M. Schwaiger, "Cardiovascular molecular imaging: an overview," Cardiovasc. Res. **83,** 643-652 (2009).

C. H. Seo and J. T. Yen, "A 256 x 256 2-D array transducer with row-column addressing for 3-D rectilinear imaging," IEEE Trans. Ultrason. Ferroelectr. Freq. Control **56,** (2009).

S. Sethuraman, J. H. Amirian, S. H. Litovsky, R. W. Smalling, and S. Y. Emelianov, "Spectroscopic intravascular photoacoustic imaging to differentiate atherosclerotic plaques," Optics express **16,** 3362-3367 (2008).

P. Shao, B. Cox, and R. J. Zemp, "Estimating optical absorption, scattering, and Grueneisen distributions with multiple-illumination photoacoustic tomography," Appl. Opt. **50,** 3145-3154 (2011).

D. M. Shcherbakova and V. V. Verkhusha, "Near-infrared fluorescent proteins for multicolor in vivo imaging," Nature methods **10,** 751-754 (2013).

D. Shcherbo, E. M. Merzlyak, T. V. Chepurnykh, A. F. Fradkov, G. V. Ermakova, E. A. Solovieva, K. A. Lukyanov, E. A. Bogdanova, A. G. Zaraisky, and S. Lukyanov, "Bright far-red fluorescent protein for whole-body imaging," Nature methods **4,** 741-746 (2007).

X. Shu, A. Royant, M. Z. Lin, T. A. Aguilera, V. Lev-Ram, P. A. Steinbach, and R. Y. Tsien, "Mammalian expression of infrared fluorescent proteins engineered from a bacterial phytochrome," Science **324,** 804-807 (2009).

S. W. Smith, R. E. Davidsen, C. D. Emery, R. L. Goldberg, and E. D. Light, "Update on 2-D array transducers for medical ultrasound," in *Ultrasonics Symposium, 1995. Proceedings., 1995 IEEE,* Anonymous (IEEE, 1995), pp. 1273-1278.

J. Sorensen, D. Sandberg, M. Sandstrom, A. Wennborg, J. Feldwisch, V. Tolmachev, G. Astrom, M. Lubberink, U. Garske-Roman, J. Carlsson, and H. Lindman, "First-in-human molecular imaging of HER2 expression in breast cancer metastases using the 111In-ABY-025 affibody molecule," J. Nucl. Med. **55,** 730-735 (2014).

D. N. Stephens, D. E. Kruse, A. S. Ergun, S. Barnes, X. M. Lu, and K. W. Ferrara, "Efficient array design for sonotherapy," Physics in Medicine & Biology **53,** 3943 (2008).

A. C. Stiel, X. L. Deán-Ben, Y. Jiang, V. Ntziachristos, D. Razansky, and G. G. Westmeyer, "High-contrast imaging of reversibly switchable fluorescent proteins via temporally unmixed multispectral optoacoustic tomography," Opt. Lett. **40,** 367-370 (2015).

J. L. Su, B. Wang, K. E. Wilson, C. L. Bayer, Y. Chen, S. Kim, K. A. Homan, and S. Y. Emelianov, "Advances in clinical and biomedical applications of photoacoustic imaging," Expert opinion on medical diagnostics **4,** 497-510 (2010).

F. V. Subach, L. Zhang, T. W. Gadella, N. G. Gurskaya, K. A. Lukyanov, and V. V. Verkhusha, "Red fluorescent protein with reversibly photoswitchable absorbance for photochromic FRET," Chem. Biol. **17,** 745-755 (2010).

T. L. Szabo, *Diagnostic ultrasound imaging: inside out* (Academic Press, 2004).

G. Themelis, J. S. Yoo, K. Soh, R. B. Schulz, and V. Ntziachristos, "Real-time intraoperative fluorescence imaging system using light-absorption correction," J. Biomed. Opt. **14,** 064012 (2009).

S. Vaithilingam, T. Ma, Y. Furukawa, I. O. Wygant, X. Zhuang, A. De La Zerda, O. Oralkan, A. Kamaya, R. B. Jeffrey, and B. T. Khuri-yakub, "Three-dimensional photoacoustic imaging using a two-dimensional CMUT array," IEEE Trans. Ultrason. Ferroelectr. Freq. Control **56,** 2411-2419 (2009).

K. S. Valluru, K. E. Wilson, and J. K. Willmann, "Photoacoustic Imaging in oncology: translational preclinical and early clinical experience," Radiology **280,** 332-349 (2016).

B. Vanhaesebroeck, J. Guillermet-Guibert, M. Graupera, and B. Bilanges, "The emerging mechanisms of isoform-specific PI3K signalling," Nature reviews Molecular cell biology **11,** 329-341 (2010).

J. Vernet, W. Steichen, R. Lardat, O. Garcia, and J. Gelly, "PMUTS design optimization for medical probes applications," in *Ultrasonics Symposium, 2001 IEEE,* Anonymous (IEEE, 2001), pp. 899-902.

L. V. Wang, "Tutorial on photoacoustic microscopy and computed tomography," IEEE Journal of Selected Topics in Quantum Electronics **14,** 171-179 (2008).

L. V. Wang and H. Wu, *Biomedical optics: principles and imaging* (John Wiley & Sons, 2012).

L. V. Wang and J. Yao, "A practical guide to photoacoustic tomography in the life sciences," Nature methods **13,** 627 (2016).

X. Wang, W. W. Roberts, P. L. Carson, D. P. Wood, and J. B. Fowlkes, "Photoacoustic tomography: a potential new tool for prostate cancer," Biomedical optics express **1,** 1117-1126 (2010).

X. Wang, X. Xie, G. Ku, L. V. Wang, and G. Stoica, "Noninvasive imaging of hemoglobin concentration and oxygenation in the rat brain using high-resolution photoacoustic tomography," J. Biomed. Opt. **11,** 024015 (2006).

Y. Wang, J. Xia, and L. V. Wang, "Deep-tissue photoacoustic tomography of Förster resonance energy transfer," J. Biomed. Opt. **18,** 101316-101316 (2013).

B. Wang, A. Karpiouk, D. Yeager, J. Amirian, S. Litovsky, R. Smalling, and S. Emelianov, "In vivo intravascular ultrasound-guided photoacoustic imaging of lipid in plaques using an animal model of atherosclerosis," Ultrasound Med. Biol. **38,** 2098-2103 (2012).

L. V. Wang and S. Hu, "Photoacoustic tomography: in vivo imaging from organelles to organs," Science **335,** 1458-1462 (2012).

Y. X. Wang, "Superparamagnetic iron oxide based MRI contrast agents: Current status of clinical application," Quant. Imaging Med. Surg. **1,** 35-40 (2011).

R. Weissleder, "Molecular imaging in cancer," Science **312,** 1168-1171 (2006).

R. Weissleder and M. J. Pittet, "Imaging in the era of molecular oncology," Nature **452,** 580-589 (2008).

J. K. Willmann, N. van Bruggen, L. M. Dinkelborg, and S. S. Gambhir, "Molecular imaging in drug development," Nature Reviews Drug Discovery **7,** 591-607 (2008).

K. E. Wilson, S. V. Bachawal, L. Abou-Elkacem, K. Jensen, S. Machtaler, L. Tian, and J. K. Willmann, "Spectroscopic Photoacoustic Molecular Imaging of Breast Cancer using a B7-H3-targeted ICG Contrast Agent," Theranostics **7,** 1463 (2017).

K. E. Wilson, S. V. Bachawal, L. Tian, and J. K. Willmann, "Multiparametric spectroscopic photoacoustic imaging of breast cancer development in a transgenic mouse model," Theranostics **4,** 1062-1071 (2014).

L. L. Wong, A. I. Chen, Z. Li, A. S. Logan, and J. T. Yeow, "A row–column addressed micromachined ultrasonic transducer array for surface scanning applications," Ultrasonics **54,** 2072-2080 (2014).

I. O. Wygant, X. Zhuang, D. T. Yeh, O. Oralkan, A. S. Ergun, M. Karaman, and B. T. Khuri-Yakub, "Integration of 2D CMUT arrays with front-end electronics for volumetric ultrasound imaging," IEEE Trans. Ultrason. Ferroelectr. Freq. Control **55,** (2008).

L. Xi, S. R. Grobmyer, L. Wu, R. Chen, G. Zhou, L. G. Gutwein, J. Sun, W. Liao, Q. Zhou, and H. Xie, "Evaluation of breast tumor margins in vivo with intraoperative photoacoustic imaging," Optics express **20,** 8726-8731 (2012).

J. Xia, M. R. Chatni, K. I. Maslov, Z. Guo, K. Wang, M. A. Anastasio, and L. V. Wang, "Whole-body ring-shaped confocal photoacoustic computed tomography of small animals in vivo," J. Biomed. Opt. **17,** 050506 (2012).

J. Xia and L. V. Wang, "Small-animal whole-body photoacoustic tomography: a review," IEEE Transactions on Biomedical Engineering **61,** 1380-1389 (2014).

C. Xu, P. D. Kumavor, U. S. Alqasemi, H. Li, Y. Xu, S. Zanganeh, and Q. Zhu, "Indocyanine green enhanced co-registered diffuse optical tomography and photoacoustic tomography," J. Biomed. Opt. **18,** 126006 (2013).

G. Xu, Y. Xue, Z. G. Özkurt, N. Slimani, Z. Hu, X. Wang, K. Xia, T. Ma, Q. Zhou, and H. Demirci, "Photoacoustic imaging features of intraocular tumors: Retinoblastoma and uveal melanoma," PloS one **12,** e0170752 (2017).

M. Xu and L. V. Wang, "Universal back-projection algorithm for photoacoustic computed tomography," Physical Review E **71,** 016706 (2005).

Y. Xu and L. V. Wang, "Time reversal and its application to tomography with diffracting sources," Phys. Rev. Lett. **92,** 033902 (2004).

J. Yao, A. A. Kaberniuk, L. Li, D. M. Shcherbakova, R. Zhang, L. Wang, G. Li, V. V. Verkhusha, and L. V. Wang, "Multiscale photoacoustic tomography using reversibly switchable bacterial phytochrome as a near-infrared photochromic probe," Nature methods **13,** 67-73 (2016).

D. T. Yeh, O. Oralkan, I. O. Wygant, M. O'Donnell, and B. T. Khuri-Yakub, "3-D ultrasound imaging using a forward-looking CMUT ring array for intravascular/intracardiac applications," IEEE Trans. Ultrason. Ferroelectr. Freq. Control **53,** 1202-1211 (2006).

J. T. Yen, J. P. Steinberg, and S. W. Smith, "Sparse 2-D array design for real time rectilinear volumetric imaging," IEEE Trans. Ultrason. Ferroelectr. Freq. Control **47,** 93-110 (2000).

D. Yu, M. A. Baird, J. R. Allen, E. S. Howe, M. P. Klassen, A. Reade, K. Makhijani, Y. Song, S. Liu, and Z. Murthy, "A naturally monomeric infrared fluorescent protein for protein labeling in vivo," Nature methods **12,** 763-765 (2015).

R. J. Zemp, "Quantitative photoacoustic tomography with multiple optical sources," Appl. Opt. **49,** 3566-3572 (2010).

A. d. l. Zerda, Z. Liu, S. Bodapati, R. Teed, S. Vaithilingam, B. T. Khuri-Yakub, X. Chen, H. Dai, and S. S. Gambhir, "Ultrahigh sensitivity carbon nanotube agents for photoacoustic molecular imaging in living mice," Nano letters **10,** 2168-2172 (2010).

E. Zhang, J. Laufer, and P. Beard, "Backward-mode multiwavelength photoacoustic scanner using a planar Fabry-Perot polymer film ultrasound sensor for high-resolution three-dimensional imaging of biological tissues," Appl. Opt. **47,** 561-577 (2008).

E. Zhang, J. Laufer, R. Pedley, and P. Beard, "In vivo high-resolution 3D photoacoustic imaging of superficial vascular anatomy," Physics in Medicine & Biology **54,** 1035 (2009).

H. F. Zhang, K. Maslov, M. Sivaramakrishnan, G. Stoica, and L. V. Wang, "Imaging of hemoglobin oxygen saturation variations in single vessels in vivo using photoacoustic microscopy," Appl. Phys. Lett. **90,** 053901 (2007).

H. F. Zhang, K. Maslov, G. Stoica, and L. V. Wang, "Functional photoacoustic microscopy for high-resolution and noninvasive in vivo imaging," Nat. Biotechnol. **24,** 848 (2006).

P. Zhang, G. Fitzpatrick, T. Harrison, W. A. Moussa, and R. J. Zemp, "Double-SOI wafer-bonded CMUTs with improved electrical safety and minimal roughness of dielectric and electrode surfaces," J Microelectromech Syst **21,** 668-680 (2012).

P. Zhang, W. Zheng, W. Moussa, and R. J. Zemp, "CMUTs with interlaced high-and low-frequency elements," in *Ultrasonics Symposium (IUS), 2011 IEEE International,* Anonymous (IEEE, 2011), pp. 116-119.

S. Zhang, R. Cheng, C. Tao, and X. Liu, "Photoacoustic tomography with a high lateral resolution and a large field of view using a rectangular focused ultrasound transducer," Applied Physics Express **9,** 047301 (2016).

K. R. Zinn, T. R. Chaudhuri, A. A. Szafran, D. O'Quinn, C. Weaver, K. Dugger, D. Lamar, R. A. Kesterson, X. Wang, and S. J. Frank, "Noninvasive bioluminescence imaging in small animals," ILAR journal **49,** 103-115 (2008).